

**EFFECT OF BOUNDARY LAYER TRIP AND  
TUBERCLES ON AERODYNAMIC PERFORMANCE  
OF E216 AIRFOIL**

Thesis

Submitted in partial fulfillment of the requirements for the degree of

**DOCTOR OF PHILOSOPHY**

by

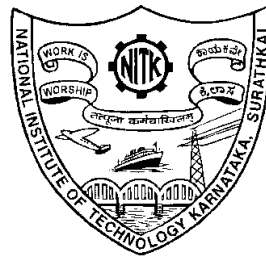
**SREEJITH B K**

(ME13F08)

Under the Guidance of

**Dr. SATHYABHAMA A**

**Associate Professor**



**DEPARTMENT OF MECHANICAL ENGINEERING  
NATIONAL INSTITUTE OF TECHNOLOGY KARNATAKA  
SURATHKAL, MANGALURU - 575025, INDIA**

**December 2018**

## **DECLARATION**

*by the Ph D Research Scholar*

I hereby **declare** that the Research Thesis entitled “**Effect of Boundary Layer Trip and Tubercles on Aerodynamic Performance of E216 Airfoil**” which is being submitted to the **National Institute of Technology Karnataka, Surathkal** in partial fulfillment of the requirements for the award of the Degree of **Doctor of Philosophy in Mechanical Engineering** is a *bonafide report of the research work carried out by me*. The material contained in this thesis has not been submitted to any University or Institution for the award of any degree.

Name of the Research Scholar: **SREEJITH B K**

Register No.: **ME13F08**

Signature of Research Scholar:

Department of Mechanical Engineering

Place: NITK - Surathkal

Date:

## CERTIFICATE

This is to certify that the Research Thesis entitled “**Effect of Boundary Layer Trip and Tubercles on Aerodynamic Performance of E216 Airfoil**”, submitted by **Mr. SREEJITH B K (Register Number: 135069ME13F08)** as the record of the research work carried out by him, is *accepted* as the *Research Thesis submission* in partial fulfillment of the requirements for the award of degree of **Doctor of Philosophy**.

Dr. Sathyabhama A  
Research Guide  
Date:

Chairman-DRPC  
Date:

This thesis is  
dedicated to  
*My beloved*  
**Mother and family**

## ACKNOWLEDGEMENTS

I take this opportunity to thank all the people who have guided, supported and encouraged me to complete my research work. Firstly, I would like to express my sincere gratitude to my advisor **Dr. Sathyabhama A** for the continuous support for my Ph.D study and related research, for her patience, motivation, and immense knowledge. Her guidance helped me in all the time of research and writing of this thesis. Besides my advisor, I would like to thank the rest of my thesis committee members **Dr. Arun M** and **Dr. Hari Prasad Dasari**, for their insightful comments and encouragement, but also for the hard question which incited me to widen my research from various perspectives. I am also thankful to **Dr. Narendranath S**, Professor and Head, Department of Mechanical Engineering for his support.

I express my heartfelt gratitude to my colleagues **Suhas B G, Reshmi R, Prashanth S P, Kumar Karthik, Sathyajith, Athul, Avdooth W, Jeena Joseph, Jaypal Reddy, Raghavendra** and **Sandeep** for furnishing necessary aids and for their co-operation throughout the period of research work. As thank and appreciation does not value in friendship, I would just remember **Sreebhash S Kutty, Thippesh L R, and Abdhul R Buradi**, the dynamic and empathetic personalities I ever met.

(SREEJITH B K)

## ABSTRACT

The thesis presents experimental and numerical investigation on the aerodynamic performance of airfoil E216 in prestall region at Reynolds number ( $Re$ ) of  $1 \times 10^5$ . The effect of boundary layer trip (BLT) of different shapes and leading edge tubercles are studied with an aim to improve the aerodynamic performance and to eliminate the laminar separation bubble (LSB) formation on the airfoil. Finally the effect of modification are addressed in terms of performance improvement in the power output of a conceptual turbine which is capable of generating 100W at wind speed of 6.5 m/s.

In the study Rectangular (RT), Right angled triangular (RA) and Isosceles triangular (IT) shaped boundary layer trips of different height located at two different positions are investigated. Wind tunnel experiment is conducted with rectangular boundary layer trip and is used for validation of numerical methodology. The amplitude of the tubercles are varied from 2 mm to 8 mm and wavelength from 15.5 mm to 62 mm. The different combination of the amplitudes and wavelengths resulted in total of nine models. Out of these, wind tunnel experiment are conducted on three models and are used to validate the numerical results. Langtry-Menter 4-equation Transitional SST Model or  $\gamma - Re_{\theta}$  - SST model is used in the study to model laminar separation bubble and effect of trip and tubercles on it.

The investigation revealed that the the airfoil stalls at  $12^{\circ}$  with lift coefficient ( $C_l$ ) of 1.37 and drag coefficient ( $C_d$ ) of 0.063. Maximum value of lift to drag ratio of 42.46 is obtained at AOA of  $4^{\circ}$ . Surface pressure distribution over the airfoil shows the presence of laminar separation bubble. The laminar separation bubble (LSB) formed at a

distance of  $x/c = 0.22$  from leading edge at AOA of  $6^\circ$ . The location of laminar separation bubble moved upstream with increase in AOA. Based on the location of laminar separation bubble at AOA of  $6^\circ$ , boundary layer trips are positioned at  $0.17c$  and  $0.10c$  from leading edge of the airfoil. Result showed that boundary layer trip eliminates LSB partially or completely and improves the aerodynamic performance of the airfoil. Highest improvements of 16.7% in  $C_d$  and 34.6% in  $C_l/C_d$  are obtained for location-2 with the rectangular trip having lowest trip height of 0.3 mm at AOA of  $8^\circ$ . In all the cases, improvement in performance is observed only up to trip height of 0.5 mm. There is no observable advantage for isosceles and right-angled triangular trips over rectangular trips.

Improvement in  $C_l$  is observed for most of the tubercled models and is significant at high angles of attack. But simultaneous increase in drag coefficient resulted in little improvement in  $C_l/C_d$  for most of the cases. But tubercled model with amplitude 2 mm and wavelength of 62 mm (A2W62) produced a peak value of 46.91 at AOA  $6^\circ$  which is higher than the baseline by 7.37%. Compared to baseline, there is high suction peak pressure along the trough and lower along the peak. The low amplitude and low wavelength tubercled model exhibited smooth  $C_p$  distribution without any sign of strong LSB. The LSB moves upstream with increasing amplitude and wavelength. LSB along the trough is formed ahead of that at peak inducing three-dimensional wavy shaped LSB unlike the straight LSB for the baseline. The tubercles considerably reduced the size of LSB compared to baseline. Two pairs of counter rotating vortices are formed on the airfoil surface between the adjacent peaks at two different chord-wise locations which strongly alter the flow pattern over it. The effect of trips and tubercles is demonstrated using a wind turbine performance analysis using BEM theory and it is seen that average improvement in power coefficient by 1.65% is obtained with the boundary layer trip and by 0.64% is achieved with the tubercles.

# TABLE OF CONTENTS

<b>ACKNOWLEDGEMENTS</b>	<b>iv</b>
<b>ABSTRACT</b>	<b>v</b>
<b>LIST OF TABLES</b>	<b>xi</b>
<b>LIST OF FIGURES</b>	<b>xvii</b>
<b>NOMENCLATURE</b>	<b>xx</b>
<b>1 INTRODUCTION</b>	<b>1</b>
1.1 OVERVIEW . . . . .	1
1.2 SMALL SCALE WIND TURBINE . . . . .	1
1.3 LOW REYNOLDS NUMBER AERODYNAMICS . . . . .	2
1.3.1 Laminar separation bubble . . . . .	4
1.4 FLOW CONTROL TECHNIQUES . . . . .	7
1.4.1 Boundary layer trip . . . . .	8
1.4.2 Tubercles . . . . .	9
1.5 PROBLEM STATEMENT . . . . .	10
1.6 OVERVIEW OF THE THESIS . . . . .	12
<b>2 LITERATURE REVIEW</b>	<b>13</b>
2.1 OVERVIEW . . . . .	13
2.2 SMALL SCALE WIND TURBINE . . . . .	13
2.3 BOUNDARY LAYER TRIP (BLT) . . . . .	15
2.4 EFFECT OF TUBERCLES ON AIRFOIL PERFORMANCE . . . . .	18



2.4.1	Flow structure over the airfoil with tubercles . . . . .	21
2.4.2	Flow mechanism with tubercles . . . . .	25
2.5	MOTIVE AND SCOPE OF THE PRESENT WORK . . . . .	26
2.6	RESEARCH OBJECTIVES . . . . .	27
<b>3</b>	<b>METHODOLOGY</b>	<b>29</b>
3.1	OVERVIEW . . . . .	29
3.2	EXPERIMENTAL METHODOLOGY . . . . .	29
3.2.1	Airfoil model design and fabrication . . . . .	29
3.2.2	Boundary layer trip . . . . .	30
3.2.3	Tubercled airfoil model . . . . .	32
3.2.4	Wind tunnel . . . . .	33
3.2.5	Pressure measurements . . . . .	33
3.2.6	Pitot tube measurements . . . . .	39
3.2.7	Wind tunnel boundary layer profile . . . . .	40
3.2.8	Boundary layer probe measurements . . . . .	41
3.2.9	Wind tunnel turbulence intensity . . . . .	42
3.2.10	Wind tunnel corrections . . . . .	43
3.3	UNCERTAINTIES IN THE EXPERIMENT . . . . .	45
3.4	REPEATABILITY . . . . .	46
3.5	NUMERICAL METHODOLOGY . . . . .	47
3.5.1	Geometry . . . . .	47
3.5.2	Computational domain and mesh . . . . .	48
3.5.3	Boundary conditions and solver setup . . . . .	50
3.5.4	Turbulence model . . . . .	52
3.5.5	Grid independent study . . . . .	55
3.6	DESIGN OF WIND TURBINE BLADE . . . . .	57
3.6.1	Size of wind turbine . . . . .	57
3.6.2	Blade shape . . . . .	58

<b>4</b>	<b>RESULTS AND DISCUSSION</b>	<b>63</b>
4.1	OVERVIEW . . . . .	63
4.2	AIRFOIL SELECTION . . . . .	63
4.3	AERODYNAMIC PERFORMANCE OF AIRFOIL E216 . . . . .	64
4.4	LAMINAR SEPARATION BUBBLE . . . . .	65
4.4.1	Simulation results for coefficient of surface pressure distribution ( $C_p$ ) . . . . .	69
4.4.2	Velocity vector plot . . . . .	70
4.5	AERODYNAMIC FORCE ANALYSIS OF THE AIRFOIL WITH RECTANGULAR TRIP . . . . .	73
4.5.1	Coefficient of surface pressure distribution with and without boundary layer trip . . . . .	78
4.6	AIRFOIL WITH BLT OF DIFFERENT SHAPE . . . . .	85
4.6.1	Coefficient of surface pressure distribution . . . . .	85
4.6.2	Velocity vector plots . . . . .	87
4.6.3	Aerodynamic performance analysis . . . . .	88
4.7	EFFECT OF LEADING EDGE TUBERCLES ON AERODYNAMIC PERFORMANCE OF THE AIRFOIL . . . . .	99
4.7.1	Validation of numerical simulation . . . . .	99
4.7.2	Simulation results for the airfoil with tubercle . . . . .	102
4.7.3	Distribution of coefficient of surface pressure . . . . .	111
4.7.4	Surface flow pattern analysis . . . . .	118
4.7.5	Flow physics . . . . .	125
4.8	BLADE DESIGN . . . . .	134
4.8.1	Performance analysis . . . . .	137
4.9	EFFECT OF BLT AND TUBERCLES ON THE PERFORMANCE OF SSWT . . . . .	138
<b>5</b>	<b>CONCLUSIONS AND SCOPE FOR FUTURE WORK</b>	<b>141</b>
5.1	CONCLUSIONS . . . . .	141

5.2 SCOPE FOR FUTURE WORK . . . . .	143
<b>APPENDICES</b>	<b>145</b>
<b>A ADDITIONAL DETAILS RELATED TO EXPERIMENTAL AND NUMERICAL WORK</b>	<b>145</b>
A.1 Airfoil terminology . . . . .	145
A.2 Drag force and Lift force . . . . .	146
A.3 Airfoil coordinates . . . . .	146
A.4 Wind tunnel calibration . . . . .	147
A.5 Iso surface plot of zero velocity . . . . .	148
<b>B MATLAB CODE FOR SSWT BLADE DESIGN AND PERFORMANCE ASSESSMENT USING BEM THEORY</b>	<b>151</b>
<b>C UNCERTAINTY IN EXPERIMENTAL MEASUREMENTS</b>	<b>155</b>
C.1 Uncertainty associated with coefficient of pressure ( $C_p$ ) . . . . .	155
C.2 Uncertainty associated with coefficient of normal force ( $C_n$ ) . . . . .	155
C.3 Uncertainty associated with coefficient of normal force ( $C_n$ ) . . . . .	156
C.4 Uncertainty associated with coefficient of lift ( $C_l$ ) . . . . .	156
C.5 Uncertainty associated with coefficient of drag ( $C_d$ ) . . . . .	156
C.5.1 Uncertainty associated with $u/U_\infty(\delta_{u/U_\infty})$ : . . . . .	156

## LIST OF TABLES

3.1	Wind tunnel specifications . . . . .	35
3.2	Location of pressure ports from leading edge of the airfoil . . . . .	37
3.3	Probe locations for boundary layer measurement . . . . .	42
3.4	Uncertainty in derived parameters . . . . .	46
3.5	Tubercled model parameters . . . . .	48
3.6	Grid number used for different kind of BLT model . . . . .	56
4.1	Laminar separation bubble location and size on baseline and modified models . . . . .	117
4.2	Geometrical parameters of blade . . . . .	135
A.1	E216 airfoil coordinates (UIUC 2014) . . . . .	147
C.1	Uncertainty in $C_p$ at AOA of $4^0$ . . . . .	157
C.2	Uncertainty in $C_l$ , $C_d$ and $C_l/C_d$ . . . . .	158

## LIST OF FIGURES

1.1	Small scale wind turbine (Energypress 2019) . . . . .	2
1.2	Influence of Reynolds number on airfoil (NACA-0012) behaviour (Musial and Cromack 1988) . . . . .	3
1.3	Laminar separation bubble (LSB) (Jahanmiri 2011) . . . . .	5
1.4	Laminar separation bubble - Zoomed view (Jahanmiri 2011) . . . . .	5
1.5	Laminar Vs. Turbulent boundary layer over a sphere (Bergman <i>et al.</i> 2007) . . . . .	8
1.6	Conventional boundary layer trip (BLT) on airfoil (Hansen 2012) . . . . .	9
1.7	Conceptual illustration of trip effect. (Gopalarathnam <i>et al.</i> 2003) . . . . .	9
1.8	Tubeclles on Humpback whale flipper (Johari <i>et al.</i> 2007) . . . . .	11
2.1	Comparison of a Humpback whale pectoral flipper cross section with the NACA 63 <sub>4</sub> -021 airfoil profile (Custodio 2007). . . . .	19
2.2	Streamline over the tubercled airfoil forming surface vortices (Malipeddi <i>et al.</i> 2012) . . . . .	23
2.3	Streamlines over tubercled airfoil model NACA 0012 showing onset of separation and re attachment point of LSB (Rostamzadeh <i>et al.</i> 2014) . . . . .	23
3.1	Airfoil E216 (maximum thickness = 10:4% at 26:2% of chord (UIUC 2014)) . . . . .	30
3.2	Airfoil with trip . . . . .	32
3.3	Tubercled model showing the nomenclature and dimensions used for simulation . . . . .	33
3.4	Tubercled models used for experiment: (a) A2W15.5, (b) A4W31 and (c) A8W62 . . . . .	34
3.5	Subsonic wind tunnel facility at National Institute of Technology Karnataka, India . . . . .	34
3.6	Electronic differential manometer (Make:HTC, Model: PM-6202) . . . . .	35

3.7	Pressure taps on baseline airfoil: (a) suction surface and (b) pressure surface . . . . .	36
3.8	A discrete element on the airfoil surface of length $ds$ showing the resolved components of forces (Hansen 2012) . . . . .	38
3.9	Schematic of wake survey method . . . . .	40
3.10	Boundary layer probe . . . . .	41
3.11	Boundary layer profile . . . . .	43
3.12	Repeatability of the experiment . . . . .	46
3.13	Different shapes of BLT used in the study: (a) rectangle, (b) right-angled triangle, (c) isosceles triangle . . . . .	47
3.14	Tubercle geometry created through lofting . . . . .	48
3.15	Far view of structured grid in the domain with boundary conditions . . . . .	49
3.16	Close view of dense grid around the airfoil . . . . .	49
3.17	Grid configuration near to BLT . . . . .	49
3.18	Computational domain . . . . .	50
3.19	Far view of structured grid in the domain . . . . .	51
3.20	Close view of dense grid nearer to the airfoil . . . . .	51
3.21	Grid on the airfoil surface . . . . .	51
3.22	Effect of number of grid cells on lift and drag coefficient for baseline airfoil at $6^0$ AOA . . . . .	56
3.23	Variation of $C_l$ and $C_d$ of the baseline airfoil with grid number at AOA of $6^0$ . . . . .	57
3.24	Flow chart for BEM code . . . . .	61
4.1	Variation of $C_l/C_d$ with AOA . . . . .	64
4.2	$C_l$ and $C_d$ results obtained from experiment and simulation as a function of AOA . . . . .	65
4.3	$C_l/C_d$ obtained from experiment and simulation as a function of AOA . . . . .	66
4.4	$C_p$ distribution over a typical airfoil (Russell 1979) . . . . .	66
4.5	Comparison of numerical and experimental result for $C_p$ distribution over the airfoil at AOA of $6^0$ . . . . .	68

4.6	Oil flow visualisation on E216 airfoil at AOA of $6^0$ . . . . .	68
4.7	$C_p$ distribution over the airfoil at different AOA . . . . .	69
4.8	Location of LSB for different AOA . . . . .	71
4.9	Velocity vector plot showing LSB formation over airfoil for AOA of $6^0$ . . . . .	71
4.10	Close view of LSB showing recirculation region at AOA of $6^0$ (where the reversed velocity vector direction shows recirculation and flow transition) . . . . .	71
4.11	Velocity vectors over the airfoil coloured with velocity magnitude (red represents highest and blue represents lowest velocity) . . . . .	72
4.12	Effect of trip height and location on (a) $C_d$ and (b) $C_l/C_d$ of airfoil at AOA = $4^0$ ( Validation with experimental results are also shown) . . . . .	74
4.13	Effect of trip height and location on (a) $C_d$ and (b) $C_l/C_d$ of airfoil at AOA = $6^0$ . . . . .	75
4.14	Effect of trip height and location on (a) $C_d$ and (b) $C_l/C_d$ of airfoil at AOA = $8^0$ . . . . .	76
4.15	Comparison of $C_p$ with and without trip at location-1 for AOA of $6^0$ . . . . .	79
4.16	$C_p$ distribution on the airfoil surface for AOA of $4^0$ : (a) trip at location-1 and (b) trip at location-2 . . . . .	80
4.17	$C_p$ distribution on the airfoil surface for AOA of $6^0$ : (a) trip at location-1 and (b) trip at location-2 . . . . .	81
4.18	$C_p$ distribution on the airfoil surface for AOA of $8^0$ : (a) trip at location-1 and (b) trip at location-2 . . . . .	82
4.19	Velocity vector plot over the airfoil at AOA $4^0$ and different trip heights for location-1 (R represents reattachment location) . . . . .	83
4.20	Velocity vector plot over the airfoil at AOA $4^0$ and different trip heights for location-2 (R represents reattachment location) . . . . .	84
4.21	$C_p$ distribution around airfoil for trip of different shape with height 0.7 mm for AOA of $4^0$ at (a) location-1 and (b) location-2 . . . . .	86
4.22	Velocity vector profile over the airfoil with trip height of 0.7 mm and different trip shapes at location-1 for AOA of $4^0$ (R - flow re-attachment point) . . . . .	87
4.23	Velocity vector profile over the airfoil with trip height of 0.7 mm and different trip shapes at location-2 for AOA of $4^0$ (R - flow re-attachment point) . . . . .	88

4.24	Effect of trip on $C_d$ of airfoil at AOA = $4^0$ at (a) location-1 and (b) location-2 . . . . .	89
4.25	Effect of trip on $C_l/C_d$ of airfoil at AOA = $4^0$ at (a) location-1 and (b) location-2 . . . . .	90
4.26	Effect of trip on $C_d$ of airfoil at AOA = $6^0$ at (a) location-1 and (b) location-2 . . . . .	93
4.27	Effect of trip on $C_l/C_d$ of airfoil at AOA = $6^0$ at (a) location-1 and (b) location-2 . . . . .	94
4.28	Effect of trip on $C_d$ of airfoil at AOA = $8^0$ at (a) location-1 and (b) location-2 . . . . .	96
4.29	Effect of trip on $C_l/C_d$ of airfoil at AOA = $8^0$ at (a) location-1 and (b) location-2 . . . . .	97
4.30	Distributions of TKE without (4.30a) and with BLT (4.30b - 4.30e) at AOA $6^0$ for RT trip . . . . .	98
4.31	Validation of baseline 3D simulation with experimental results . . . . .	100
4.32	Experimental results (4.32a) and simulations (4.32b) for tubercled models . . . . .	101
4.33	Effect of amplitude on $C_l$ of airfoil . . . . .	103
4.34	Effect of amplitude on $C_d$ of airfoil . . . . .	105
4.35	Effect of amplitude on $C_l/C_d$ of airfoil . . . . .	106
4.36	Effect of wavelength on $C_l$ of airfoil . . . . .	108
4.37	Effect of wavelength on $C_d$ of airfoil . . . . .	109
4.38	Effect of wavelength on $C_l/C_d$ of airfoil . . . . .	110
4.39	$C_p$ distribution on modified and unmodified models at AOA of $4^0$ . . . . .	112
4.40	$C_p$ distribution on modified and unmodified models at AOA of $4^0$ . . . . .	115
4.41	$C_p$ distribution for modified and unmodified models at AOA of $4^0$ . . . . .	116
4.42	Front view of the (a)baseline and (b)modified airfoil-A4W31 with surface streamlines, showing the bifurcation line . . . . .	118
4.43	Three dimensional streamline over the airfoils . . . . .	119
4.44	Contours of pressure on the suction surface: (a) Baseline (b)A2W15.5, (c) A4W31 and (d) A8W62 at AOA = $4^0$ . . . . .	121



4.45	Velocity streamlines on the suction surface showing the flow inclining from peak to trough at AOA = $4^0$ : (a)A2W15.5, (b) A4W31 and (c) A8W62. . . . .	122
4.46	Surface streamlines on A4W31 marked with different regions in the flow pattern at AOA = $4^0$ (flow is from left to right) . . . . .	123
4.47	Iso surface of zero velocity over the airfoils showing the region of separation(LSB) along with surface streamlines at AOA of $4^0$ (continuous blue area shows the separation region and flow is from top to down) . . . . .	124
4.48	Three dimensional velocity streamlines emerging from the primary vortices(A4W31 at AOA = $4^0$ ) . . . . .	125
4.49	Three-Dimensional vortex formation plotted on different planes normal to airfoil surface at different $x/c$ distance starting from leading edge of the tubercle model A4W31 at AOA of $4^0$ . . . . .	126
4.50	Surface streamline pattern on plain airfoil model at AOA of $4^0$ . . . . .	127
4.51	Surface streamlines distribution over modified airfoils . . . . .	128
4.51	Surface streamlines distribution over modified airfoils . . . . .	129
4.51	Surface streamlines distribution over modified airfoils . . . . .	130
4.52	Velocity stream lines on A2W31 at AOA of $4^0$ , showing velocity variation at different stream-wise and span-wise locations . . . . .	134
4.53	Pressure contour on A2W31 at AOA of $4^0$ , showing pressure variation at peak and trough . . . . .	135
4.54	Blade sections (bottom view) . . . . .	136
4.55	Blade sections . . . . .	136
4.56	CAD geometry of generated turbine model . . . . .	136
4.57	Variation of axial induction factor with radius of blade . . . . .	137
4.58	Variation of Coefficient of power with Tip Speed Ratio . . . . .	138
4.59	Variation of power coefficient of SSWT with BLT for various tip speed ratio . . . . .	139
4.60	Power coefficient variation of SSWT with tubercle for various tip speed ratio . . . . .	139
A.1	Airfoil terminology (Manwell <i>et al.</i> 2010) . . . . .	145
A.2	Lift and drag components of aerodynamic forces (Manwell <i>et al.</i> 2010) . . . . .	146

A.3	Wind tunnel calibration chart . . . . .	148
A.4	Iso surface of zero velocity showing flow separation regimes . . . . .	148
A.4	Iso surface of zero velocity showing flow separation regimes . . . . .	149

## NOMENCLATURE

$A$	Amplitude (m)
$A_s$	Swept area of turbine ( $m^2$ )
$C_d$	Drag coefficient
$C_l$	Lift coefficient
$C_p$	Coefficient of pressure
$C_t$	Coefficient of tangential force
$Re_T$	Viscosity ratio Reynolds number
$Re_\theta$	Momentum thickness Reynolds number
$Re_k$	Roughness Reynolds number
$Re_v$	Strain rate (vorticity) Reynolds number
$Re_{\theta c}$	Critical Reynolds number
$Re_{\theta t}$	Transition onset momentum thickness Reynolds number
$S$	Strain rate
$U_\infty$	Free stream velocity ( $m^2/s$ )
$W$	Wavelength (m)
$\tilde{Re}_{\theta t}$	Local transition onset momentum thickness Reynolds number

$c$	Chord length (m)
$ds$	Distance between nearby pressure port on the airfoil surface (m)
$h$	Pressure head (m)
$k$	Turbulent kinetic energy, ( $m^2/s^2$ )
$k_r$	Boundary layer trip height (m)
$u_k$	Velocity on the top of the roughness element (m/s)
$x/c$	Axial distance over airfoil along axial chord
$y^+$	Non dimensional wall distance

### **Greek Symbols**

$\alpha$	Angle of attack ( $^{\circ}$ )
$\delta$	Boundary layer height (m)
$\eta$	Overall efficiency of turbine
$\gamma$	Intermittency
$\mu$	Molecular viscosity ( $Pa.s$ )
$\mu_t$	Eddy viscosity ( $m^2/s$ )
$\nu_k$	Kinematic viscosity of the air over trip ( $m^2/s$ )
$\Omega$	Absolute value of vorticity
$\omega$	Specific turbulence dissipation rate ( $s^{-1}$ )
$\rho$	Density ( $Kg/m^3$ )

### **Subscripts**

$\infty$  Free stream (static) entity

$0$  Total entity

$s$  Streamline

$t$  Transition onset

$w$  Property of water

### **Abbreviation**

2D Two dimensional

AOA Angle of attack

CFD Computational fluid dynamics

IT Isosceles triangular

LSB Laminar separation bubble

RA Right-angled triangular

RANS Reynolds averaged Navier–Stokes

RT Rectangular

SIMPLE Semi-implicit method for pressure-linked equations

SSWT Small scale wind turbines

TKE Turbulent kinetic energy

# CHAPTER 1

## INTRODUCTION

### 1.1 OVERVIEW

Lack of electricity in rural area is a worldwide problem that affects more than 1.5 billion people (Cabanillas Sanchez 2013). Electrification in rural areas improves their communication and exposure to outside world which brings socio-economic development. In the absence of grid facilities for bringing electricity, in-house production is the available alternative for electrification. Wind energy is a best alternative method for self-sufficiency in rural areas. Utilization of renewable energy benefits people in terms of improved healthy environment and extended productive hours. Moreover installation of large wind farms provides job opportunity for rural people.

### 1.2 SMALL SCALE WIND TURBINE

Large scale wind turbines (LSWT) require high wind potential and large area of free land. Investment cost of large wind turbine is also very high. The alternative method for extraction of wind energy is to use small scale wind turbine (SSWT). The wind turbines of rotor diameter less than 10 m and having power capacity less than 20 kW are classified as SSWT (Tummala *et al.* 2016). Figure 1.1 shows the photograph of a SSWT. The low investment cost and ability to work in low wind condition are the advantages of SSWT. So this system can be installed in urban area as a supplementary power source for buildings. It can be used either as a standalone system which can provide energy demand for entire building or as a backup power source. Noise pollution and safety

hazards of SSWT are very less compared to large wind turbines. The SSWT is a best alternative for rural electrification and power resource for polar research centers where zero emission environment persists. The SSWT can be integrated with PV cells and is a promising technique for maximum utilisation of renewable energy. Large population in the world use mobile phones, laptops and other electronic personal gadgets, which consume electrical power. Though their individual energy consumption is low, cumulative power consumption comes in large figure. To recharge these kind of electronic equipment, SSWT can be used. It can also act as an emergency power source for communication system and other rescue instruments in natural calamity affected areas. Hence the technique reduces fossil fuel consumption and environmental impact.



Figure 1.1: Small scale wind turbine ([Energypress 2019](#))

### 1.3 LOW REYNOLDS NUMBER AERODYNAMICS

Aerodynamic performance of a wind turbine is influenced much by Reynolds number (Re). Reynolds number for airfoil is defined by Equation 1.1.

$$Re = \frac{cU_{rel}}{\nu} \quad (1.1)$$

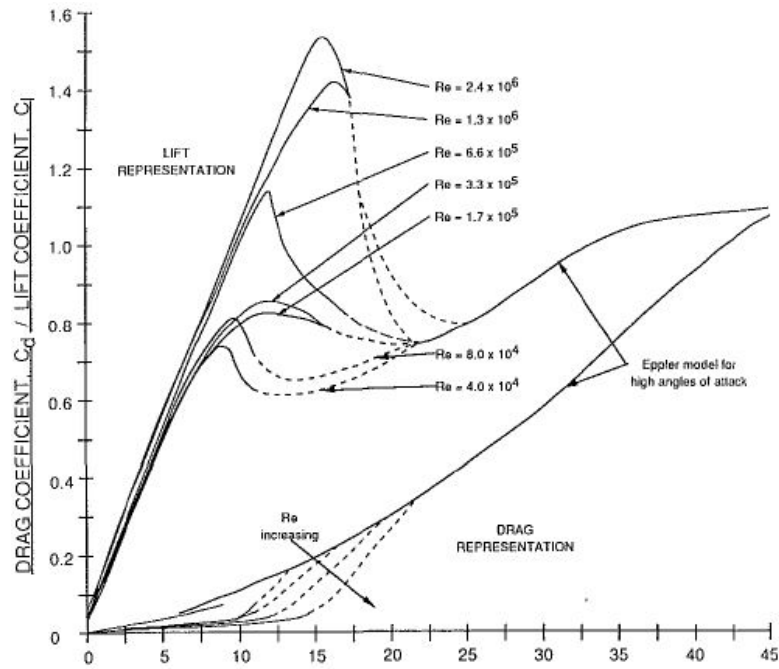


Figure 1.2: Influence of Reynolds number on airfoil (NACA-0012) behaviour (Musial and Cromack 1988)

Where  $\nu$ ,  $c$  and  $U_{rel}$  are kinematic viscosity of air, chord length of airfoil - which forms the blade cross section (Appendix A) and relative velocity of wind (vector sum of wind speed and rotational speed of rotor) respectively. For SSWT, blade chord length is small compared to LSWT. Also SSWT is erected where low wind velocity persists. Reynolds number for SSWT corresponding to these chord length and wind velocity is of very low value (less than  $1 \times 10^6$ ). Studies carried out by Musial and Cromack (1988) showed the influence of Re on coefficient of lift ( $C_l$ ) and coefficient of drag ( $C_d$ ). Decrease in Re reduces  $C_l$  and increases  $C_d$  (Table 1.2) which results in drastic reduction in  $C_l/C_d$  ratio. Power generation from turbine blade is proportional to  $C_l/C_d$  ratio of its airfoil. The reduction in  $C_l/C_d$  ratio results in net performance reduction of SSWT in low Re.

Power developed by wind turbine is proportional to square of rotor radius( $r$ ), cube of free stream wind speed ( $U_\alpha$ ) and  $C_l/C_d$  ratio of the blade's airfoil. For a SSWT both radius and wind speed are constrained. So the developed power output may also be low.



Maximizing the performance of the blade (maximum  $C_l/C_d$  ratio) is the only way to increase power output. Maximum efficiency can be achieved by aerodynamic performance improvement of blades/airfoil. This ratio can be increased by either increasing  $C_l$  or reducing  $C_d$ . Improvement in  $C_l$  can be achieved by going for higher angle of attack (AOA). Since almost all SSWT are constant pitch stall regulated turbines, it is not possible to provide an AOA more than critical AOA at design condition. Moreover, at high AOA  $C_d$  will be very high and inturn  $C_l/C_d$  ratio will be low. Alternative solution is to reduce  $C_d$ . Drag produced by airfoil is mainly from pressure drag and viscous drag. Pressure drag can be reduced by using thin airfoil, but there exists restriction because of structural limitations. In low Re airfoils, in addition to viscous drag, drag due to laminar separation bubble (LSB) developed under high adverse pressure also plays a major role in total drag. Detailed discussion on the LSB is presented in the next section.

### **1.3.1 Laminar separation bubble**

The boundary layer around an airfoil must negotiate areas of favourable and adverse pressure gradients. A favourable pressure gradient is one in which the pressure is decreasing in the direction of the flow and is present on the leading edge portion of the airfoil. As the curvature of the surface changes sign, the static pressure increases with downstream distance thus creating an adverse pressure gradient (APG). The APG is accompanied by decreased flow velocity as is evident from the stream-wise momentum equation inside the boundary layer (Equation 1.2). At some point, portions of the flow very near the surface of the airfoil begin to flow in a direction opposite to that of the free stream. This point is the separation point of the boundary layer. At low Reynolds numbers, the freestream laminar flow contains very little kinetic energy and is not able to overcome the APG and commonly separates before it can transition to turbulent flow. The separated laminar boundary layer transitions to a turbulent flow and gains energy due to momentum exchange with the mean flow. If enough energy is gained by the

turbulent flow, the boundary layer will be able to withstand the APG and subsequently re-attach to the surface (Walker 1992) as shown in Figures 1.3 and 1.4. The region between the flow separation and reattachment forms a recirculating dead air zone and is called laminar separation bubble (LSB) (Jahanmiri 2011). Laminar separation bubble (LSB) formation is a common aerodynamic phenomenon observed on the SSWT blades which operate in low Re environment (Musial and Cromack 1988)

$$u \frac{\partial u}{\partial x} = -\frac{1}{\rho} \frac{\partial p}{\partial x} = \nu \frac{\partial^2 u}{\partial y^2} \quad (1.2)$$

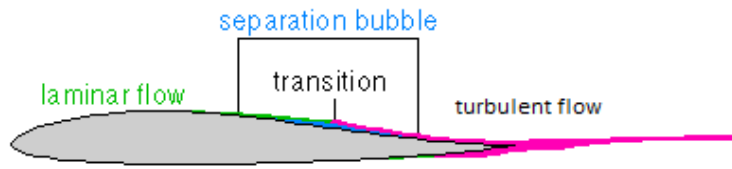


Figure 1.3: Laminar separation bubble (LSB) (Jahanmiri 2011)

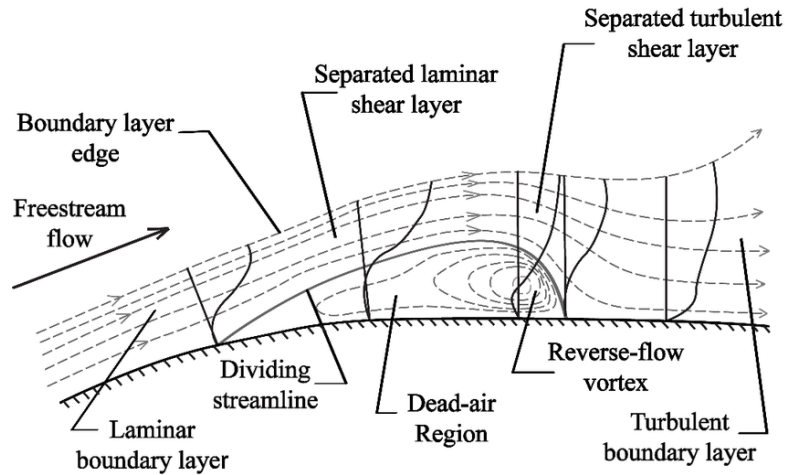


Figure 1.4: Laminar separation bubble - Zoomed view (Jahanmiri 2011)

Skin friction coefficient ( $C_f$ ) has great influence on LSB formation. Von Karman integral boundary-layer equation (Melville Jones 1934) can be written as,

$$\frac{1}{\rho u_e^2 \theta} \frac{d(\rho u_e^2 \theta)}{d(\xi)} = \frac{C_f}{2\theta} - \frac{H}{u_e} \frac{du_e}{d\xi} \quad (1.3)$$

where  $\xi$  is the boundary-layer co-ordinate and  $u_e$  is the boundary-layer edge velocity. The term  $H$  is shape factor, defined as the ratio between the boundary-layer momentum thickness ( $\theta$ ) and the boundary-layer displacement thickness ( $\delta^*$ ).

The skin friction inside the bubble is nearly zero (Selig 2003) and then Equation 1.3 becomes,

$$\frac{\Delta(\rho u_e^2 \theta)}{\rho u_e^2 \theta} \simeq -H \frac{\Delta u_e}{u_e} \quad (1.4)$$

and can be re-written as,

$$\Delta(\rho u_e^2 \theta) \simeq \rho u_e \delta^* \Delta u_e \quad (1.5)$$

It can be observed that the increase in drag  $\Delta(\rho u_e^2 \theta)$  due to LSB is proportional to the product of average mass defect  $\rho u_e \delta^*$  and edge velocity jump  $\Delta u_e$ . It implies that the size and position of the LSB are the functions of the airfoil shape, angle of attack (AOA),  $Re$  and environmental conditions (Horton 1968).

The Reynolds number greatly affects the length of the separation bubble. As the angle of attack increases, the adverse pressure gradient increases and the separation bubble moves upstream. The leading edge radius also affects the formation of laminar separation bubbles. A small radius induces a small bubble close to the leading edge. This usually leads to abrupt leading edge stall. A large radius produces a separation bubble in the aft part of the airfoil that leads to a more gradual trailing edge stall (Rothan 1993).

For controlling the boundary layer flow, reduced separation bubble size is essential to improve the aerodynamic performance of low Reynolds number airfoils. The pressure drag associated with the laminar separation bubble can be decreased by proper use of flow separation controls as discussed below.

## 1.4 FLOW CONTROL TECHNIQUES

Flow separation can be controlled by active or passive methods. If the flow control device works with the aid of external power source, the method is termed as active flow control technique. The method usually involves electronically operated actuators consuming energy for operation. Depending on the demand, the device can be switched to ON or OFF mode to achieve optimum performance. Some examples for active flow control techniques used to re-energize the boundary layer and to reduce the APG are discussed below.

In 'suction', small amount of fluid is removed from suction surface of the airfoil (Swatton 2011). The fluid is removed using vacuum and directed towards trailing edge. It stabilises laminar boundary layer and reduces skin friction drag. In another method called Blowing method, the fluid is injected tangentially or normally into boundary layer in oscillatory or continuous form. This blow increases the boundary layer fluid momentum which delays the separation. Likewise there are many active methods such as active dimple actuators (Dearing *et al.* 2007), synthetic jet (Ramesh *et al.* 2009), magnetohydrodynamic flow control (Nosenchuck *et al.* 1995) etc.

Flow control techniques which do not require any external power input are categorised under passive flow control techniques. Some of the passive methods are: the geometrical modifications like Tape strips, longitudinal and transverse grooves which advance the transition point, boundary layer fences that prevent separation, vortex generators to raise the turbulence level and enhance the momentum and energy of the boundary layer, and screens to divert the flow and increase the velocity gradient on the surface. Incorporation of leading edge undulations, called tubercles, on the airfoil is one of the recent passive flow control technique to improve airfoil performance.

### 1.4.1 Boundary layer trip

The flow separation in the laminar flow is much upstream than turbulent flow as illustrated in the Figure 1.5. Turbulent boundary layers are more resistive to flow separation compared to laminar boundary layer (Bergman *et al.* 2007). It shows that forced conversion of laminar boundary layer to turbulent boundary may lead to delayed separation of the flow from airfoil and may lead to suppression of laminar bubble formation. This can be achieved by tripping the laminar boundary layer into turbulent boundary layer with the use of boundary layer trip (BLT) (Preston 1958). Use of mechanical BLT like trip wires, plain trips, zigzag tape, etc are the most effective methods of LSB elimination currently in use.

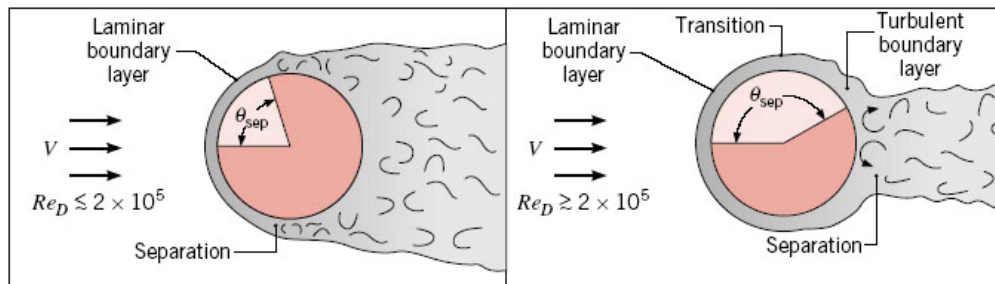


Figure 1.5: Laminar Vs. Turbulent boundary layer over a sphere (Bergman *et al.* 2007)

Boundary layer trips are thin raised strip attached to airfoils suction surface nearer to leading edge as shown in Figure 1.6. The BLT induces flow disturbance and perturbation which alter the suction surface pressure distribution. The altered pressure distribution triggers the flow transition to turbulent. The turbulent flow has capability to withstand adverse pressure gradient due to its higher energy achieved from the enhanced momentum exchange.

Application of trip on airfoil surface has three main effects on the drag of airfoil as shown in Figure 1.7: 1) it reduces bubble drag by eliminating LSB 2) it increases the device drag as trip acts as a disturbance to the flow and 3) it increases skin friction drag

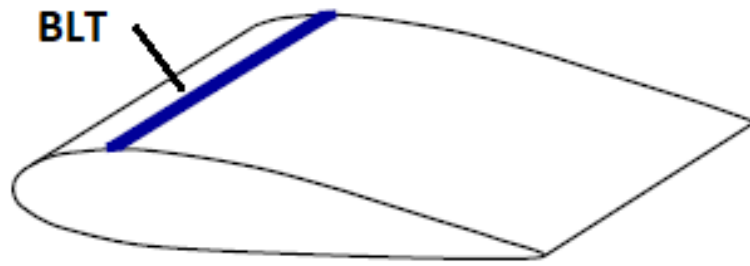


Figure 1.6: Conventional boundary layer trip (BLT) on airfoil (Hansen 2012)

due to the additional turbulent flow region present after the forced transition. The trip can only be effective if the reduction in bubble drag is greater than cumulative increase in device drag and skin friction drag. Hence, the height and position of the BLT are the important parameters to be optimised for the beneficial performance of the BLT.

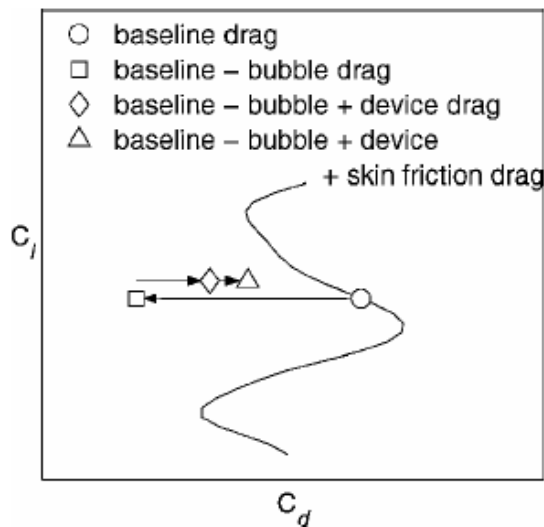


Figure 1.7: Conceptual illustration of trip effect. (Gopalarathnam *et al.* 2003)

## 1.4.2 Tubercles

Leading edge undulations on the airfoil are called tubercles. The technique is inspired from the biological observation on the Humpback whales and resembles the protuber-

ance found over humpback whale flippers. The tubercles on the leading edge of humpback whale flippers (Figure 1.8) are the reason for its better manoeuvrability (Bushnell and Moore 1991).

There are many theories to explain how tubercles affect the airfoil performance, such as vortex theory, vortex lift theory and induced flow theory but none of these are conclusive (Bolzon *et al.* 2015). The vortex theory suggests that tubercles act like vortex generator. The tubercles produce pairs of streamwise, counterrotating vortices which increase boundary layer momentum exchange (Fish and Battle 1995). It results in delayed separation and stall along with improved lift. The Vortex lift theory suggests that, creating strong vortices over the suction side of an airfoil leads to downwash of the vortices which in turn makes flow attached over the surface and thereby delays flow separation. According to induced flow theory, the tubercles produce pairs of streamwise, counter-rotating vortices, and a region of common downwash occurs over each peak, while a region of common upwash occurs over each trough. Where downwash occurs, it is suggested that the effective angle of attack is reduced, resulting in an increased stall angle, whereas the opposite will occur where there is upwash . This spatially periodic change in stall angle will then result in a more gradual stall process and delayed stall. Apart from the aerodynamic effects, tubercles considerably reduce noise during the operation of airfoil (Dewar *et al.* 2013).

## **1.5 PROBLEM STATEMENT**

As discussed previously, LSBs are detrimental to the performance of low Reynolds number airfoils because they typically have the effect of increasing drag, thus reducing aerodynamic efficiency. Consequently, methods of controlling or eliminating LSB are a priority of many aerodynamicists. The most effective passive methods of LSB elimination currently in use involve (i) forcing premature turbulent transition of the boundary

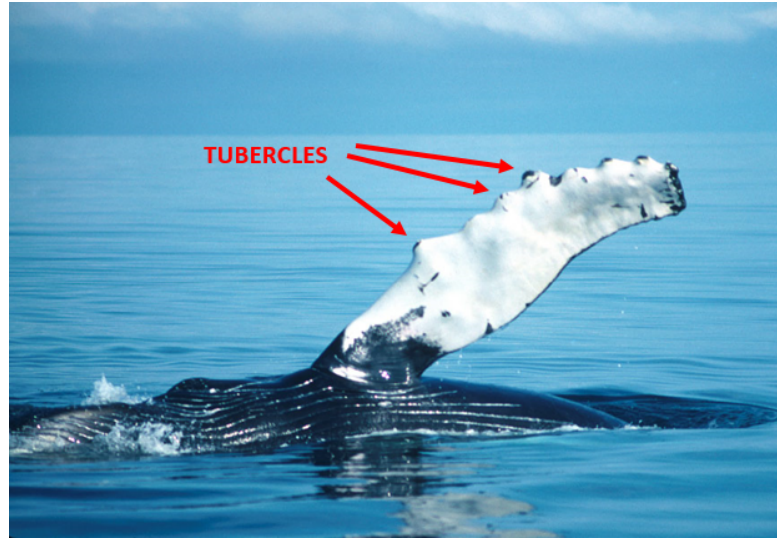


Figure 1.8: Tubercles on Humpback whale flipper (Johari *et al.* 2007)

layer, making it less likely to separate by placing the BLT upstream of the laminar separation point and (ii) delay the separation and stall by using tubercles. In spite of all research efforts, many critical points regarding the effect of tubercles and BLTs on the behavior of LSB are still contradictory and/or inconclusive. The complete understanding of the flow structure and transition mechanisms in the bubble region is still far from complete. While the influence of tubercles and BLT on aerodynamic performance of airfoil have been studied extensively both numerically and experimentally, the effect on LSB is still to be explored. A better understanding of the physical mechanisms which control the formation and structure of separation bubbles and the mechanism by which tubercles and BLT eliminate/reduce the length of LSB is still to be uncovered. At the same time, the interest in the behavior of laminar bubbles is rising, because of their importance in low Reynolds number flow applications. The main objective of this thesis is to investigate the characteristics of LSB with the ultimate goal of eliminating/reducing the length of the bubble by using two passive flow control methods namely the BLTs and tubercles. Other objective is to improve the understanding of the physics involved, focusing on the flow pattern over the models.



## **1.6 OVERVIEW OF THE THESIS**

This thesis consists of five chapters namely introduction, literature review, methodology, results and discussion, conclusions and scope for future work. Bibliography is followed by appendices section.

A substantial amount of research regarding separation bubbles and their elimination by using passive flow control methods is available in open literature. A review of the relevant literature and the objectives of the present work, that have been identified by examining the literature, are given in Chapter 2.

Chapter 3 provides a description of the experimental facilities and measurement techniques used in the course of the research. The low speed wind tunnel facility, its measurement system, and the test models examined are described. Data reduction procedures for the experimental studies along with a discussion of measurement uncertainties are also included. The numerical setup and procedures for the computational aspects of the research are included in Chapter 3. This includes a brief outline of the numerical methods used in the ANSYS-Fluent solver, and a detailed description of the computational domains, their discretization, boundary-conditions and convergence criteria.

Chapter 4 presents the experimental and numerical results. Further, validation of the transition model used in the study is also presented in this chapter. Fifth chapter concludes the results obtained from the present study and gives the scope for future work.

## **CHAPTER 2**

### **LITERATURE REVIEW**

#### **2.1 OVERVIEW**

Literature review for this dissertation has three sections. The first section includes the literature on small scale wind turbine design. Second section provides detailed literature review on Boundary layer trips (BLT). The third section reviews the literature regarding Tubercles and its effect on performance of airfoil.

#### **2.2 SMALL SCALE WIND TURBINE**

A small-scale wind turbine consists of turbine blades, hub, mechanical transmission system and an electrical generator. Power output from the SSWT is quite low compared to the large-scale wind turbine. Any small loss in efficiency of the turbine components may considerably affect the efficiency of the SSWT. Optimisation and performance improvements of these components are very important and essential for SSWT in this perspective. Only limited study for the improvement of performance of the SSWT can be seen in the literature compared to as that of LSWT.

[Kale and Varma \(2014\)](#) designed an 800 mm blade for a 600 W horizontal axis wind turbine using NACA 4412 airfoil. The preliminary geometrical design was carried out based on blade element momentum (BEM) theory and the design was optimized by Betz-Joukowsky Limit Theory. Multiple iterations were carried out to get optimum axial induction factor, radial induction factor, relative blade inflow angle and power co-

efficient incorporating tip loss correction. A reduction of 24% in the chord and 44% in thickness were achieved along with a power coefficient hike of 30% from the respective baseline performance. Parallel genetic algorithm was used by [Polat and Tuncer \(2013\)](#) for aerodynamic shape optimization study carried out on turbine with fixed wind speed, fixed turbine speed, fixed rotor diameter and fixed number of blades to maximize the power output. Blade element momentum tool calculated the power production from the data provided by XFOIL (XFOIL is an interactive program for the design and analysis of subsonic isolated airfoils, ([Drela 1989](#))). Validation studies for BEM tool were carried with a base airfoil of 1 MW capacity turbine. Optimization variables were section chord, section twist, and blade profile at the tip, mid and root. The study reported achievement of 12% increase in power output. [Singh and Ahmed \(2013\)](#) used a specially designed low Reynolds number airfoil, AF300, for designing a small wind turbine blade, operating in low wind velocity of 3 m/s to 6 m/s. Designed blades were mounted on an Air-X wind turbine and tested for a pitch angle of  $15^{\circ}$ ,  $18^{\circ}$  and  $20^{\circ}$ . Performance study showed that the newly developed turbine has an optimum pitch angle of  $18^{\circ}$  and it performs (power output and  $C_p$ ) better than an Air-X wind turbine. And also it showed better start-up response.

[Adu-Gyamfi \(2013\)](#) carried out theoretical optimization study for a low wind speed turbine blade. Ten number of high lift coefficient airfoils were selected and aerodynamic performance was tested under low wind speed (3 m/s) condition at each section of the blade. Optimum performance of each airfoil at different sections was iterated for different tip speed ratios (0.1 to 7.1) and the optimum value was stored in the database. During blade design process, airfoil at each section of the blade was selected based on the airfoil's performance database saved earlier to match the best suitable airfoil at each section of the blade. Likewise, the entire blade was constructed from these ten airfoils for different radial stations. The result showed improved power generation compared to the existing turbine (Evance R9000), indicates that a redesigned blade gave quite a higher output.

In an approach of performance augmentation of SSWT, [Cencelli \*et al.\* \(2006\)](#) modified existing airfoil for each section of a wind turbine blade by blending many airfoils to give an airfoil which performs better than existing airfoils. A blade profile optimisation was achieved by an automated design environment consisting of XFOIL, MATLAB and an optimiser, VisulDOC. Power coefficient ( $C_p$ ) was selected as the objective function used for optimization. The design methodology was validated with experimental result (CSIR). The blade was divided into four sections, viz: root, mid, semi and tip stations were considered for blade design from all the redesigned airfoils. Result gave a higher  $C_p$  value of 12% obtained for the best-designed blade at a wind speed of 6 to 7 m/s.

## **2.3 BOUNDARY LAYER TRIP (BLT)**

To understand the effect of BLT on low Re airfoil drag, [Lyon \*et al.\* \(1997\)](#) carried out studies on three low Reynolds number airfoils- M06-13-128, E374, and SD7037. Experiments were carried out in wind tunnel for a different type of two dimensional and three dimensional BLTs as well as single and multiple configurations over the Re range of  $1 \times 10^5$  to  $3 \times 10^5$ . Surface oil-flow visualization and drag data were collected for different trip configuration. The effect of the different type of trips and their location along the chord length on the drag was studied and compared with the airfoil with no trips for the same working condition. From the experiment, they concluded that compared to single two-dimensional trips, the performance was lower for multiple trips and three-dimensional trips. The sudden drag reduction was observed only in case of thin trips. Performance of thick trips varied incrementally. Chord wise trips location upstream of laminar separation point had little effect on performance. They also reported that the BLT's performance is better in case of the airfoil with smaller LSB than that of with longer LSB.

To get a deep insight into the effect of trip on airfoil performance [Gopalarathnam et al. \(2003\)](#) carried out experimental studies on three airfoils with trips. They carried out experiments on airfoils namely SA7024, SA7025 and SA7026 in a wind tunnel having test section  $2.8 \times 4$  ft cross section and 8 ft long. Studies were carried out for Re of  $1 \times 10^5$  to  $3 \times 10^5$  and five test conditions: clean, trip at 0.1c, 0.2c, 0.3c, and 0.4c (where c indicates the chord length of the airfoil). Trips were fabricated by using multiple layers of pressure sensitive graphics tape of thickness 0.0135 in and length 0.125 in. They were located in such a way that the aft end of the tape was at the specified transition point on the upper surface of the airfoil. Drag polar of each clean airfoil was compared that with the trip. The study showed that for high coefficient of lift ( $C_l$ ) and low Reynolds number, tripped airfoils have low drag than clean airfoil but effect inverted at low  $C_l$  and high Re. Their study concluded that for the airfoils considered in the work , it was not possible to improve the performance of airfoil designed with trips for a variety of working condition compared to the corresponding clean airfoil. The optimum trip location also changed with different working conditions.

[McCrosen et al. \(2010\)](#) tested Clark Y12 airfoil with boundary layer trips (BLT) in seven different positions along the airfoil's chord length and nine different Re between  $6.2 \times 10^4$  and  $2.09 \times 10^5$ . Lift and drag data for angles of attack between  $0^\circ$  and  $24^\circ$  were collected. A two-axis force gauge was used for measuring lift and drag forces. For higher Re, any BLT applied on the airfoil caused a more significant increase in drag than lift. This indicated that the use of BLTs is restricted to Re less than or equal to approximately  $1.35 \times 10^5$ . [Jones et al. \(2008\)](#) performed experiments to compare the effects of full span tape and wire turbulators on low Reynolds number airfoil (Eppler E423) for Re between  $4 \times 10^4$  and  $1.2 \times 10^5$ . For relatively high Re, LSB was found to occur on clean airfoil. For airfoil with tape and wire turbulators, both the tape and wire surface-mounted trips were found to improve lift for low angles of attack, but both were

ineffective at high angles of attack. All trip designs were found to improve lift except at the low Re.

Traub (2011) studied the impact of the zigzag trip on the performance of S8036 airfoil at Re of  $7.5 \times 10^4$  and  $1 \times 10^5$ . Tape trips of height 0.1 mm, 0.2 mm and 0.3 mm were used for the study attached at locations 10% 25% and 40% from leading edge of the foil. Results showed a reduction in the lift for most of the cases he studied and improvement in drag particularly for 25% and 40% trip location were observed. Additionally, trip attachment nearer to the leading edge required greater trip height to be effective. Up to 41% improvement in the lift to drag ratio was reported in the study. Improved performance was observed in the case where partial elimination of LSB was attained, not when the elimination was complete.

In an experimental study conducted by Slangen (2009) to explore the effect of different kind of transition trips, comparison of straight and zigzag strips were made. Trips of different thickness at a different location from leading edge of a flat plate were studied. The thickness of zigzag trips varied from 0.75 mm to 0.9 mm and that for straight strips were 1.5 mm to 2.15 mm. The study was conducted in the air with a flow velocity of 8 m/s. Result revealed that zigzag trips were more efficient than the straight 2D strip.

Boudet *et al.* (2015) reported a novel approach to numerically simulate trip using source-term method and the results were compared with grid-step method. The source term method was simple and yielded a smoother and faster transition. The implementation was easy as the geometrical modifications were not required on the model. The study was conducted on a flat plate at Re of  $1.3 \times 10^6$  and solved with LES approach.

For better performance of the BLT, geometry and position of the trip should be such that the flow transition to turbulent should be completed within the separation bubble

and not after the reattachment (Simens and Gungor 2018). The literature study implies that the performance of BLT is airfoil dependent and its applicability depends on the relative advantage between lift and drag coefficients and hence effect on  $C_l/C_d$  ratio should be studied.

## 2.4 EFFECT OF TUBERCLES ON AIRFOIL PERFORMANCE

Fish and Battle (1995) designed hydrofoil inspired from the observation on whale flipper. The humpback whale flipper has a nearly symmetrical cross section which can be approximated to NACA 63<sub>4</sub>-021 as shown in Figure 2.1. The designed hydrofoil was tested at Re of  $6 \times 10^6$  which equivalent to the flipper moving at 8.8 m/s through sea water. They suggested that the tubercle functions as the flow control device and enhances lift generation at high AOA. They proposed that the momentum exchange in the boundary layer by the stream-wise vortices generated from the tubercles was the reason for performance enhancement of such flippers.

Watts and Fish (2001) also observed the enhanced performance of the tubercled airfoil at higher AOA compared to its baseline. They carried out 3D vortex panel studies on the finite wing of NACA 0021 and presented their result for  $10^\circ$  AOA. Improved performance observed at  $10^\circ$  was vanished at  $0^\circ$  AOA, implying no penalty for the presence of tubercles during a null state. Moreover the study revealed an increase in form drag comparable to the savings in induced drag. Here, 4.8% increase in lift, a 10.9% reduction in induced drag and a 17.6% increase in the lift to drag ratio were observed for the modified model in the study. Also increase in pressure drag by 11% was observed in the viscous drag study.

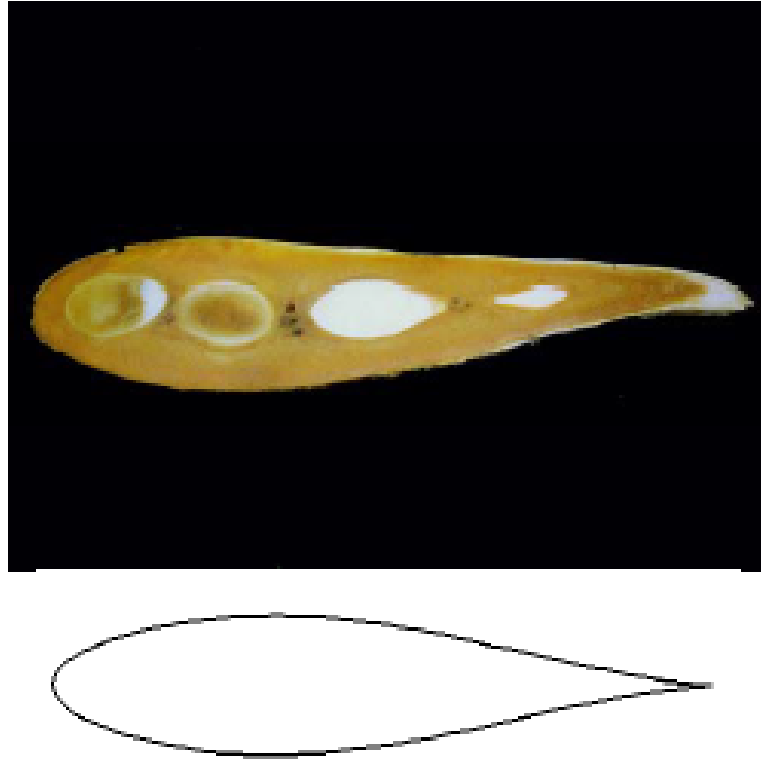


Figure 2.1: Comparison of a Humpback whale pectoral flipper cross section with the NACA 63<sub>4</sub>-021 airfoil profile (Custodio 2007).

A comparative study of smooth and scalloped scaled idealized model study by Miklosovic *et al.* (2004) reported a performance improvement of 6% in maximum lift with no drag penalty at the lower angles of attack range (till 10.3°). The wind tunnel study was conducted in the Re range of  $1.35 \times 10^5$  -  $5.5 \times 10^5$  based on average chord length. Airfoil having NACA 0021 as cross-section was employed for the idealized flipper model and study was conducted for the AOA in the range of 0° - 25°. Results showed an extended stall angle of 16.3° for scalloped wing which was increased by 40% than the smooth model which stalled at 12°. The drag of the modified model had similar value in the lower AOA range and improved thereafter by 32% in the higher AOA range.

Performance degradation in pre-stall condition was reported in some literature. Water tunnel test conducted by Johari *et al.* (2007) reported a reduction in lift and increase in drag force for modified tubercled airfoil model till stall angle of baseline. The study



was conducted on NACA 63<sub>4</sub>-021 for various combination of amplitude and wavelength. Above the stall angle of the baseline model, modified models have up to 50% lift improvement with no drag penalty was obtained. The flow visualization using tufts indicate separated flow in the troughs and attached flow on the peaks of the modified models beyond the post-stall angle of the baseline foil. They reported that the amplitude of the protuberance has a notable effect on the performance of the airfoil than the wavelength. Small wavelength had lesser effect on the performance of airfoil with tubercle (Serson and Meneghini 2015). At higher wavelength, lift generation reduced along with drag reduction resulted in a net decrease in the lift to drag ratio. Hansen *et al.* (2011) reported drag penalty at low angle of attack (AOA). They also observed the amplitude variation effect significantly than that of wavelength.

Effect of tubercle parameters on the performance of airfoil in the pre-stall and post-stall region was studied in-depth by Fernandes *et al.* (2013) on NACA 2412 using  $k - \epsilon$  turbulence model simulation. Different combination of amplitude and wavelength were studied and the results were compared with baseline results. The simulation results were validated with wind tunnel experiments. Extended stall angle was observed for the modified models compared to the baseline model whereas the  $C_{lmax}$  value was higher for the unmodified model. In the pre-stall region lift curve of smaller amplitude models followed the baseline identically while higher amplitude modification was found to generate lift slightly lower than the baseline. The decrease in  $C_l$  in post stall region was more pronounced for the unmodified case than modified. In terms of lift generation in the post-stall region, the larger amplitude was preferred over smaller amplitude. the optimum configuration was found to be with tubercled airfoil model having smaller amplitude and larger wavelength. Here, 5.33% increase in lift and 2.72% reduction in drag was documented in the post-stall operational condition at  $AOA = 28^\circ$ . The even higher lift was achieved at higher AOA without drag penalty. Attached flow was observed over baseline and modified model with least amplitude and highest wavelength. Early flow separation was observed along the peak than the trough. They concluded that the

stream-wise vortex generation was the main cause for the performance improvement. Similarly, [Custodio \(2007\)](#) observed a reduction in the lift and increase in drag in the pre-stall region whereas performance improvement was observed in the post-stall region.

[Cai \*et al.\* \(2018\)](#) investigated the aerodynamic performance of a modified airfoil with a single leading edge protuberance and compared with the baseline NACA 63<sub>4</sub>-021 airfoil. Spalart- Allmaras turbulence model was applied for the numerical simulation. Compared to the sharp decline of baseline lift coefficient, the stall angle of the modified foil decreased and the decline of the lift coefficient became mild. The post-stall performance of the modified airfoil was improved, while the pre-stall performance was declined. Asymmetric flows along the spanwise direction were observed on the modified airfoil, and the local region around one shoulder of the protuberance suffered from leading edge separation at pre-stall angles of attack, which may be responsible for the performance decline. At poststall angles of attack, the attached flows along the peak of the protuberance with a sideward velocity component, would help improving the total performance of the airfoil. Experimental visualization methods, including surface tuft and smoke flow, were performed, and the asymmetric flow pattern past the protuberance was successfully captured. This specific phenomenon may be largely related to the formation of the bi-periodic condition and other complicated flow patterns induced by multiple leading-edge protuberances. The study suggested that The formation mechanism and suppression method of the symmetry breaking phenomenon should be investigated more deeply in the future to guide the practical application of this passive control method.

#### **2.4.1 Flow structure over the airfoil with tubercles**

[Watts and Fish \(2001\)](#) carried out an inviscid simulation study and presented pressure distribution and streamline patterns over a tubercled airfoil model. They observed the

cyclic change in pressure distribution near the leading edge of the modified model. Higher pressure was observed near peak and lower pressure was observed near to trough. The velocity streamlines were closer in trough than peak which indicates the high flow velocity at the trough. The inviscid study could not capture the vortex formation over the model.

Detached eddy simulation (DES) carried out by [Malipeddi \*et al.\* \(2012\)](#) reported the flow forms counter-rotating vortices between the peak and trough, as shown in the [Figure 2.2](#). The flow pattern was of biperiodic. The flow-streamlines emerging from the peak inclined towards trough and then form the vortices. Hydrogen bubble visualization done by [Hansen \*et al.\* \(2009\)](#) revealed the exact flow pattern on NACA 0021 behind the peak and trough. The flow separated early behind trough than that at the peak forming a wider wake behind the trough. The flow streak-lines converge in the trough which indicates the flow accelerated through trough nearer to the leading edge.

[Rostamzadeh \*et al.\* \(2014\)](#) reported the details regarding the formation of a pair of counter-rotating vortices on an airfoil with leading-edge tubercle with the help of shear stress lines as shown in [Figure 2.3](#). The part of streamline coming from the leading edge has spanwise velocity gradient. It resulted in a flow which moved towards the trough and converged to point N2 in the figure and other streamlines moved back towards the trailing edge to form spiral shape with foci F1 and F2. The point N2 serves as the onset of beginning of LSB and point S1 serves as a node of reattachment

[Sudhakar \*et al.\* \(2017\)](#) conducted oil flow visualization study on a typical UAV whose wings were modified to incorporate tubercles on its leading edge at 0.18 and 0.27 million Re and at various AOA. Two types of wings were tested, one with constant amplitude and wavelength (case I) and one with varying amplitude and wavelength (case II). The results were compared with unmodified baseline model to study the ef-

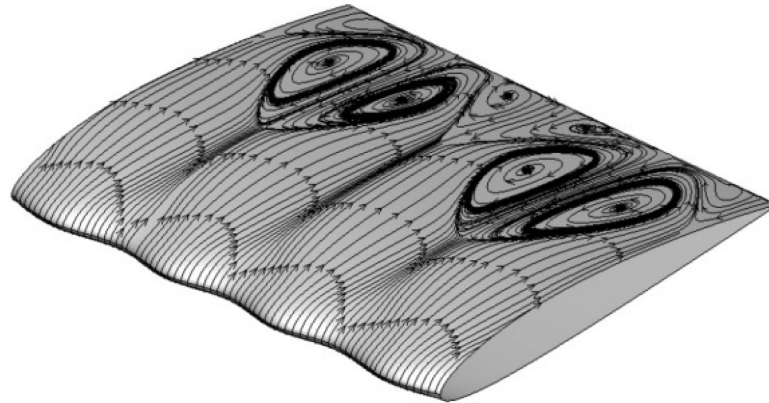


Figure 2.2: Streamline over the tubercled airfoil forming surface vortices (Malipeddi *et al.* 2012)

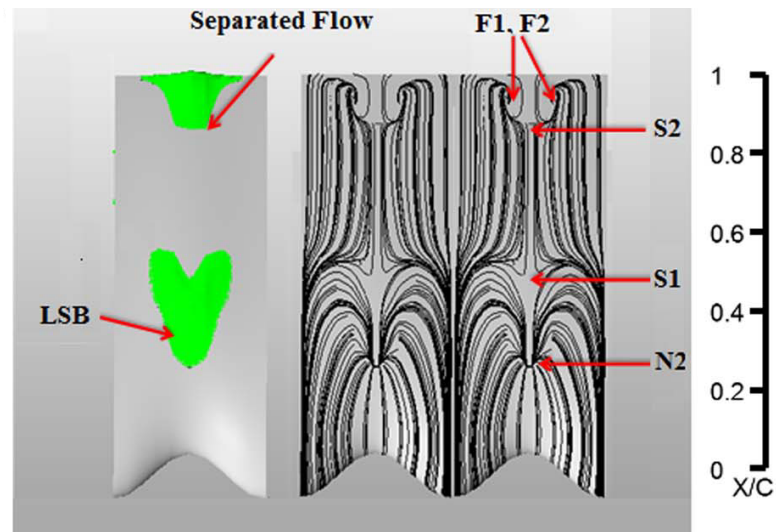


Figure 2.3: Streamlines over tubercled airfoil model NACA 0012 showing onset of separation and re attachment point of LSB (Rostamzadeh *et al.* 2014)

effect of tubercles on the formation of LSB. On the baseline model, clear and straight separation and reattachment regions were observed. On modified wing with case I also LSB was observed in a similar fashion but reduced size (up to 5%) at  $4^\circ$ . A similar pattern was observed for case II also with a reduction in LSB size up to 10% to 20%. But at higher AOA ( $8^\circ$  and  $12^\circ$ ) and  $Re$ , wavy separation and straight reattachment lines were observed.

[Karthikeyan \*et al.\* \(2014\)](#) conducted experimental study on NACA 4415 airfoil at  $Re$  of  $1.2 \times 10^5$  and oil-flow visualization was used for flow pattern study. They observed the onset of separation, dead air region and reverse flow region on the modified and unmodified airfoils with oil-flow visualization. Wavy separation and reattachment line were observed for a modified airfoil at AOA  $6^\circ$ . The tubercle induced three dimensional 'V' shaped bubble pockets with separation apex aligned along the trough region of the leading edge tubercle. [Hansen \(2012\)](#) compared the effects of tubercle on the performance of two different airfoils and reported that performance of tubercle was airfoil dependent. The airfoils with maximum thickness location occurring further aft from the leading edge benefited the most from the tubercles. The study reported the effect of tubercle on LSB and found that LSB was absent in the peak and middle with a shortened bubble in the trough of the tubercles compared to the unmodified airfoil.

[Kim \*et al.\* \(2018\)](#) investigate vortical structures above a three-dimensional wing with tubercles using surface-oil-flow visualization and particle image velocimetry measurement. Two wing models with and without tubercles are considered at the Reynolds number of  $1.8 \times 10^5$  based on the free-stream velocity and mean chord length. At this Reynolds number, tubercles delay the stall angle by  $7^\circ$  and increase the maximum lift coefficient by about 22%. At a low angle of attack, flow separation first occurs near the tip region for both wing models. While flow separation rapidly progresses inboard (toward the wing root) for the model without tubercles with increasing angle of attack, tubercles produce two types of vortical motions and block the inboard progression of flow separation, resulting in delayed stall from AOA =  $8^\circ$  to  $15^\circ$ . One of these two vortical structures is pairs of counter-rotating streamwise vortices evolving from hemispherical separation bubbles near the leading-edge troughs at pre-, near-, and post-stall AOA, and the other is asymmetric pairs of streamwise vortices evolving from separated flow regions after the mid-chord region at near-stall angle of attack. At a post-stall AOA (AOA =  $16^\circ$ ), strong clockwise and counter-clockwise streamwise vortices are generated from foci at the root and tip near the trailing edge, respectively, and delay

flow separation in the mid-span, resulting in a higher lift coefficient than that without tubercles.

[Abate et al. \(2019\)](#) studied different tubercle configurations in terms of amplitude and wavelength applied to the leading edge of the NREL phase VI wind turbine blade. Results in terms of power and annual energy production are compared with the regular NREL phase VI blade notice a considerable improvement in the power for all the cases tested at high wind speed conditions ( $20\text{m/s}$ ), but an opposite trend is visible moving to the design condition ( $10\text{m/s}$ ). The study suggest that, tubercle generate counter-rotating vortices, which block the spanwise flow leading to a stall strength reduction.

#### **2.4.2 Flow mechanism with tubercles**

[Hansen \(2012\)](#) propose that a pair of counter vortices between the peak of the tubercle promotes the flow modification along the stream-wise direction. [Pedro and Kobayashi \(2008\)](#) reported the reason for higher aerodynamic performance for the scalloped flipper was due to the presence of stream-wise vortices originated by the tubercles. The reason why it improves the aerodynamics was of twofold. In the first place the vortices carry momentum to the boundary layer delaying the trailing-edge separation, secondly, these vortices confine the leading edge separation to the tip region.

In a DNS study, [Favier et al. \(2012\)](#) found that a certain combination of amplitude and wavelength of tubercle gives optimum performance. They identified a Kelvin–Helmholtz-like instability driven by the span-wise modulation of the stream-wise velocity profile induced by the wavy leading edge was the reason for the origin of the generation of the stream-wise vortices which control the boundary layer separation.

There are contradictory opinions about the flow mechanism for the improved per-

formance of the airfoil with tubercles. Van Nierop *et al.* (2008) proposed that as the wavelength and amplitude of tubercle were larger than the boundary layer thickness, tubercles cannot act as a vortex generator. Performance difference due to stall angle was commenced due to the redistribution of surface pressure such that separation of the boundary layer was delayed behind the tubercles. Skillen *et al.* (2013) observed a secondary flow induced by the span-wise pressure gradient, that transports the fluid in the low inertia boundary layer behind the peak to suction peak along the trough. High momentum fluid from above seems to replace the boundary layer fluid (thus re-energizing the boundary layer) behind the peak thus delaying the separation.

## 2.5 MOTIVE AND SCOPE OF THE PRESENT WORK

From the detailed literature review presented in the above sections, it is clear that SSWT is promising option to extract wind potential from areas with poor wind spectrum. To design a SSWT for low rated wind speed, high performance ( $C_l/C_d$ ) airfoil is required for its blade cross section. The airfoil E216 is one such a airfoil which generates high  $C_l/C_d$  at low Re situation. Literature study shows that, the performance of the airfoil E216 is less explored and the data base is not available in open literature. The present work involves an exclusive study of performance of the E216 in the prestall region to test its applicability for SSWT design.

The performance of such airfoils degrade due to the presence of LSB in the low Re environment. Literature study reveals that the use of BLT as a passive flow control technique is well acceptable method to control LSB formation. However, the performance of the BLT varies with airfoil and working environment. The effect of BLT on the aerodynamic performance of the airfoil E216 is not reported in the literature. Further, the previous studies have mainly focused on the effect of the position of BLT along chord

wise direction and its height normal to the flow direction on the LSB formation. There is insufficient literature on the effect of cross sectional of BLT shape along with its position and height on the LSB formation and airfoil performance. So the study focused on the performance of BLT of different shapes on the airfoil E216 to check its suitability for SSWT design.

Incorporation of tubercles on leading edge of airfoil is a recent passive flow control technique for airfoil's performance augmentation. Currently, the majority of studies have considered only thick, symmetric foils and wings as they approximate Humpback whale flippers. The effect of tubercles on thin and highly cambered airfoils such as E216 are less reported. Moreover the effect of tubercles on LSB formation is still to be explored.

In view of the great significance of the reliable data base for E216 airfoil as a candidate for SSWT blade design, an independent study is undertaken here to determine aerodynamic performance characteristics of the airfoil E216. The study also involves the effect of the BLT of different cross-section and tubercles of different amplitude and wavelength on the performance of the airfoil E216 in prestall region.

## **2.6 RESEARCH OBJECTIVES**

- To study experimentally and numerically the effect of boundary layer trip of different shapes on LSB formation and performance of airfoil E216.
- To study experimentally and numerically the effect of leading edge tubercle on LSB formation and performance of airfoil E216.



- To investigate, computationally, the effect of boundary layer trip and tubercles on the newly designed SSWT blade.

# CHAPTER 3

## METHODOLOGY

### 3.1 OVERVIEW

This chapter provides description of the facilities and methods for experimental study as well as the numerical analysis. The details of standard equipment and methods are omitted but methodology specific to the study is given in details. Justification of chosen methodology are given wherever necessary. This chapter is divided into two sections, one for experimental and the other for numerical methodology. The experimental methodology section consists of details about the model preparation, measuring instrument and data reduction techniques. Numerical methodology includes the details related to geometry, meshing and solver set-up.

### 3.2 EXPERIMENTAL METHODOLOGY

#### 3.2.1 Airfoil model design and fabrication

The airfoil E216 is used for profile section of the test models in the study (Figure 3.1). The airfoil is modeled using the computer aided drafting package SolidWorks 2010 using the coordinates given in Appendix A, Table A.1. Size of the model is decided considering many factors. Moderate flow speed is required in the wind tunnel to have laminar flow. The blockage induced by the model should be minimum to get accurate results. At the same time, span of the model should be large enough to consider the test as two-dimensional and reduce tip vortices. The model should be stiff enough to reduce velocity-induced vibrations. Along with this, considering previous studies (Lyon *et al.*

1997; Hu and Yang 2008), an aspect ratio 6.33 is chosen for the model. It resulted in 150 mm chord length and 950 mm span with planform area of  $0.143 \text{ m}^2$ . Airfoil model is fabricated from fibre reinforced plastic (FRP).

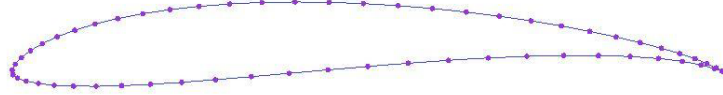


Figure 3.1: Airfoil E216 (maximum thickness = 10:4% at 26:2% of chord (UIUC 2014))

### 3.2.2 Boundary layer trip

The height of BLT is calculated based on the guidelines given by Braslow *et al.* (1966). They proposed the term roughness Reynolds number ( $Re_k$ ) based on roughness height  $k_r$ , velocity on the top of the roughness element  $u_k$  and the kinematic viscosity of the air at that location ( $\nu_k$ ) as given in Equation 3.1. They reported that the value of  $Re_k$  should be 600 to trip the flow to turbulent.

$$Re_k = \frac{u_k k_r}{\nu_k} \quad (3.1)$$

To decide the position of BLT, wind tunnel experiments are conducted for the baseline airfoil at  $6^\circ$  AOA. The  $C_p$  distribution curve shows the presence of LSB at a distance of 22 mm from leading edge (Chapter 4, Figure 4.5). Based on this, the BLT position is decided at 15 mm ( $x/c = 0.10$ ) from leading edge. From the Blasius equation, the boundary layer height at  $x = 15$  mm,

$$\delta = 5 \sqrt{\frac{\nu_x x}{U_\infty}} \quad (3.2)$$

where,

$\nu_x$  = kinematic viscosity of air =  $1.568 \times 10^{-5} \text{ m}^2/\text{s}$

$U_\infty$  = free stream velocity = 10.8 m/s.

The calculated  $\delta$  is  $7.37 \times 10^{-4} \text{ m}$ . From similarity rule inside the boundary layer, a relation can be written as shown in Equation 3.3;

$$\frac{k_r}{\delta} = \frac{u_k}{U_\infty} \quad (3.3)$$

Combining Equations 3.1 and 3.3, the equation for calculating roughness height  $k_r$  can be written as given in Equation 3.4:

$$k = \sqrt{\frac{\delta \nu_k Re_k}{U_\infty}} \quad (3.4)$$

The calculations resulted in a roughness height of 0.71 mm and is the minimum BLT height required for the complete tripping of laminar boundary layer into turbulent boundary layer. Taking this height as reference, four trip heights - 0.3 mm, 0.5 mm, 0.7 mm and 1 mm, are selected for the study. Rectangular (RT), Right angled triangular (RA) and Isosceles triangular (IT) are the different trip height used in the study. Experiments are conducted only for RT trip of different trip heights. The width of the trip is maintained 2 mm for all the cases. Trip is introduced at a distance  $0.17c$  from leading edge for location-1 and at  $0.10c$  for location-2. These locations are chosen after analyzing the location of LSB formation from pressure distribution over the base airfoil. Experiments are carried out at  $Re = 1 \times 10^5$ . Boundary layer trips are made from several layers of masking tape. A number of layers of tape are laminated one over the other, at the required location on the airfoil as shown in Figure 2. Ten number of layers of tape is used to make 1 mm trip thickness. Width of trip is kept 3 mm and is fixed along the span at required chord-wise location. Each set of experiments started with highest trip height of 1 mm and required trip height for subsequent experiments is achieved by removing layers of tape from existing height.

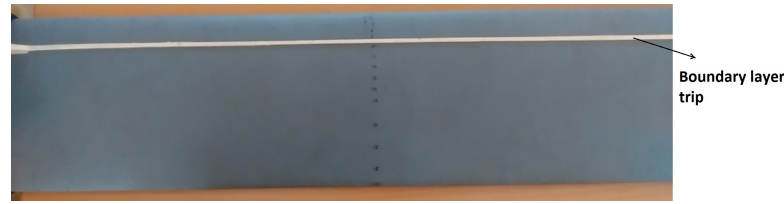


Figure 3.2: Airfoil with trip

### 3.2.3 Tubercled airfoil model

Tubercles are the bio-inspired modification on leading edge of the airfoil. [Fish and Battle \(1995\)](#) determined the average normalised amplitude ( $A/\bar{c}$ ) and wavelength ( $W/\bar{c}$ ) of tubercles to be 0.05 and 0.415 respectively. Required amplitudes and wavelengths are calculated by multiplying this ratio by the model chord length of 150 mm which results in  $A \approx 8\text{mm}$  and  $W \approx 64\text{mm}$ . As far as a small scale wind turbine blade is concerned, a higher amplitude and wavelength than the calculated one may invite structural challenges. So the study is carried out with two more lesser amplitudes (2 mm and 4 mm) and wavelengths (15.5 mm and 32 mm). The models are named as 'A(x)W(y)' where 'x' and 'y' represent the corresponding amplitude and wavelength in mm. The detailed nomenclature is shown in [Figure 3.3](#). Three type of tubercle configurations, A2W15.5, A4W31 and A8W62, are used for the experiment and are shown in [Figure 3.4](#).

The models are drafted in SolidWorks2010. The airfoil profile E216 is lofted through two guidelines, sinusoidal curve at leading edge and straight edge at trailing edge to required length. The sinusoidal guidelines curve is created using equation driven spline method with required amplitude and wavelength values. The lofting process generated three dimensional model with varying chord length along the span. The models are fabricated from FRP with total of 56 number of pressure ports on its surface to capture surface pressure on the model.

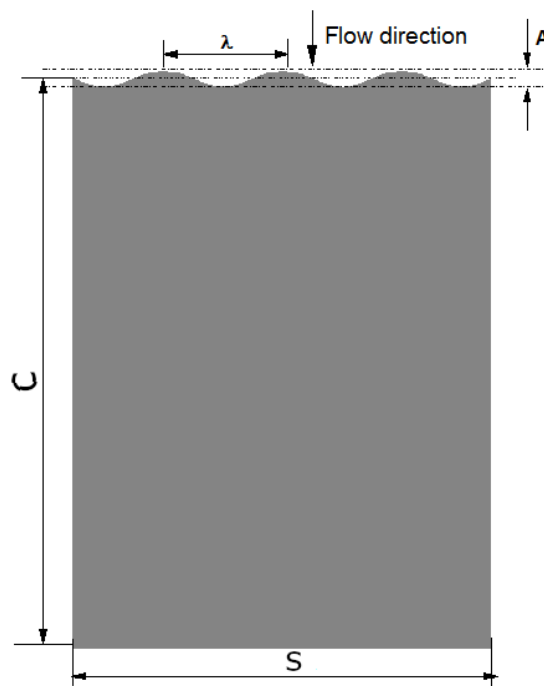


Figure 3.3: Tubercled model showing the nomenclature and dimensions used for simulation

### 3.2.4 Wind tunnel

The experiments are conducted in subsonic open type wind tunnel facility in the Mechanical Engineering Department of National Institute of Technology Karnataka, India and is shown in the Figure 3.5. The tunnel has 1000 mm  $\times$  1000 mm  $\times$  2000 mm square test section with air flow speed range of 0 to 35 m/s. The tunnel is of suction type with empty test section turbulence level less than 0.71% over the tunnel operating range. Further details are listed in Table 3.1. The test model is mounted at 475 mm from entry of the test section.

### 3.2.5 Pressure measurements

To ensure high degree of accuracy, commercially available HTC make PM-6202 model electronic differential manometer is used and is shown in Figure 3.6. The pressure measurement system is pre-calibrated by the manufacturer. This system needs only zero

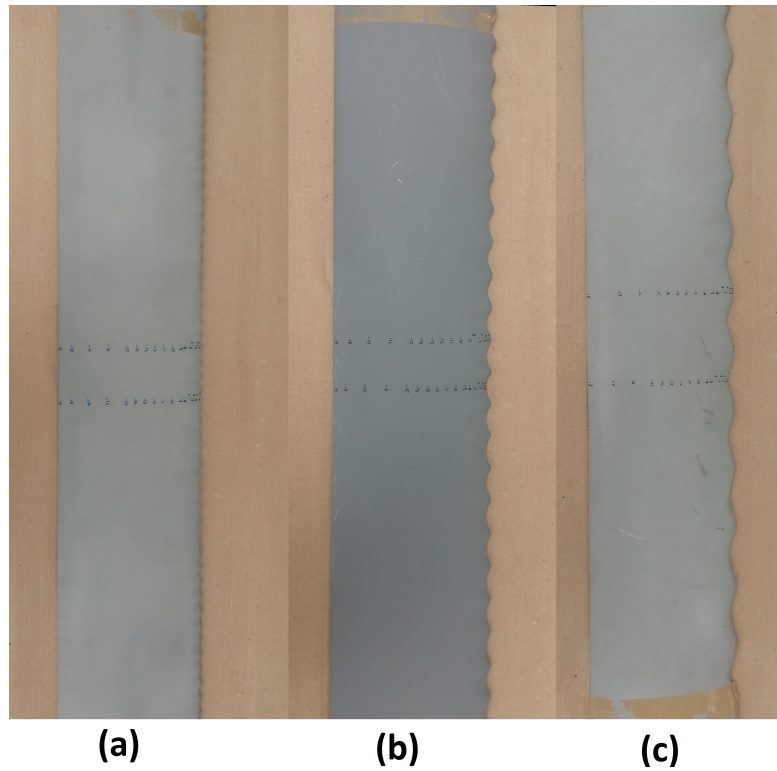


Figure 3.4: Tubercled models used for experiment: (a) A2W15.5, (b) A4W31 and (c) A8W62



Figure 3.5: Subsonic wind tunnel facility at National Institute of Technology Karnataka, India

Table 3.1: Wind tunnel specifications

Type of Tunnel	:Subsonic, Open circuit, Suction type.
Test Section	:1000 mm × 1000 mm × 2000 mm
Air Speed (Velocity)	:30 meters/ sec
Contraction Ratio	:9:1
Contraction length	:2.25 m
Drive	:Axial Flow Fan with AC Motor and speed controller
Overall Size	:4 m × 4 m × 13.5 m (Approx.)
Power Requirement	:A.C 15 HP (11 kW), 440 volts



Figure 3.6: Electronic differential manometer (Make:HTC, Model: PM-6202)

correction prior to the experiment and appropriate offset are determined automatically. The measurement range of manometer is  $\pm 2\text{psi}$  with an accuracy of  $\pm 0.3\%$ . One end of the manometer is connected to pressure port from the airfoil model and the other end is open to atmosphere.

### Surface pressure measurement

The surface pressure measurement is useful in interpreting transition points, separation points and separation bubbles. The static surface pressure is measured using pressure taps provided on the airfoil surface and the recorded values are used to calculate lift force on the airfoil and the procedure is explained in the succeeding section.



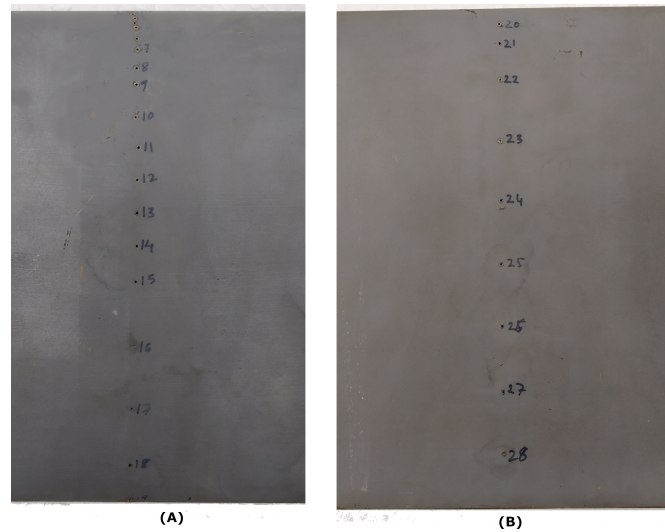


Figure 3.7: Pressure taps on baseline airfoil: (a) suction surface and (b) pressure surface

### Pressure taps

The models are incorporated with static pressure taps on the upper and lower surface. Stainless tubes of 0.50 mm inner diameter are internally connected to airfoil surface through the holes drilled on the model surface. The small diameter hole reduces the uncertainty of the pressure measurement. All the SS tubing are bend and passed through a bigger SS tube of outer diameter 12 mm. The bigger tube passed through one side of the model where the maximum camber exist. The bigger tube served as a guide for small tubes and portion of the tube projecting from the model served as support in the wind tunnel test section. The small tubes coming out from the model is connected to flexible vinyl tubing through which it communicates with pressure sensor.

The baseline test model is provided with 28 static pressure taps located near the midspan out of which 19 pressure taps are located on suction side and 9 on the pressure side as shown in Figure 3.7. Chord wise locations of the pressure taps on the airfoil are listed in Table 3.2.

Unlike the baseline model, two rows of pressure ports are provided on the tubercled

Table 3.2: Location of pressure ports from leading edge of the airfoil

Upper surface										
Port no.	1	2	3	4	5	6	7	8	9	10
Location (mm)	0	1.5	3	4.5	6	9	12	15	18	23
Upper surface										
Port no.	11	12	13	14	15	16	17	18	19	
Location (mm)	32	41	50	59	68	78	97	117	142	
Lower surface										
Port no.	20	21	22	23	24	25	26	27	28	
Location (mm)	6	12	23	41	59	78	97	117	135	

model. One row of pressure ports capture the pressure variation along the crest and one along the trough. Each row consists of 28 pressure ports with 19 on upper surface and 9 on the lower surface. The ports are unevenly spaced with more number towards leading edge .

### Coefficient of Lift calculation from surface pressure measurement

The  $C_l$  is calculated from surface pressure distribution ( $h_i$ ) over the airfoil model which is obtained from pressure port readings as explained by [Multhopp \(1950\)](#). Free stream static pressure ( $h_\infty$ ) and total pressures ( $h_0$ ) are measured using Pitot-static tube located upstream of model mounted in wind tunnel. From these pressure measurements  $C_p$  is calculated using Equation 3.5.

$$C_p = \frac{h_0 - h_i}{h_0 - h_\infty} \quad (3.5)$$

The normal force component  $C_n$  and tangential force component  $C_t$  is calculated from the line integral of  $C_p$  around the airfoil curve outline, s using trapezoidal rule as given in equations 3.6 and 3.7.

$$C_n = \oint_s C_p \frac{dx}{c} \quad (3.6)$$

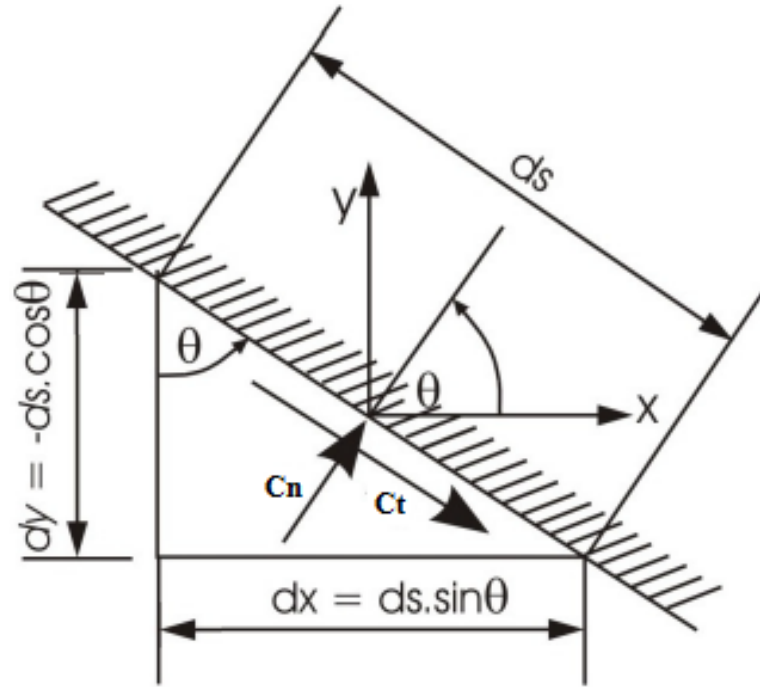


Figure 3.8: A discrete element on the airfoil surface of length  $ds$  showing the resolved components of forces (Hansen 2012)

$$C_t = \oint_s C_p \frac{dy}{c} \quad (3.7)$$

where,

$$dx = ds \sin \theta$$

$$dy = -ds \cos \theta$$

$c$  = airfoil chord length

$ds$  = Nearby pressure port distance (Figure 3.8)

The values of  $C_n$  and  $C_t$  are calculated through integration using the trapezoidal rule. The lift generated by the airfoil has contribution from both normal and tangential force coefficients as shown in Figure 3.8 and lift coefficient,  $C_l$ , can be calculated from the Equation 3.8.

$$C_l = C_n \cos \alpha - C_t \sin \alpha \quad (3.8)$$

where  $\alpha$  is AOA in degrees.

### 3.2.6 Pitot tube measurements

A pitot-static tube of 1.5 mm diameter is used for measurement of local flow velocity inside the wind tunnel. The pitot-static tube is used for the measurement of both free stream and wake velocity. The free stream velocity,  $U_\infty$ , is measured using the Equation 3.9 in the empty tunnel keeping the pitot tube at position where model is kept in the test section.

$$\rho_w g \Delta h_w = \frac{1}{2} \rho_a U_\infty^2 \quad (3.9)$$

Here  $\Delta h_w$  is the difference of pressures, total and static, measured in terms of difference in height of water column.

### Coefficient of Drag measurement from wake survey

Wake survey method, as represented in Figure 3.9, is used to measure  $C_d$  of the model. The Pitot tube is mounted downstream of the test model to measure the wake created by the model in the flow. The pitot tube is mounted at a distance of  $1.5c$  from the trailing edge of the model to ensure sufficient settlement of highly turbulent wake. The pitot tube is mounted on a manually operated vertical traverse system. The pitot tube is lowered in 5 mm spacial increment starting from  $3c$  above and  $3c$  below the centre of the tunnel. Loss in momentum in the flow behind the airfoil model in terms of momentum thickness is used to calculate the  $C_d$  of the airfoil using the Equation 3.10 (Melville Jones 1937).

$$C_d = \frac{2}{c} \int_L^U \sqrt{\frac{p_0(y) - p(y)}{p_0 - p_\infty}} \left( 1 - \sqrt{\frac{p_0(y) - p(y)}{p_0 - p_\infty}} \right) dy \quad (3.10)$$

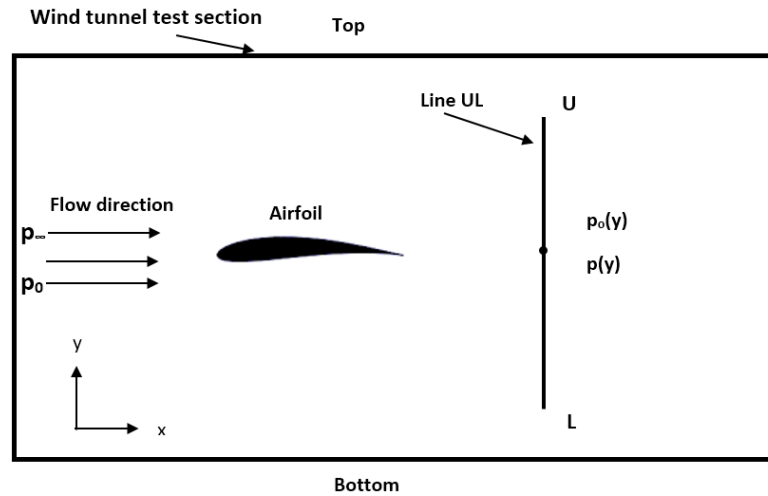


Figure 3.9: Schematic of wake survey method

where  $p_0(y)$  is the total pressure at each point on the measured line  $UL$  along  $y$  direction from top of the tunnel,  $U$  to bottom of the tunnel,  $L$  behind the airfoil trailing edge,  $p(y)$  is the static pressure measured at the same point,  $p_0$  is the free stream total pressure and  $p_\infty$  is the free stream static pressure. These equations are solved through numerical integration using the trapezoidal rule.

### 3.2.7 Wind tunnel boundary layer profile

The model mounted in the wind tunnel and tunnel wall had an airgap of 25 mm provided for the free movement of model while changing AOA. It is essential to prove that the air-gap is less than the boundary layer thickness of the tunnel wall to eliminate wing vortices and consider the experiment to be two dimensional without spanwise flow. Therefore boundary layer measurements are carried out in the wind tunnel using boundary layer probe.

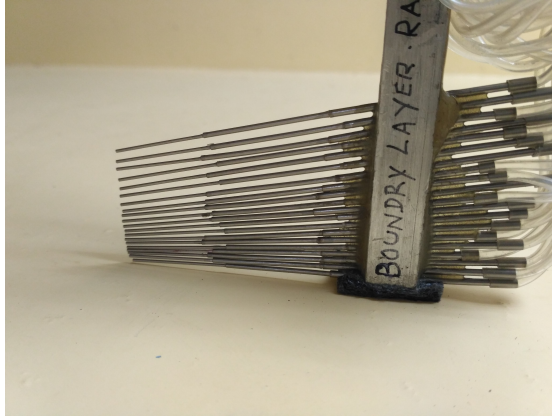


Figure 3.10: Boundary layer probe

### 3.2.8 Boundary layer probe measurements

The boundary layer probe (shown in Figure 3.10) had 20 SS tubes of 0.25 mm internal diameter inclined down at  $15^\circ$  to capture pressure distribution very close to wind tunnel wall. The pressure is measured using the electronic pressure transducer. Using this probe, pressure at twenty different vertical position is measured at a time. The location details of the probes is listed in Table 3.3.

Local velocity,  $u$  at different vertical direction ( $y$ ) from wind tunnel wall surface is measured till the local velocity becomes equals to 0.99 times of free stream velocity,  $U_\infty$ . Boundary layer profile  $u/U_\infty$  is plotted against similarity variable,  $\zeta$  and is shown in Figure 3.11 (where  $\zeta = \frac{y}{2x}\sqrt{Re_x}$ ,  $y$  = vertical distance of measuring probe from tunnel wall,  $x$  = boundary layer development length and  $Re_e = Re$  based on distance  $x$ ). The  $\zeta$  value 10000 represents a boundary layer height of 36.1 mm.

The boundary layer thickness,  $\delta^*$  and momentum thickness,  $\theta$  are calculated for this vertical distance using the equations 3.11 and 3.12 respectively.

$$\delta^0 = \int_0^\delta \left(1 - \frac{u}{U_\infty}\right) dy \quad (3.11)$$

$$\theta = \int_0^\delta \frac{u}{U_\infty} \left(1 - \frac{u}{U_\infty}\right) dy \quad (3.12)$$

Table 3.3: Probe locations for boundary layer measurement

Probe number	Distance (mm)
1	0.5
2	1
3	2
4	3.5
5	4
6	5.5
7	7.5
8	9
9	11
10	13
11	14.5
12	16
13	18
14	20
15	22
16	24
17	27
18	28
19	31
20	34.5

Trapezoidal rule is used to numerically solve the above equations. Calculations showed a boundary layer thickness of 35.01 mm and momentum thickness of 26.73 mm from the wall. This resulted in a shape factor value of 1.31, and it shows that the boundary layer is turbulent.

### 3.2.9 Wind tunnel turbulence intensity

Turbulence intensity (TI) represents the velocity fluctuation in the wind tunnel and should be low as possible to get reliable result. It represents the velocity fluctuation in the wind tunnel. The TI of wind tunnel in the present work is calculated based on the assumption that TI is isotropic in nature ([Schlichting and Gersten 2016](#)). Therefore,

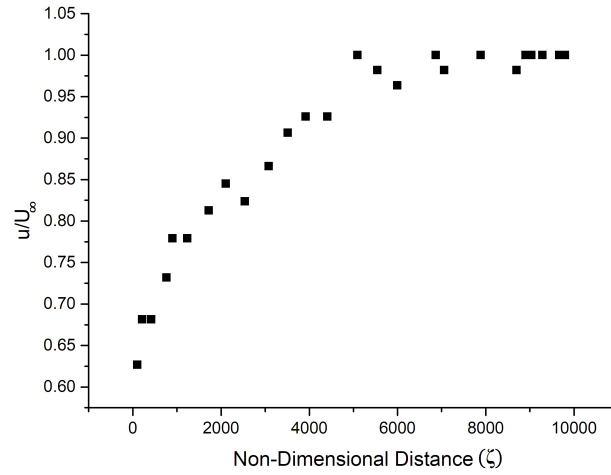


Figure 3.11: Boundary layer profile

simplified Equation 3.13 is used for TI calculation.

$$TI = \frac{\sqrt{\overline{u'^2}}}{U_\infty} \quad (3.13)$$

where,  $u'$  is the fluctuating velocity component in streamwise direction.

The TI for a free stream velocity of 10.8 m/s is calculated at different points in a plain at 425 mm from inlet of test section, which is the location of leading edge of the model. Measurements are carried out on a total of  $4 \times 4 = 16$  number of equi-distant points in the plane. The TI of the tunnel is found to have average value of 0.12%

### 3.2.10 Wind tunnel corrections

Flow inside a wind tunnel is bounded by its side wall. To resemble the flow as a open field flow and to reduce the measurement errors, necessary corrections have to be incorporated into the measured data and are called wind tunnel corrections. The guidelines provided by Barlow *et al.* (2015) and Selig and McGranahan (2004) are followed in



the study. Solid blockage, wake blockage and streamline curvature are the corrections considered in the study. Buoyancy correction and downwash corrections are not incorporated here.

Solid blockage,  $\varepsilon_{sb}$ , is due to the presence of a model within the wind tunnel test section which results in reduction of effective area through which the air flows. Solid blockage correction factor is calculated from Equation 3.14. Here,  $t$  is the model thickness,  $h$  is the tunnel cross sectional height and  $\lambda_s$  is shape factor whose value is 1.5 as per the recommendation by Barlow *et al.* (2015) for a wing spanning the tunnel.

$$\varepsilon_{sb} = 0.822\lambda_s \frac{t^2}{h^2} \quad (3.14)$$

Wake blockage,  $\varepsilon_{wb}$ , is caused by a decreased local pressure in the airfoil wake which causes higher flow velocity outside the wake than free stream. The correction factor,  $\varepsilon_{wb}$  is calculated from the Equation 3.15 (Selig and McGranahan 2004).

$$\varepsilon_{wb} = \frac{c}{2h_{ts}} C_{du} \quad (3.15)$$

where  $h_{ts}$  is the test section height and  $C_{du}$  is the uncorrected drag coefficient. Streamline curvature around the airfoil is affected by wind tunnel walls and it results in induced pseudo camber of airfoil in the test section. This pseudo camber increases the lift generation. The correction factor,  $\sigma$  is calculated using the Equation 3.16 (Selig and McGranahan 2004).

$$\sigma = \frac{\pi^2}{48} \left( \frac{c}{h_{ts}} \right)^2 \quad (3.16)$$

Finally, corrected parameters combining all the blockage corrections are calculated using equations 3.17 - 3.19:

$$U = U_u(1 + \varepsilon) \quad (3.17)$$

where,  $\varepsilon = \varepsilon_{sb} + \varepsilon_{wb}$

$$C_l = C_{lu}(1 - \sigma - 2\varepsilon) \quad (3.18)$$

$$C_d = C_{du}(1 - 3\varepsilon_{sb} - 2\varepsilon_{wb}) \quad (3.19)$$

where  $\varepsilon_b = \varepsilon_{sb} + \varepsilon_{wb}$ . For the baseline model at highest prestall AOA of  $12^\circ$ , following values for correction factors are obtained:

$$\begin{aligned} \varepsilon_{sb} &= 3 \times 10^{-4} \\ \varepsilon_{wb} &= 6.08 \times 10^{-3} \\ \sigma &= 4.63 \times 10^{-3} \end{aligned}$$

The calculated correction factors are very small and negligible. Hence wind tunnel corrections are not incorporated in the study.

### 3.3 UNCERTAINTIES IN THE EXPERIMENT

Uncertainty of electronic manometer used in the experiment for measuring pressure is  $\pm 0.03\%$ . Uncertainty in derived quantity is calculated as explained in reference [Kline and McClintock \(1953\)](#). If  $R$  is a given function of the independent variables  $x_1, x_2, x_3, \dots, x_n$ . Thus,

$$R = R(x_1, x_2, \dots, x_n) \quad (3.20)$$

Let  $\omega_R$  be the uncertainty in the  $R$  and  $\omega_1, \omega_2, \dots, \omega_n$  be the uncertainties in the independent variables. Then,

$$\omega_R = \left[ \left( \frac{R}{x_1} \omega_1 \right)^2 + \left( \frac{R}{x_2} \omega_2 \right)^2 + \dots + \left( \frac{R}{x_n} \omega_n \right)^2 \right]^{1/2} \quad (3.21)$$

The maximum uncertainties in derived parameters are shown in Table 3.4. The details of uncertainties in each parameters are given in Tables C.1 and C.2 of Appendix C.

Table 3.4: Uncertainty in derived parameters

$C_p$	$\pm 0.60\%$
$C_l$	$\pm 3.74\%$
$C_d$	$\pm 1.77\%$
$C_l/C_d$	$\pm 5.69\%$

### 3.4 REPEATABILITY

The repeatability of results is an important concern in wind tunnel experimentation. It demonstrates reliability of experimental set up to reproduce experimental data under similar circumstances. The baseline airfoil's performance test is assessed for same Re of  $1 \times 10^5$  and environmental conditions and is shown in Fogure 3.12. The maximum deviation is found to be less than 10%.

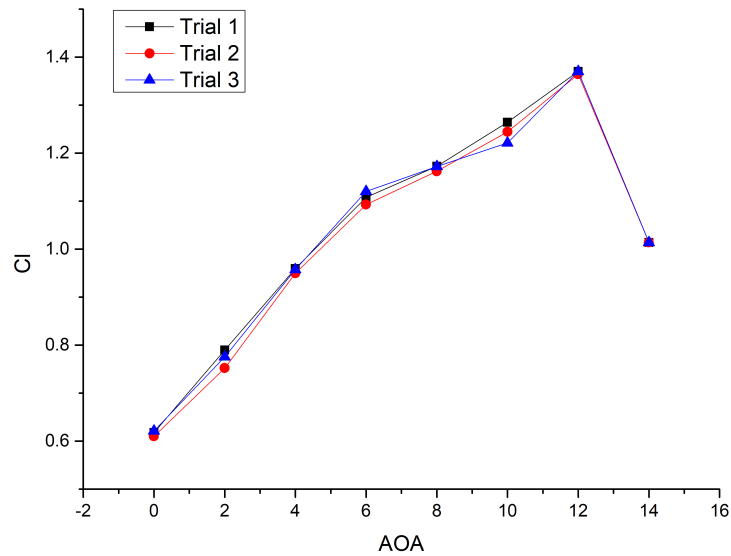


Figure 3.12: Repeatability of the experiment

## 3.5 NUMERICAL METHODOLOGY

### 3.5.1 Geometry

All required geometries for the simulation works are created using drafting software SolidWorks2010. Two sets of airfoil geometries are created, one set is two dimensional which is used for the study on the effect of BLT on the airfoil performance. The other set is for three dimensional geometries used for the study of effect of tubercles on the performance of the airfoil. The airfoil E216 is used as the profile shape for all the cases.

The baseline two dimensional geometry is created by importing coordinate points from a text file downloaded from [UIUC \(2014\)](#). The coordinates are scaled appropriately to get chord length of 150 mm. The imported points are joined using splines to obtain required geometries. Three kind of trip shapes are used in the study namely, rectangular (RT), right angled triangular (RA) and isosceles triangular (IT) and are shown in Figure 3.13. Width of all the trips is 2 mm. The geometry of the modified airfoils with BLT are created by editing the baseline airfoil by drafting the additional shape using line options in the software.

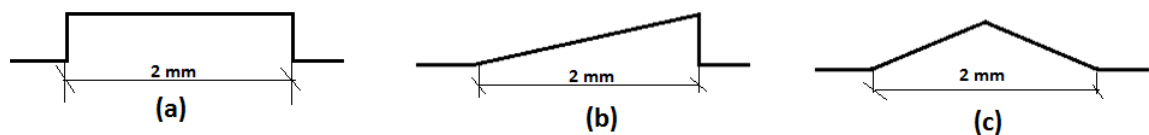


Figure 3.13: Different shapes of BLT used in the study: (a) rectangle, (b) right-angled triangle, (c) isosceles triangle

The three dimensional baseline geometry is created by lofting baseline profile shape through a straight guide line of length 124 mm. For the models with tubercles, the lofting is carried out through a pair of guidelines as explained previously. The profile curve is lofted through these curves which resulted in a geometry with varying chord

Table 3.5: Tubercled model parameters

		Wavelength(mm)		
		15.5	31	62
Amplitude(mm)	2	A2W15.5	A2W31	A2W62
	4	A4W15.5	A4W31	A4W62
	8	A8W15.5	A8W31	A8W62

length with appropriate scaling of baseline profile as shown in Figure 3.14

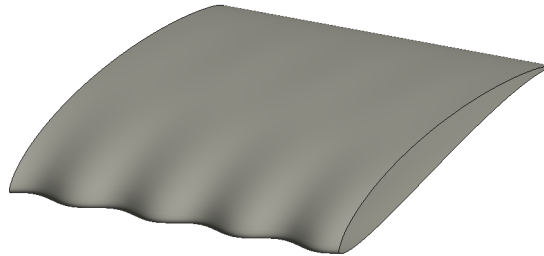


Figure 3.14: Tubercle geometry created through lofting

The study is carried out with different kind of tubercles of various amplitude and wavelength. The tubercles are formed with combination of three amplitudes - 2 mm, 4 mm, and 6 mm and three wavelength of 15.5 mm 31 mm and 62 mm which result in nine different models. The details of the amplitude and the wavelength of each tubercle model studied in the work are given in the Table 3.5.

### 3.5.2 Computational domain and mesh

The computational domain and meshes are created using ICEM CFD of ANSYS 15.0. Structured grid is used for the simulation.

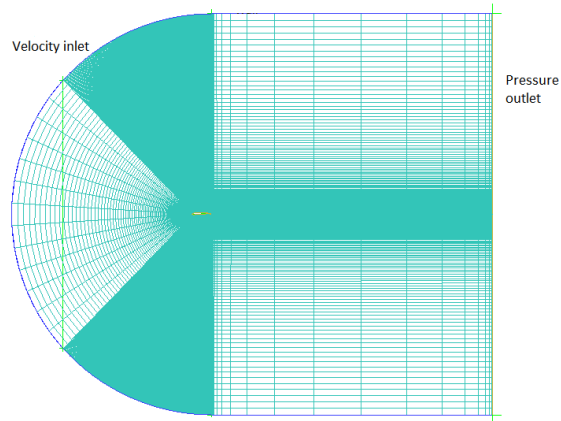


Figure 3.15: Far view of structured grid in the domain with boundary conditions

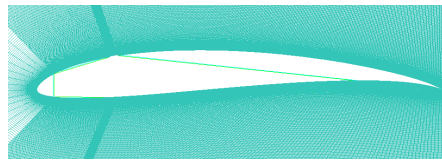


Figure 3.16: Close view of dense grid around the airfoil

### Boundary layer trip

A C-type two dimensional computational domain with structured grid is used for the BLT simulation which is shown in Figure 3.15. The computational domain has a length of  $9c$  in front of airfoil to achieve fully developed flow and  $15c$  behind the airfoil. The width is kept to 20 times the chord (Eleni *et al.* 2012). The resolution of the mesh is higher in the region close to the airfoil where greater computational accuracy is needed and it is as shown in Figures 3.16 & 3.17. As per the requirements of the turbulent models used, the height of the first cell adjacent to the surface is set such that it results in  $y^+$  value less than one.

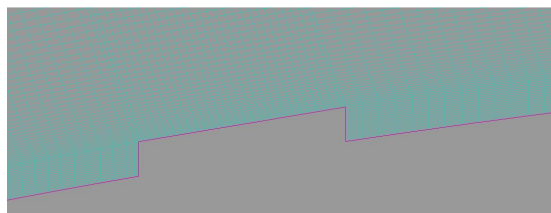


Figure 3.17: Grid configuration near to BLT

## Tubercles

The three-dimensional computational domain of rectangular shape is used for the tubercle simulation. Total length of the computational domain is set to be 25 times the chord length to achieve fully developed flow, — 9c in front of airfoil and 15c behind the airfoil. The width is kept to 20 times the chord as shown in Figure 3.18. Three dimensional structured mesh is created as shown in Figure 3.19. High resolution mesh is created in the region close to the airfoil as shown in figures 3.16 and 3.21. The height of the first cell adjacent to the surface is set such that it resulted in  $y^+$  value less than one.

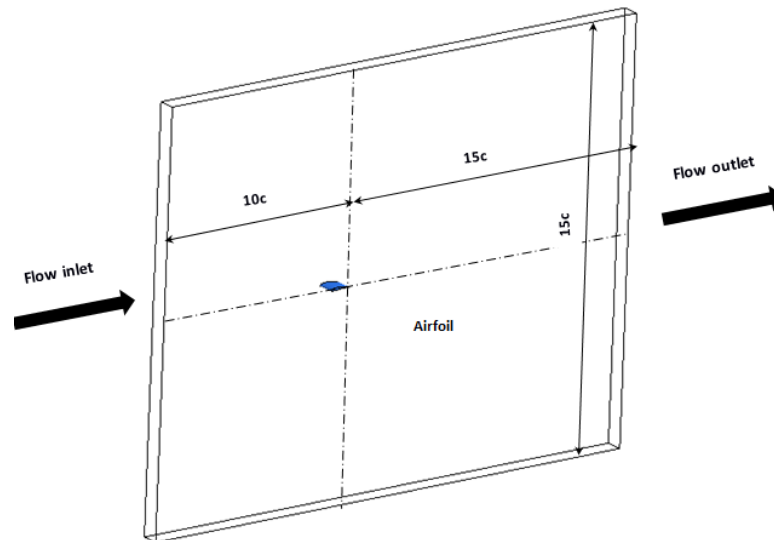


Figure 3.18: Computational domain

### 3.5.3 Boundary conditions and solver setup

No slip boundary condition is imposed on the airfoil with velocity inlet at flow inlet, symmetry condition at side walls and pressure outlet at outlet of the domain. Free stream temperature for calculating the fluid properties is selected as 308 K, same as the environmental temperature in which baseline experiments are carried out and other required properties of the fluid are calculated accordingly. For Re of  $1 \times 10^5$ , and

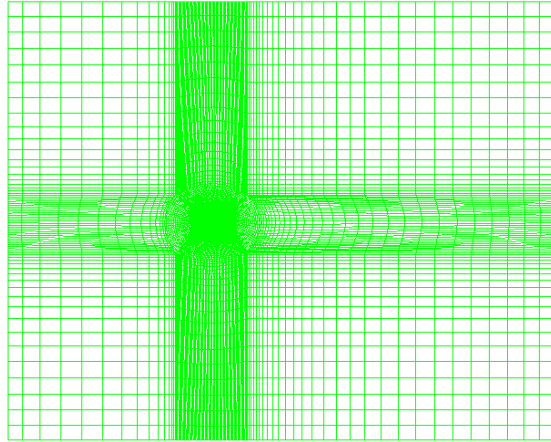


Figure 3.19: Far view of structured grid in the domain

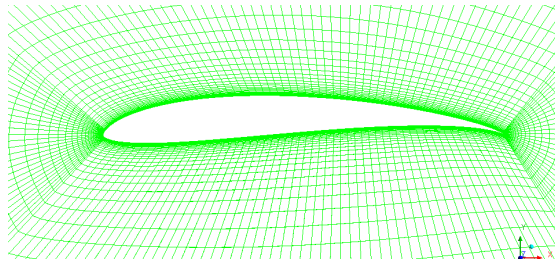


Figure 3.20: Close view of dense grid nearer to the airfoil

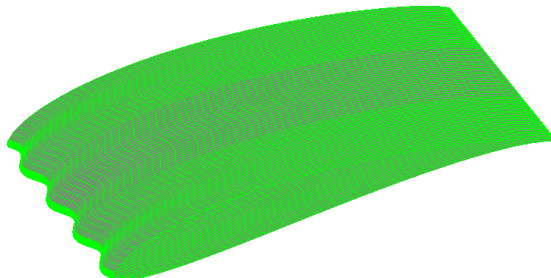


Figure 3.21: Grid on the airfoil surface



airfoil chord length of 150 mm, free stream inlet velocity of air is calculated to be 10.08 m/s. The turbulent intensity of the flow is set to 0.12%, which is equal to the turbulent intensity in the wind tunnel. Flow is considered as incompressible. To solve momentum equations semi-implicit method for pressure linked equations (SIMPLE) algorithm (FLUENT 2014) and second order upwind spacial discretization are employed in the calculations. Least square cell based spacial gradient is fixed for spacial gradient. Residual target of  $10^{-6}$  is fixed as convergence criteria.

### 3.5.4 Turbulence model

Langtry-Menter 4-equation Transitional SST Model or  $\gamma - Re_{\theta}$  - SST model is used in the study (Menter *et al.* 2006). It is based on the two-equation  $k - \omega$  SST model, augmented by two additional equations, one for intermittency ( $\gamma$ ) and another for transitional Reynolds number ( $Re_{\theta t}$ ) to describe the laminar-turbulent transition process. Intermittency term is employed to activate the production term of the turbulent kinetic energy (TKE), downstream of the transition point in the boundary layer, and the Transition Reynolds number term captures the non-local effect of the turbulence intensity (Menter *et al.* (2006)). The governing equations involved in this analysis are listed below (Menter *et al.* 2006; FLUENT 2014; Shah *et al.* 2015).

The transport equation for the intermittency term  $\gamma$  is given in Equation 3.22.

$$\frac{\partial(\rho\gamma)}{\partial t} + \frac{\partial(\rho U_j \gamma)}{\partial x_j} = P_{\gamma 1} - E_{\gamma 1} + P_{\gamma 2} - E_{\gamma 2} + \frac{\partial}{\partial x_j} \left[ \left( \mu + \frac{\mu_t}{\sigma_\gamma} \right) \frac{\partial \gamma}{\partial x_j} \right] \quad (3.22)$$

The transition source terms in the Equation 3.22 are,

$$P_{\gamma 1} = 2F_{length}\rho S[\gamma F_{onset}]^{c_{\gamma 3}} \quad (3.23)$$

$$E_{\gamma 1} = P_{\gamma 1}\gamma \quad (3.24)$$

where  $S$  represents the strain rate magnitude and  $F_{length}$  is an empirical correlation that controls the length of the transition region. Destruction source terms are given by ,

$$P_{\gamma 2} = c_{a2}\rho\Omega\gamma F_{turb} \quad (3.25)$$

$$E_{\gamma 2} = c_{e2}P_{\gamma 2}\gamma \quad (3.26)$$

here,  $\Omega$  represents vorticity magnitude. The functions which control transition onset,  $F_{onset}$  are:

$$Re_v = \frac{\rho y^2 S}{\mu} \quad (3.27)$$

$$R_T = \frac{\rho k}{\mu\omega} \quad (3.28)$$

$$F_{onset1} = \frac{Re_v}{2.193Re_{\theta c}} \quad (3.29)$$

$$F_{onset2} = \min(\max(F_{onset1}, F_{onset1}^4), 2.0) \quad (3.30)$$

$$F_{onset3} = \max\left(1 - \left(\frac{R_T}{2.5}\right)^3, 0\right) \quad (3.31)$$

$$F_{onset} = \max(F_{onset2} - F_{onset3}, 0) \quad (3.32)$$

$$F_{turb} = e^{-\left(\frac{R_T}{4}\right)^4} \quad (3.33)$$

here  $Re_{\theta c}$  is the critical Reynolds number where the intermittency first starts to increase in the boundary layer and  $y$  is wall distance. This may find upstream of the transition Reynolds number  $\tilde{Re}_{\theta t}$  and the difference between the two must be obtained from an empirical correlation. Both the  $F_{length}$  and  $Re_{\theta c}$  correlations are functions of  $\tilde{Re}_{\theta t}$ . The terms  $Re_v$  is the strain rate Reynolds number,  $k$  is the turbulent kinetic

energy,  $\omega$  is specific turbulence dissipation rate and  $Re_T$  is viscosity ratio Reynolds number. The value of constants used in the intermittency equations are,  $c_{\gamma 1} = 0.06$ ;  $c_{e2} = 50$ ;  $c_{\gamma 3} = 0.5$  and  $\sigma_{\gamma} = 1.0$ .

Equation for transition momentum thickness number,  $\tilde{Re}_{\theta t}$ , is given by Equation 3.34.

$$\frac{\partial(\rho \tilde{Re}_{\theta t})}{\partial t} + \frac{\partial(\rho U_j \tilde{Re}_{\theta t})}{\partial x_j} = P_{\theta t} + \frac{\partial}{\partial x_j} \left[ \sigma_{\theta t} (\mu + \mu_t) \frac{\partial \tilde{Re}_{\theta t}}{\partial x_j} \right] \quad (3.34)$$

where  $P_{\theta t} = c_{\theta t} \frac{\rho}{t} (Re_{\theta t} - \tilde{Re}_{\theta t})(1.0 - F_{\theta t})$ ,  $t = \frac{500\mu}{\rho U^2}$  and  $F_{\theta t}$  is the blending function used to turn off the source term in the boundary layer (FLUENT 2014; Menter *et al.* 2006; Shah *et al.* 2015).

Values of the constants in the Equation 3.34 are,  $c_{\theta t} = 0.03$  and  $\sigma_{\theta t} = 2.0$ . In the present work to get better and reliable results, the following values are used in the simulations (Fagbenro *et al.* 2014; Shah *et al.* 2015);  $c_{\theta t} = 0.02$ ;  $\sigma_{\theta t} = 3.0$ .

### Separation - induced transition correction

The model, without the correction predicts the turbulent reattachment location far downstream compared to experimental results (Menter *et al.* 2006). This is because the TKE,  $k$ , in the separating shear layer is smaller at lower free stream turbulence intensities. As a result, it takes longer for TKE to grow to large enough values that would cause the boundary layer to reattach. To correct this deficiency, a modification to the transition model is introduced that allows TKE to grow rapidly once the laminar boundary layer separates. Separation-induced transition can be re written as,

$$\gamma_{sep} = \min \left[ 2 \cdot \max \left[ \left( \frac{Re_v}{3.235 Re_{\theta c}} \right) - 1, 0 \right] F_{reattach}, 2 \right] F_{\theta t} \quad (3.35)$$

where

$$F_{reattach} = e^{-\left(\frac{Re_T}{20}\right)^4} \quad (3.36)$$

$$\gamma_{eff} = \max(\gamma, \gamma_{sep}) \quad (3.37)$$

### Coupling the Transition Model with SST Transport Equations

The transition model interacts with the SST turbulence model with modification in the  $k$ -equation as below:

$$\frac{\partial(\rho k)}{\partial t} + \frac{\partial(\rho u_i k)}{\partial x_i} = \frac{\partial}{\partial x_i} \left( \Gamma_k \frac{\partial k}{\partial x_j} \right) + G_k^* - Y_k^* + S_k \quad (3.38)$$

where,

$$Y_k^* = \min(\max(\gamma_{eff}, 0.1), 1.0) Y_k \quad (3.39)$$

and

$$G_k^* = \gamma_{eff} G_k \quad (3.40)$$

where  $Y_k$  and  $G_k$  are the terms representing original destruction and production respectively for the SST model. The production term in the  $\omega$ -equation is used without any modification.

### 3.5.5 Grid independent study

#### For two dimensional grid

Grid independence test is conducted with five sets of meshes ranging from 10,000 to 610,000 elements. Grid independent tests are carried for baseline, RT, RA and IT BLTs of 1mm trip height. Then same pattern mesh is used for respective trip shapes with all other trip heights. The  $C_l$  and  $C_d$  are the parameters checked for the grid consistency. The simulations are carried out for AOA of  $6^\circ$  and the results for baseline test are shown in Figure 3.22. After around 475,000 grid cells there is no significant variation in lift coefficient and hence it is considered as appropriate mesh size for the baseline model.

Table 3.6: Grid number used for different kind of BLT model

Model	Number of elements
RT	535,000
RA	507,000
IT	512,000

Similar procedure is followed for modified models and the Table 3.6 shows the final selected grid number which has given satisfactory results.

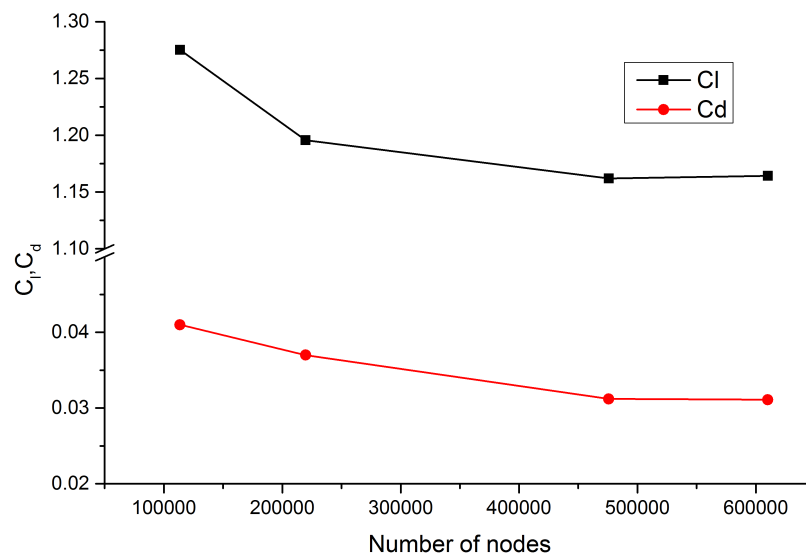


Figure 3.22: Effect of number of grid cells on lift and drag coefficient for baseline airfoil at  $6^\circ$  AOA

### For three dimensional grid

Grid independent study is carried out for baseline and A8W15 tubercled model. Five different meshes are prepared for grid independent study with number of grid cells ranging from 700,362 to 21,41,000. Simulations are carried out for AOA of  $6^\circ$ . The results for baseline is shown in Fogure 3.23. After around 1,237,620 grid cells there is no significant variation in  $C_l$  and  $C_d$  and hence it is considered as appropriate mesh size for baseline simulation. Similarly 1,319,430 elements are seen to form a mesh for

independent results in case of the tubercled model. Similar studies are also performed for the rest of tubercled model.

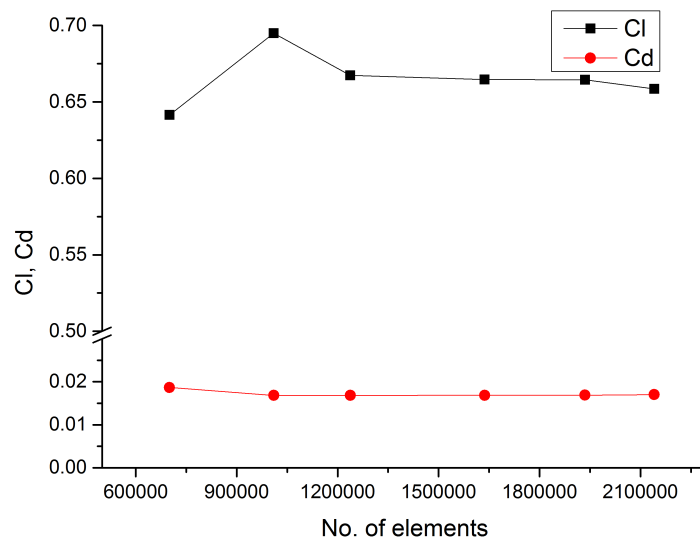


Figure 3.23: Variation of  $C_l$  and  $C_d$  of the baseline airfoil with grid number at AOA of  $6^\circ$

## 3.6 DESIGN OF WIND TURBINE BLADE

Wind turbine blade is designed based on BEM theory. Design elements like type of airfoil, expected angle of attack (AOA), blade diameter, chord distribution, pitch distribution etc. are required to be calculated for complete blade design.

### 3.6.1 Size of wind turbine

Turbines are generally designed for a particular power output. Design procedure for turbine starts with deciding the power output required from the turbine for its application. Also knowledge about average wind speed is required to calculate diameter ( $D$ )

of turbine from the power equation (Equation 3.41) of the turbine (Kishore 2013).

$$P = \eta \frac{1}{2} \rho A_s U_\alpha^3 \quad (3.41)$$

where  $\eta$  is the overall efficiency of turbine (including generator losses) and  $A_s$  is the swept area of turbine,  $A_s = \frac{\pi}{4} D^2$ . From the literature the value of  $\eta$  lies in the range of 20-25% for SSWT.

### 3.6.2 Blade shape

Pitch distribution and chord distribution determines the shape of blade. For finding pitch and chord distributions entire blade is divided into N number of segments and respective section pitch and section chords are calculated from BEM theory equations by iterative approach as mentioned below (Manwell *et al.* 2010) :

1. **Relative wind speed:** Relative wind velocity is used to calculate Reynolds number. Relative wind velocity and relative wind angle with wake rotation is calculated through iteration with initial assumed values for axial and angular induction factors ( $a = 0$  and  $a' = 0$ ) from equations 3.42 & 3.45.

$$U_{rel} = \sqrt{[(1 - a)U_\alpha]^2 + [(1 + a')\omega r]^2} \quad (3.42)$$

where  $\omega$  is the angular rotational velocity of turbine blade and r is the radial distance of section at which the section considered.

2. **Reynolds number:** Reynold number of the section considered for the wind velocity  $U_{rel}$  is calculated from Equation 3.43:

$$Re = \frac{\rho c U_{rel}}{\mu}. \quad (3.43)$$

where  $c$  represents the section chord length and is given by Equation 3.44;

$$c = \frac{8\pi r \sin\phi}{3BC_l\lambda_r}, \quad (3.44)$$

and  $\mu$  represents dynamic viscosity of the air

3. **Relative wind angle:** Relative wind angle  $\phi$  is calculated from Equation 3.45.

$$\tan\phi = \frac{(1-a)U_\alpha}{(1+a')\omega r} \quad (3.45)$$

4. **Section pitch angle:** Section pitch angle,  $\beta$  is calculated from the Equation 3.46 at each radial sections.

$$\alpha = \phi - \beta \quad (3.46)$$

5. **The over all blade loss factor:** Total blade loss factor  $F$  is calculated using the Equation 3.47 as given below.

$$F = F_{tip} * F_{hub} \quad (3.47)$$

where,  $F_{tip}$  is the tip loss factor given by Equation 3.48:

$$F_{tip} = \frac{2}{\pi} \cos^{-1} \left[ e^{-\frac{B(r_t-r)}{2r \sin\phi}} \right] \quad (3.48)$$

and  $F_{hub}$  accounts the aerodynamic losses from flow over turbine hub, which is given by Equation 3.49;

$$F_{hub} = \frac{2}{\pi} \cos^{-1} \left[ e^{-\frac{B(r-r_h)}{2r_h \sin\phi}} \right]. \quad (3.49)$$

6. **Axial and angular induction factor:** Axial and angular induction factors are calculated from the following equations 3.50, 3.51 and 3.53.



if,  $a < 0.4$ ;

$$a = \left[ 1 + \frac{4F \sin^2 \phi}{\frac{cB}{2\phi r} (C_l \cos \phi + C_d \sin \phi)} \right]^{-1} \quad (3.50)$$

if  $a > 0.4$ ;

$$a = \frac{18F - 20 - 3\sqrt{C_T(50 - 36F) + 12F(3F - 4)}}{36F - 50} \quad (3.51)$$

where  $C_T$  is the thrust coefficient which is calculated as given by Equation 3.52:

$$C_T = \frac{8}{9} + (4F - \frac{40}{9})a + (\frac{50}{9} - 4F)a^2 \quad (3.52)$$

$$a' = \frac{1}{2} \left[ -1 + \sqrt{1 + \frac{4}{\lambda_r^2} a(1 - a)} \right] \quad (3.53)$$

Above steps from 1 to 5 repeated until convergence for  $a$  and  $a'$  are obtained.

7. **Power output prediction from the blade:** after calculating all the above parameters for entire blade section Equation 3.54 is used for calculating the total power output from the blade.

$$C_P = \frac{8}{\lambda^2} \int_{\lambda_r}^{\lambda} F \sin^2 \phi (\cos \phi - \lambda \sin \phi) (\sin \phi + \lambda_r \cos \phi) \left[ 1 - \frac{C_d}{C_l} \cot \phi \right] \lambda_r^2 d\lambda_r \quad (3.54)$$

Flow chart for the blade design is shown in Figure 3.24 and the Matlab code is given in Appendix B.

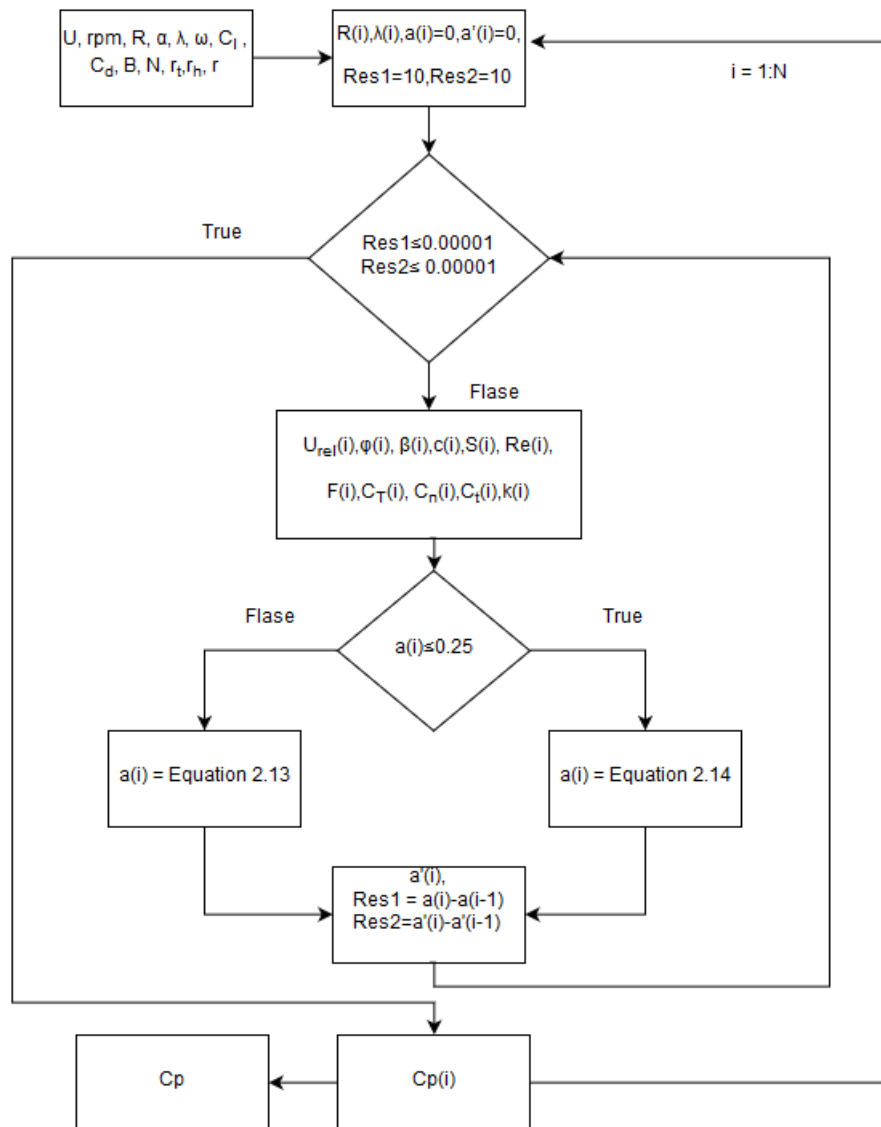


Figure 3.24: Flow chart for BEM code



## CHAPTER 4

### RESULTS AND DISCUSSION

#### 4.1 OVERVIEW

This chapter provides results of experimental study as well as the numerical analysis and related discussion on the results. This chapter is divided into three sections; viz. results of airfoil selection, baseline experimental results, experimental and numerical results for airfoil with BLT and experimental and numerical results for airfoil with tubercles.

#### 4.2 AIRFOIL SELECTION

Selection of an appropriate airfoil for the wind turbine blade is the first step towards achieving good performance from a small-scale wind turbine (SSWT). Wind turbine power generation is proportional to the ratio of coefficient of lift to coefficient of drag ( $C_l/C_d$ ) of the airfoil. Therefore, airfoil selection is based on the value of  $C_l/C_d$  for various AOA at design Re. Airfoil which gives highest  $C_l/C_d$  at the design Re is selected for the blade design. Performance of more than 60 low Re airfoils is studied in XFOIL ([Drela and Youngren 2001](#)) for range of AOA of  $0^0$  to  $20^0$  and at Re of 100,000 - calculated based on relative wind speed, corresponding to free stream wind velocity 6.5 m/s. Figure 4.1 presents the  $C_l/C_d$  vs AOA plot for six high performance airfoils amongst the sixty. The result shows that airfoil E216 has a peak value of 70.65 at an AOA of  $6^0$  and is selected for the further study.

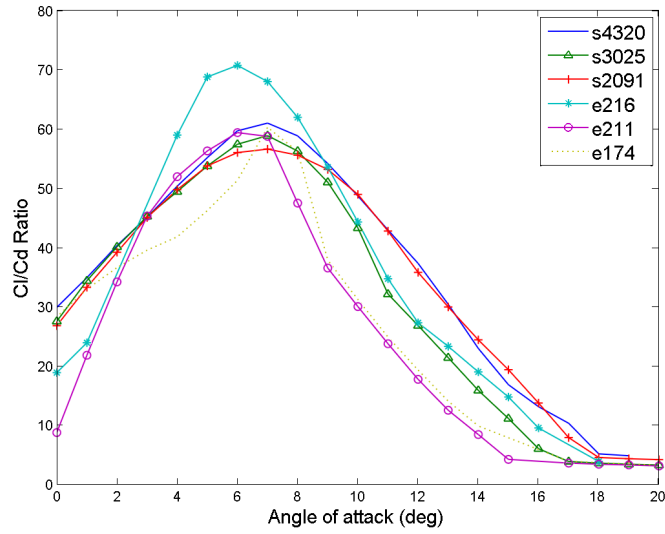


Figure 4.1: Variation of  $C_l/C_d$  with AOA

### 4.3 AERODYNAMIC PERFORMANCE OF AIRFOIL E216

Figures 4.2 and 4.3 show the experimental aerodynamic performance results of the airfoil E216 for various AOA at Re of 100,000. Maximum lift coefficient of 1.37 at an AOA of  $12^\circ$  is obtained in the experiment. Beyond this AOA lift value drops which indicates onset of stall. Drag coefficient ( $C_d$ ) is calculated from wake survey and is inaccurate beyond stall angle and hence the results are limited to AOA upto  $12^\circ$ . At this AOA, the  $C_d$  value of 0.081 is obtained. The maximum value of 42.5 is obtained for the  $C_l/C_d$  at AOA of  $4^\circ$  and is presented in Figure 4.3.

Simulation results are validated with experimental results and are shown in Figures 4.2 and 4.3. These results are in good agreement with the experimental measurements, especially in the pre-stall region. Numerical results do not exhibit completely satisfactory match in the stall region where the flow is highly unsteady (Rahimi *et al.* 2014). The  $C_l$  value of 1.37 and  $C_d$  value of 0.068 is obtained at stall angle of  $12^\circ$ . The average

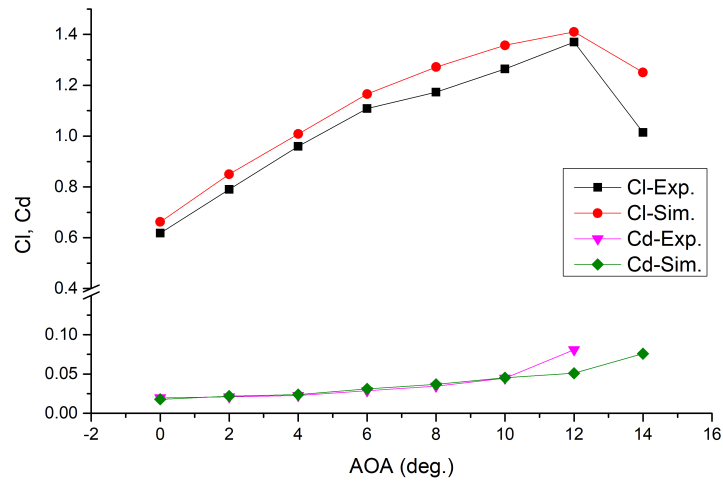


Figure 4.2:  $C_l$  and  $C_d$  results obtained from experiment and simulation as a function of AOA

deviation in  $C_l$  by 8.67% and in  $C_d$  by 5.4% is observed between simulation and experimental results. Peak value of 42.50 is observed for  $C_l/C_d$  at AOA of  $4^\circ$  with average deviation of 6.57% compared to experimental results. Deviation in results between simulation and experiment fall in the acceptable range. The 2D simulation is carried out and compared with wind tunnel experiment in which the spanwise effects (3D effects) are counted. The airfoil surface roughness is not considered in the simulation. The fluid property variation such as humidity and other impurity are also not accounted in simulation. Accumulated errors arising from this factor have resulted in the deviation of simulation results from experimental results.

## 4.4 LAMINAR SEPARATION BUBBLE

Presence and location of LSB on the airfoil can be identified from the coefficient of surface pressure ( $C_p$ ) distribution (Russell 1979). If LSB is present, there will be a plateau in the  $C_p$  distribution of the airfoil as shown in Figure 4.4. The constant pressure line

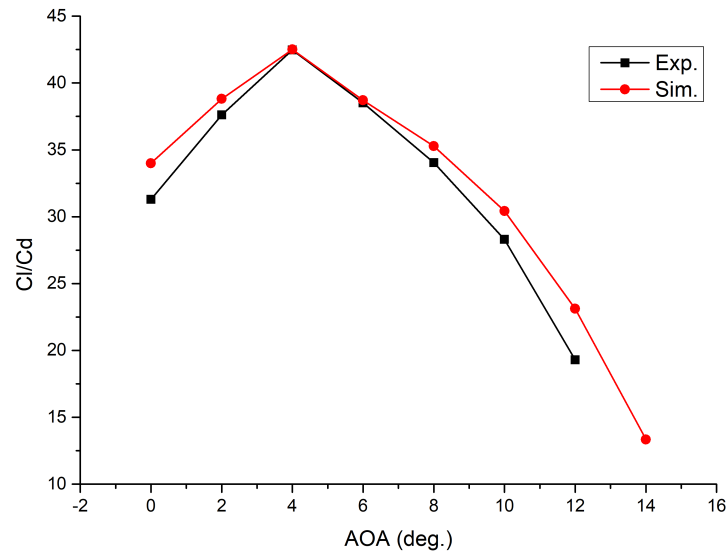


Figure 4.3:  $C_l/C_d$  obtained from experiment and simulation as a function of AOA

represents laminar separation and sudden increase in pressure represents re-energization of boundary layer called the transition region and finally it attaches over the airfoil surface as represented in the Figure 4.4. The region between the point of separation to point of reattachment represents LSB.

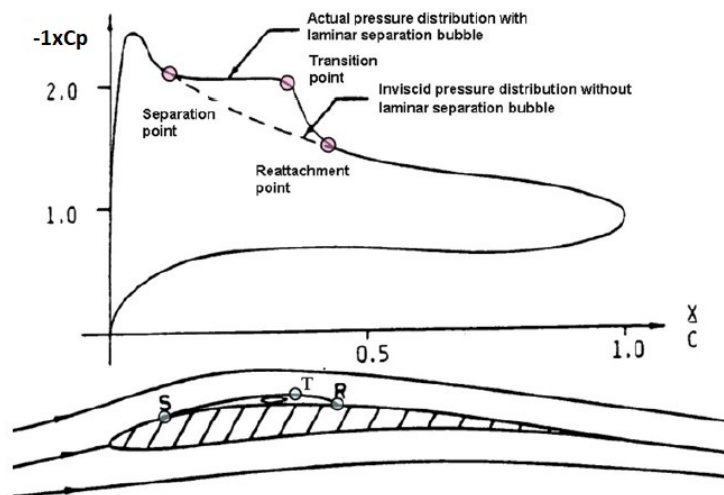


Figure 4.4:  $C_p$  distribution over a typical airfoil (Russell 1979)

In the  $C_p$  distribution from the experiment shown in Figure 4.5, a pressure plateau can be observed after a chordwise distance of  $x/c = 0.22$ . Expected pressure variation is smooth without hump. The pressure hump can be observed for a short length on the suction side of the airfoil. The hump consists of constant pressure regime followed by sharp change in  $C_p$ . The starting point of constant pressure regime, marked by point S, represents the beginning of laminar boundary layer separation from the airfoil surface. The pressure value remains constant till transition begins, represented by the point T. After this constant pressure regime (point T), the separated laminar boundary layer mixes with the fluid and this fluid entrainment re-energises the shear layer and increases the pressure rapidly, making a sudden variation in  $C_p$  (Horton 1968). This region is considered as transition region (T-R). The energized shear layer re-attaches to the airfoil surface as attached flow. The point where the actual pressure distribution coincides with that of an inviscid flow represents the point of reattachment (point R). This phenomenon of flow separation and reattachment is called LSB. In the plot (Figure 4.5), S to R represents LSB region and it starts at  $0.22c$  and ends at  $0.65c$  from the leading edge. The same is observed with oil flow visualisation as shown in Figure 4.6. The dense pigment formation (between S & R) is the indication of LSB and the location exactly matches with that observed from the  $C_p$  distribution (Figure 4.5).

The  $C_p$  distribution from the numerical study over the airfoil at an angle attack of  $6^\circ$  is compared with experimental results and is shown in Figure 4.5. The comparison is made for the reliability of numerical study. It can be seen that the numerical result matches well with that of experimental and the transition location is predicted accurately.

The experimental facilities are limited and hence numerical study is carried out for further investigation of the behaviour of LSB and the corresponding flow structure at different working condition.



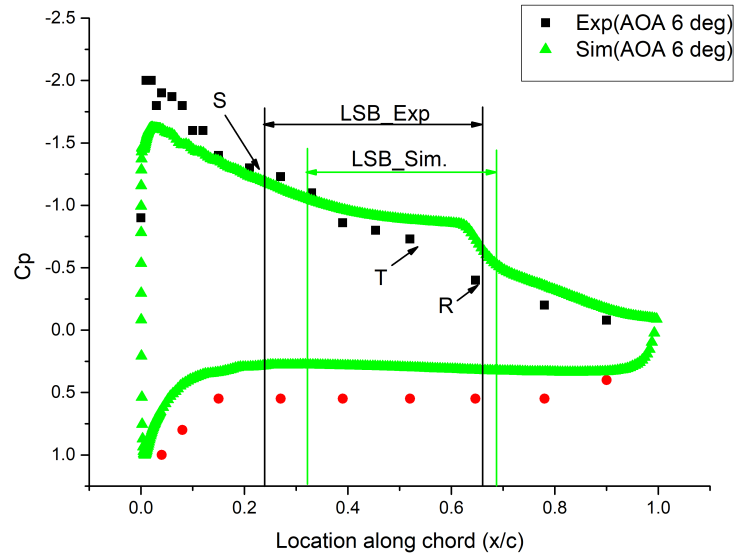


Figure 4.5: Comparison of numerical and experimental result for  $C_p$  distribution over the airfoil at AOA of  $6^\circ$

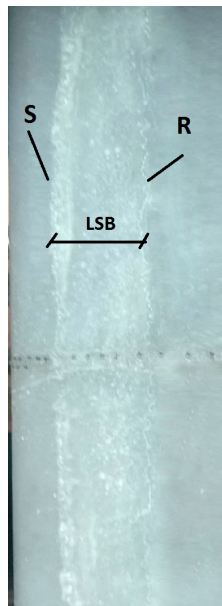
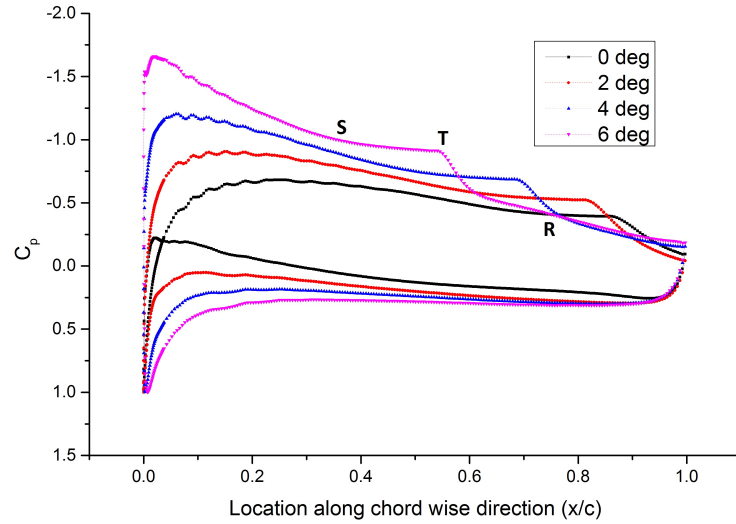
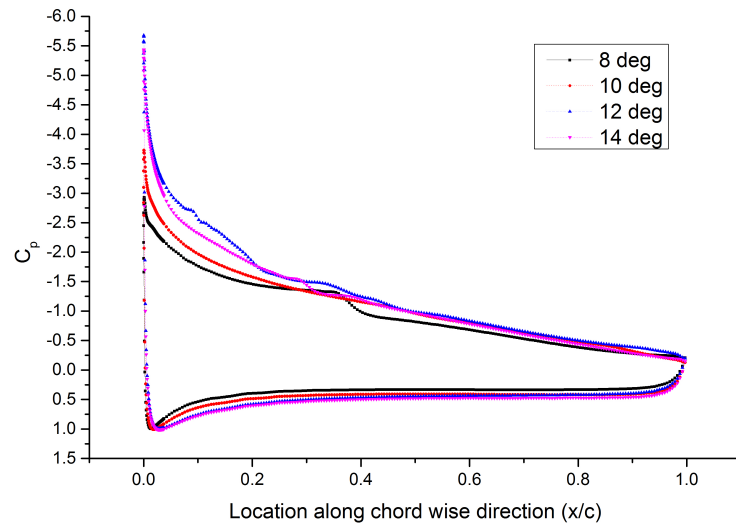


Figure 4.6: Oil flow visualisation on E216 airfoil at AOA of  $6^\circ$

#### 4.4.1 Simulation results for coefficient of surface pressure distribution ( $C_p$ )



(a)



(b)

Figure 4.7:  $C_p$  distribution over the airfoil at different AOA

Figure 4.7 represents simulation results for the  $C_p$  distribution over the airfoil at different AOA. Suction pressure peak increases with increase in AOA. Highest suction pressure peak is observed for AOA of  $14^\circ$  (Figure 4.7b) and lowest is observed for  $0^\circ$  (Figure 4.7a). The area covered by  $C_p$  curve is a representation of lift generated by

airfoil. The area enclosed by the curve increases with increase in AOA till  $12^\circ$  then it slightly reduced. It indicates the lift generation increases till AOA  $12^\circ$  then it reduced which is evident from Figure 4.2.

From the  $C_p$  curves for the airfoil in the Figures 4.7a and 4.7b, pressure plateau is observed from AOA of  $0^\circ$  to  $10^\circ$  similar to that observed in the experiment. As explained in the previous section, the pressure plateau indicates the presence of LSB on the suction surface of the airfoil. The location of the LSB formation moves upstream with increase in AOA. At low AOA, the LSB is formed nearer to trailing edge. As AOA increases, the LSB moves towards leading edge till AOA of  $10^\circ$ . When the AOA is greater than  $10^\circ$  the bubble coalesces with the free-stream flow and no LSB is formed there after. The size of the LSB also changes with respect to the AOA. To investigate this phenomena in detail, location of separation, transition and reattachment point along the airfoil chord, for different AOA, are plotted and shown in Figure 4.8. Along with the location shift of LSB, contraction of size is also observed with increase in AOA. Increase in AOA results in shortening of laminar region and turbulent region of the LSB. Reduction in turbulent region results in steep pressure rise as shown in Figure 4.7. The longest LSB is observed for AOA of  $0^\circ$  which covers 38.5% of airfoil surface area whereas for shortest, which is observed at  $8^\circ$ , it covers 20%.

#### 4.4.2 Velocity vector plot

The exact flow pattern within laminar separation bubble is shown in Figures 4.9 and 4.10. The flow before LSB formation is laminar and moves towards trailing edge. Due to APG, the laminar boundary layer separates from airfoil surface and gradually changes its direction and form reversed flow represented clearly in Figure 4.7b with increase in length of velocity vector line. At the beginning of flow reversal, the vector length is small then it increases to highest and further reduces to minimum, which represents the

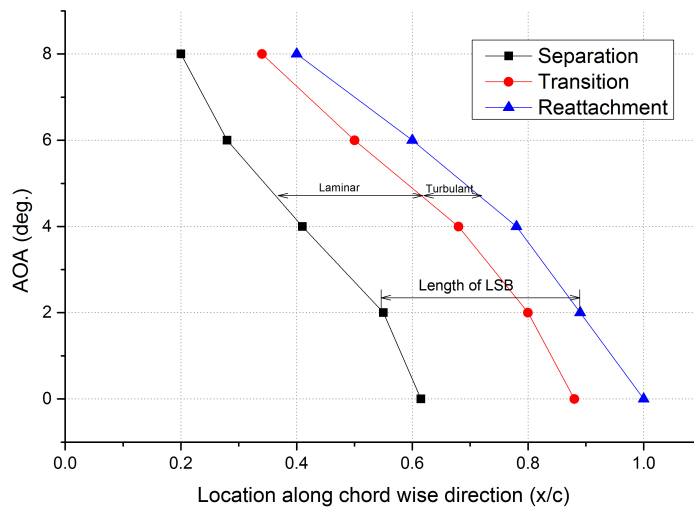


Figure 4.8: Location of LSB for different AOA

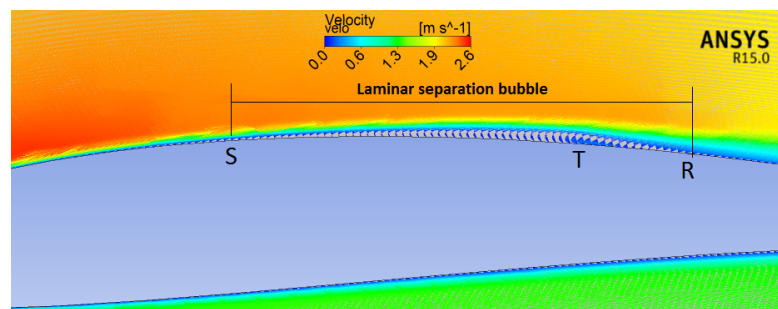


Figure 4.9: Velocity vector plot showing LSB formation over airfoil for AOA of  $6^\circ$

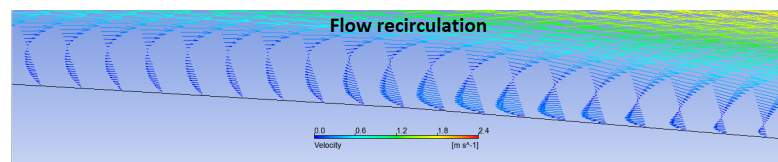
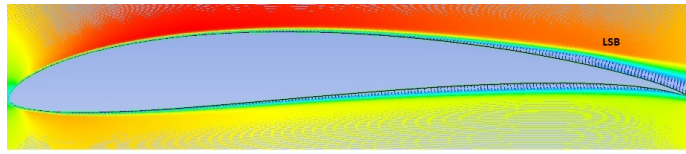


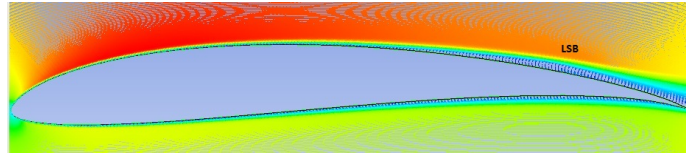
Figure 4.10: Close view of LSB showing recirculation region at AOA of  $6^\circ$  (where the reversed velocity vector direction shows recirculation and flow transition)

transition along with boundary layer flow re-energization and formation of turbulent boundary layer. Once the vector direction re-gains the streamwise direction, the flow re-attaches the surface and continue as attached flow.

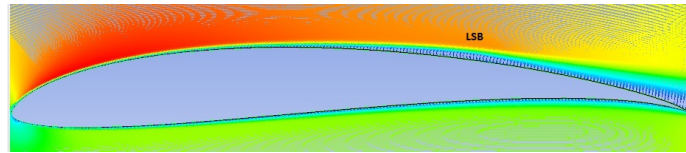
Figures 4.11a to 4.11h shows the velocity vectors near the airfoil at different AOA.



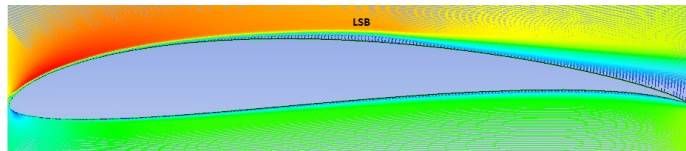
(a)  $AOA = 0^{\circ}$



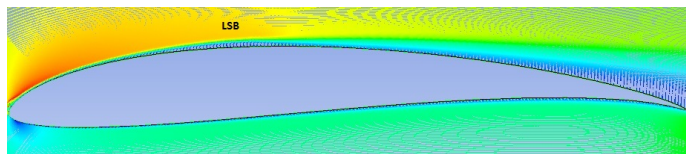
(b)  $AOA = 2^{\circ}$



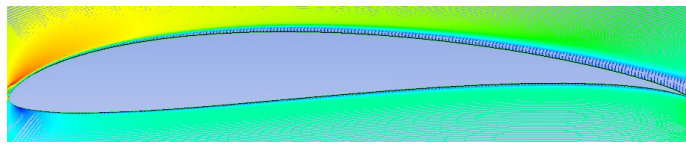
(c)  $AOA = 4^{\circ}$



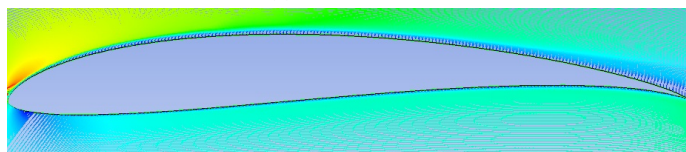
(d)  $AOA = 6^{\circ}$



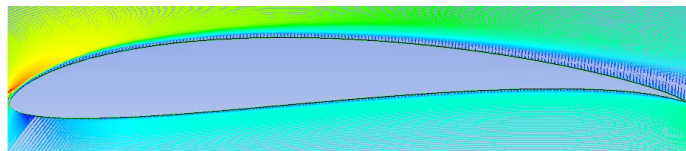
(e)  $AOA = 8^{\circ}$



(f)  $AOA = 10^{\circ}$



(g)  $AOA = 12^{\circ}$



(h)  $AOA = 14^{\circ}$

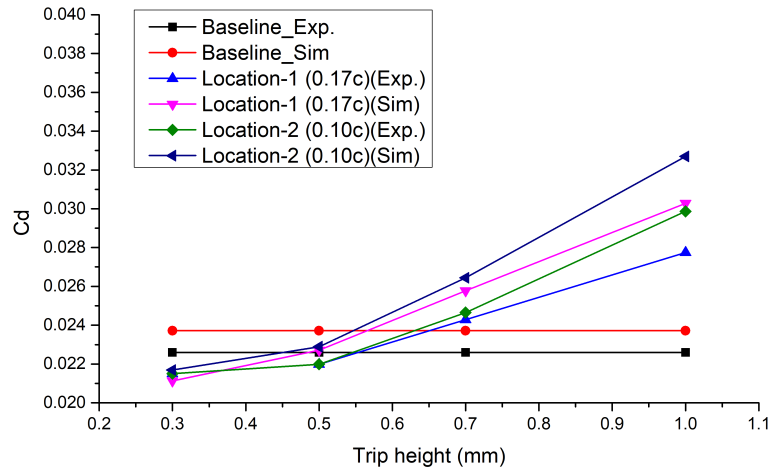
Figure 4.11: Velocity vectors over the airfoil coloured with velocity magnitude (red represents highest and blue represents lowest velocity)

The flow separation and reattachment is evident with reversed velocity vector and blue recirculation region indicates LSB formation. It can be observed that the recirculation region moves upstream with increase in AOA. There is no flow reversal beyond  $10^\circ$ . Flow separates from airfoil surface at AOA of  $12^\circ$  and complete separation occurs at  $14^\circ$ . The extent of separation and reattachment is shown in the Figures 4.9 and 4.10 for AOA  $6^\circ$  where the reversed flow represents LSB.

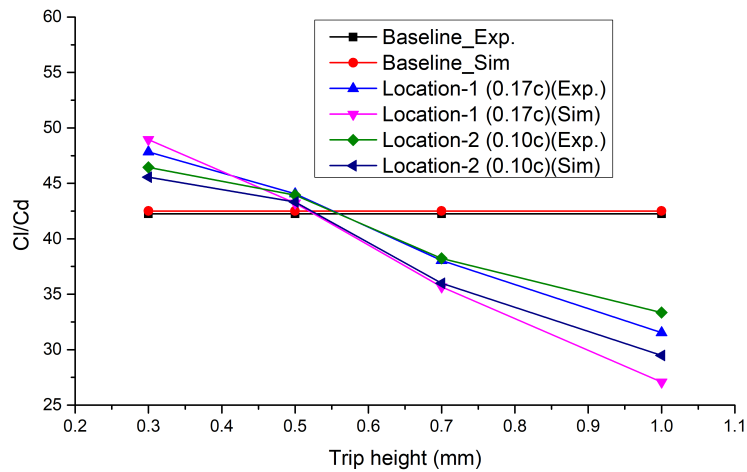
From the experimental result for  $C_p$  distribution of the airfoil at AOA of  $6^\circ$ , it is found that the LSB is formed at a distance of  $0.22c$  from the leading edge of the airfoil. Based on the result the location of BLT is chosen at two locations. For location-1 the BLT is kept at  $0.17c$  from leading edge and for location-2 it is positioned at  $0.10c$  from leading edge. The experimental study is conducted with rectangular BLT (RT) for AOAs of  $4^\circ$ ,  $6^\circ$  and  $8^\circ$ . The location is selected based on the observation that the position of LSB may move upstream or downstream depending on the AOA and meanwhile the BLT may be far upstream or very nearer to LSB which in turn resembles the situation of moving the BLT to different position or varying the Re. The affects of BLT on the total drag generation of the airfoil is the main concern. Though it affects the lift generation of the airfoil, it is not so severe and can be apparently observed from the  $C_l/C_d$  ratio. So the analysis is carried out based on the total  $C_d$  generation and  $C_l/C_d$  of the airfoil.

## **4.5 AERODYNAMIC FORCE ANALYSIS OF THE AIR-FOIL WITH RECTANGULAR TRIP**

Figures 4.12 to 4.14 show the experimental results for  $C_d$  and  $C_l/C_d$  for the airfoil with BLT for different BLT heights and AOAs along with its respective baseline results. The simulation results for the performance of baseline and modified models are plotted along with experimental results for validation purpose. The simulation results show



(a)

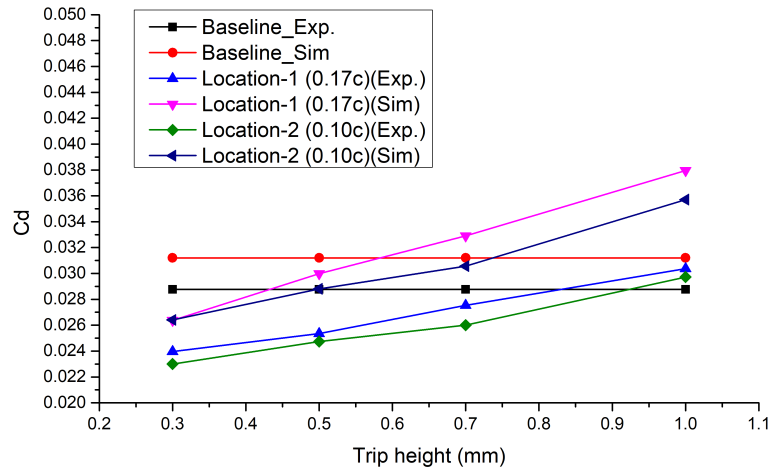


(b)

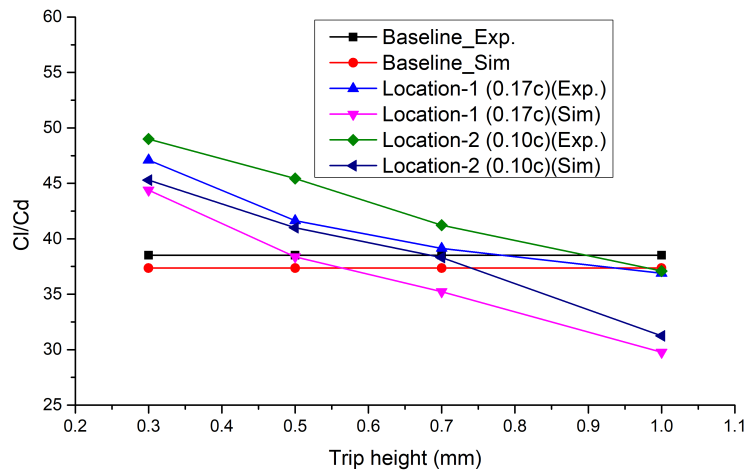
Figure 4.12: Effect of trip height and location on (a)  $C_d$  and (b)  $C_l/C_d$  of airfoil at  $AOA = 4^\circ$  ( Validation with experimental results are also shown)

good agreement with experimental results.

Figure 4.12a shows the variation of  $C_d$  with different trip heights at  $AOA$  of  $4^\circ$ . In the baseline experimental results at  $AOA$   $4^\circ$ , the LSB is observed at a distance of  $0.40c$  from leading edge. In the corresponding experiment for the airfoil with BLT, the trip is fixed at distances of  $0.17c$  and  $0.10c$  respectively for location -1 and -2 from lead-



(a)

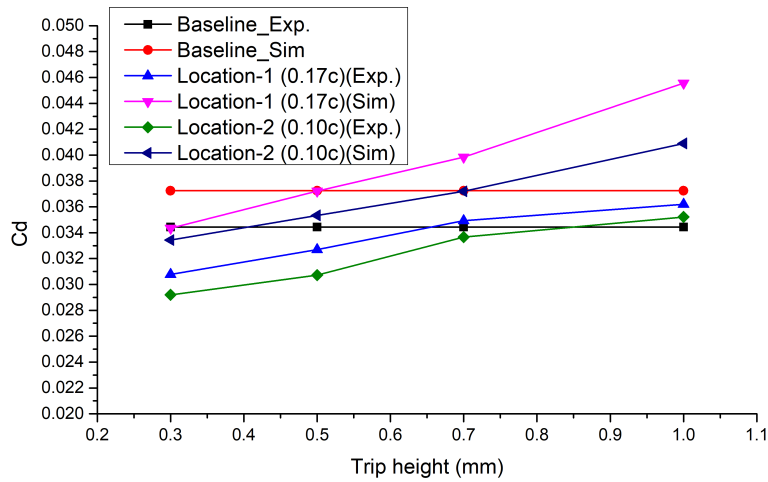


(b)

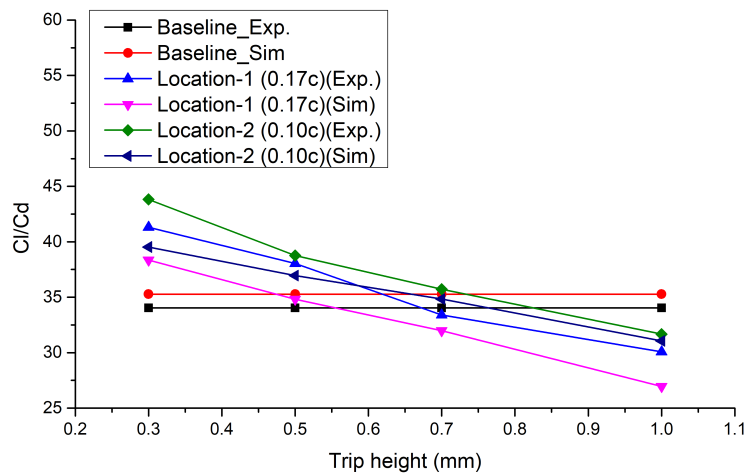
Figure 4.13: Effect of trip height and location on (a)  $C_d$  and (b)  $C_l/C_d$  of airfoil at  $AOA = 6^\circ$

ing edge. When trip is introduced on the airfoil, it converts laminar flow to turbulent. This turbulent flow remains attached to airfoil surface and it avoids/reduces LSB formation. This LSB elimination results in reduced bubble drag. Up to trip height of 0.5 mm, the reduction in bubble drag dominates the increase in frictional drag from the turbulent flow and induced device drag due to trip. Hence tripped airfoil shows better performance up to trip height of 0.5 mm compared to baseline. Thereafter the induced





(a)



(b)

Figure 4.14: Effect of trip height and location on (a)  $C_d$  and (b)  $C_l/C_d$  of airfoil at  $AOA = 8^\circ$

device drag increases with trip height and results in nullifying the advantage obtained from reduction in bubble drag. So the total drag becomes higher than baseline airfoil for trip height more than 0.5 mm. Trip at location-2 is located far upstream compared to location-1. So the turbulent flow has to flow longer distance over the airfoil than that for location-1. The laminar flow length before trip is shorter for trip at location-2 and turbulent region is longer compared to location-1. So larger frictional drag is induced

for trip at location-2 compared to location-1. This results the  $C_d$  curve for location-1 to always remain below than that for location-2. The modified model has better  $C_l/C_d$  ratio value for both the trip locations up to trip height of 0.5 mm and is shown in Figure 4.12b. Trip at location-1 performs better than at location-2 within this limit. For higher trip heights, performance is degraded due to the higher induced device drag and it outweighs the advantage obtained from the control of LSB formation.

When the AOA is increased to  $6^\circ$ , up to trip height of 0.5 mm for location-1 and up to 0.7 mm for location-2, sum of induced device drag and skin friction drag are lesser than reduction in drag achieved by eliminating LSB (bubble drag) using the BLT and net improvement in  $C_d$  is observed as shown in Figure 4.13a . For higher trip heights induced device drag dominate over reduction in bubble drag. Trip at location-2 is far upstream from LSB than that at location-1. Hence trip at location-2 could induce sufficient turbulence than the trip at location-1 which in turn reduced bubble drag more effectively and hence produce lesser total drag than that in location-1. Maximum improvement in  $C_d$  by 25.1% is observed for trip height of 0.3 mm. As the distance between the location of LSB and BLT are more, 'critical height' of trip is also increased. Effect of trip height on  $C_l/C_d$  ratio is presented in Figure 4.13b. As in the case for  $C_d$ , higher  $C_l/C_d$  up to height of 0.5 mm for location-1 and up to 0.7 mm for location-2 are observed than baseline. Maximum improvement of 21.62% is observed at trip height of 0.3 mm. For all cases, except for the case where trip height is 0.3 mm, location-2 proves advantageous over the other.

For  $8^\circ$  AOA also drag coefficients of modified airfoils are reduced significantly as shown in Figure 4.14a. For both trip locations, lower  $C_d$  is observed at 0.3 mm trip height and gradually increases with trip height due to increased device drag. The trip configurations in location-2 generated lesser drag coefficient compared to location-1. For AOA of  $8^\circ$ , location of LSB moved further upstream than that in case of AOA  $6^\circ$ .

As a result, LSB moved close to the trip location in location-1. This reduced the distance between trip and LSB which results in partial submerge of trip in LSB. In this case also LSB formation is controlled by the trip but not as effective as that in location-2 and hence generated slightly higher  $C_d$  compared to location-2. Maximum improvement in  $C_d$  value by 16.7% is observed for location-2 with trip height of 0.3 mm.

For AOA  $8^\circ$ , highest value of  $C_l/C_d$  is observed with location-2 configuration compared to location-1 and baseline results are as shown in Figure 4.14b. Highest value of  $C_l/C_d$  is obtained for 0.3 mm trip height (34.60% improvement than baseline) in location-2. For location-1 also highest  $C_l/C_d$  value is obtained for 0.3 mm trip height and the ratio is higher than baseline up to trip height of 0.65 mm. This is due to the higher rate of drag increment at higher trip heights in location-1 along with reduction in  $C_l$ .

#### **4.5.1 Coefficient of surface pressure distribution with and without boundary layer trip**

##### **Experimental result**

Pressure distribution over airfoil surface with and without BLT at AOA of  $6^\circ$  is shown in Figure 4.15. From the figure it is observed that, pressure distribution on the upper surface of the airfoil with trip is smooth which indicates the elimination of LSB. So it is a clear evidence to justify that the reduction in drag with trip is due to control of LSB.

Simulations results are used further to clearly understand the surface pressure distribution on the airfoils (baseline and modified) and flow pattern around it. The results are usefull in understanding how BLT alter the flow structure and pressure distribution

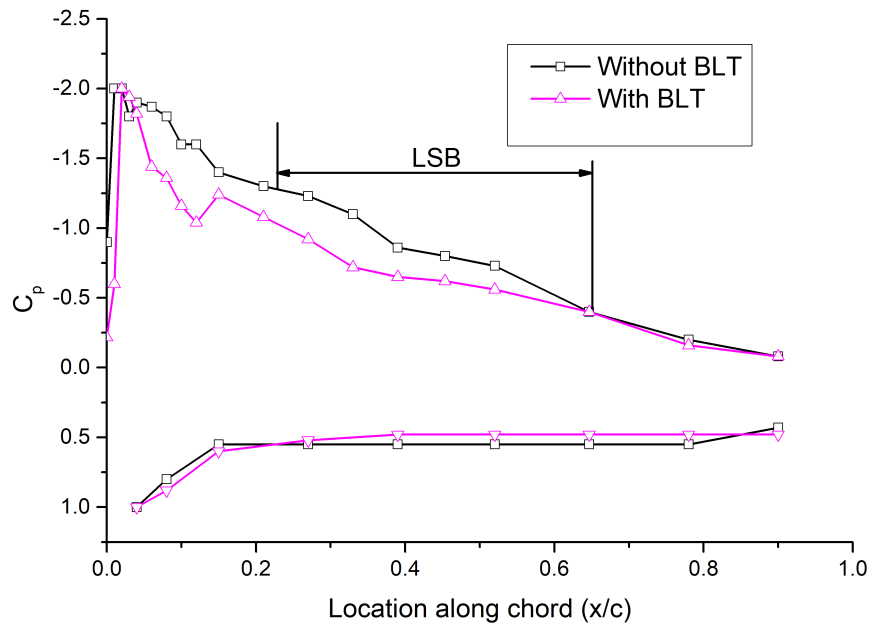
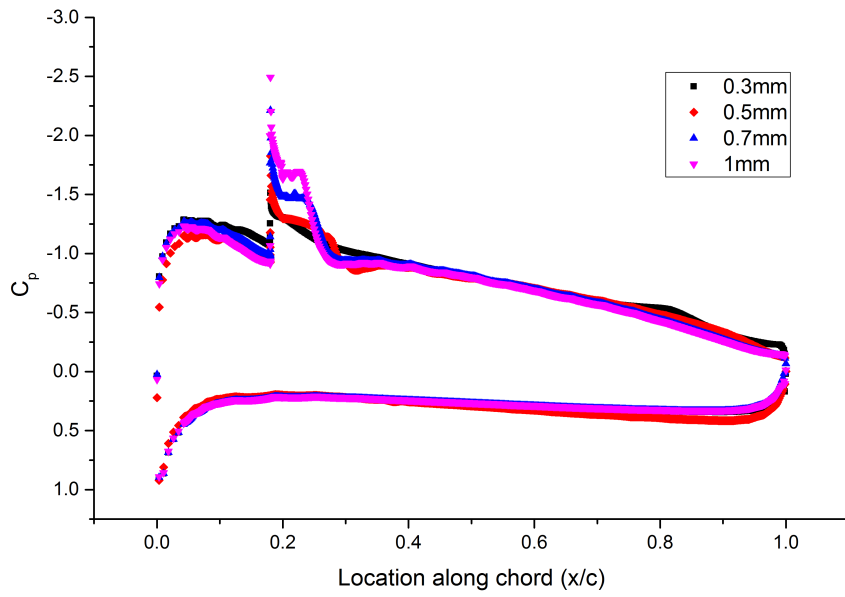


Figure 4.15: Comparison of  $C_p$  with and without trip at location-1 for AOA of  $6^\circ$

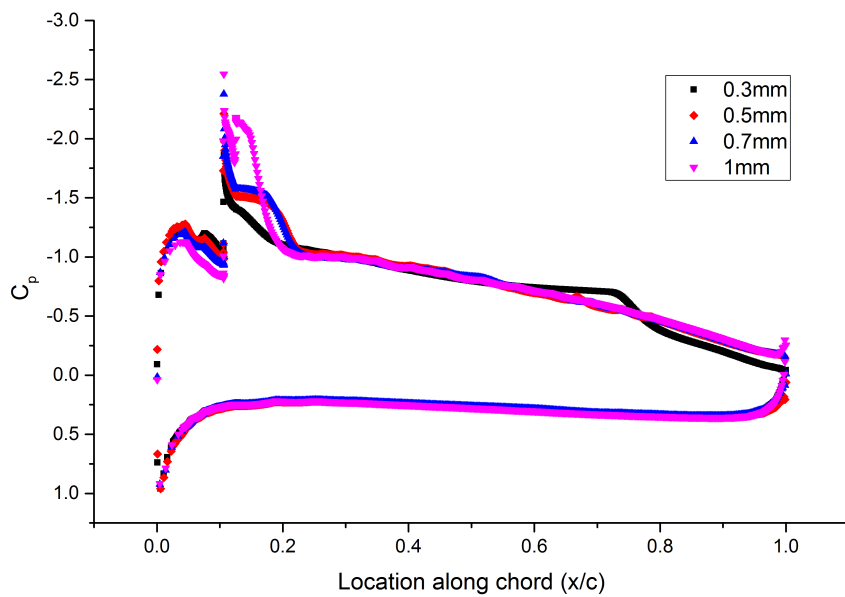
around the airfoil and the related mechanism which alter the airfoil performance.

### Simulation result

The  $C_p$  distribution around airfoil for AOA of  $4^\circ$  with trip at location-1 and 2 are shown in Figures 4.16a & 4.16b respectively. The sudden jump in  $C_p$  on suction side near to the trip is due to the flow obstruction caused by the trip, making the flow to accelerate over the trip thus creating a peak in the  $C_p$  distribution. Flow decelerates just after the trip and pressure distribution follows normal trend. The pressure distribution is smooth there after upto the trailing edge, indicating elimination of LSB except for trip height 0.3 mm in both the locations. In case of 0.3 mm trip height at both the locations-1 & 2, the turbulence induced by the trip is insufficient to fully eliminate LSB formation and hence a weak pressure plateau region can be observed in the  $C_p$  plot compared to baseline. The  $C_p$  distribution over the airfoil surface with BLT at AOA  $6^\circ$  is shown in Figures 4.17a & 4.17b. Location of LSB on base airfoil is at 0.31c from leading



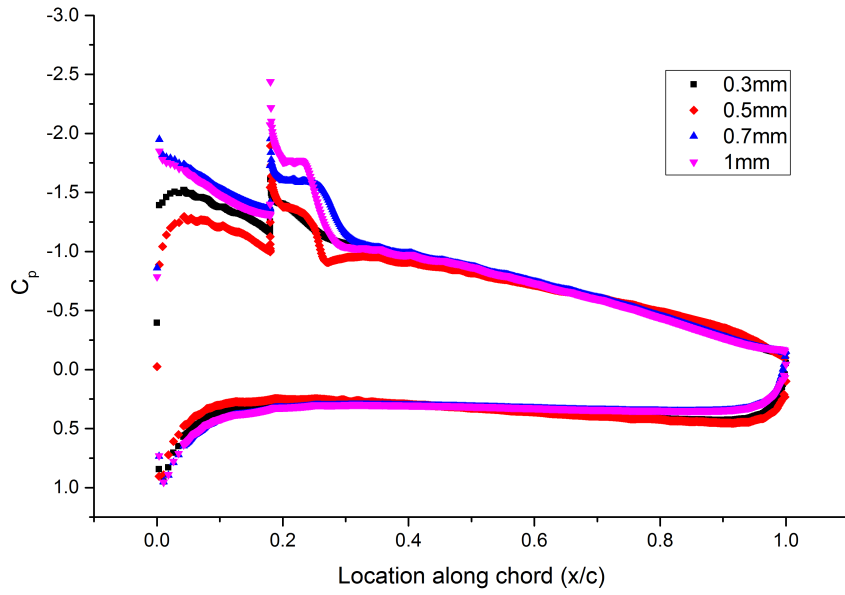
(a)



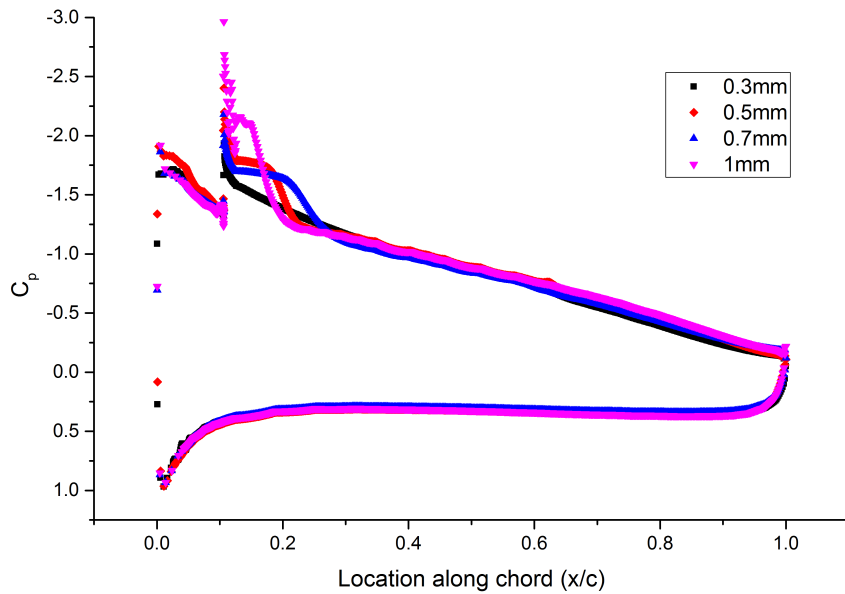
(b)

Figure 4.16:  $C_p$  distribution on the airfoil surface for AOA of  $4^\circ$ : (a) trip at location-1 and (b) trip at location-2

edge (Figure 4.5). The figures show that  $C_p$  distribution on suction surface with trip is smooth except near the trip, which indicates that the trip successfully transitioned laminar flow to turbulent with sufficient turbulence. It is clear from the graph that trip elimi-



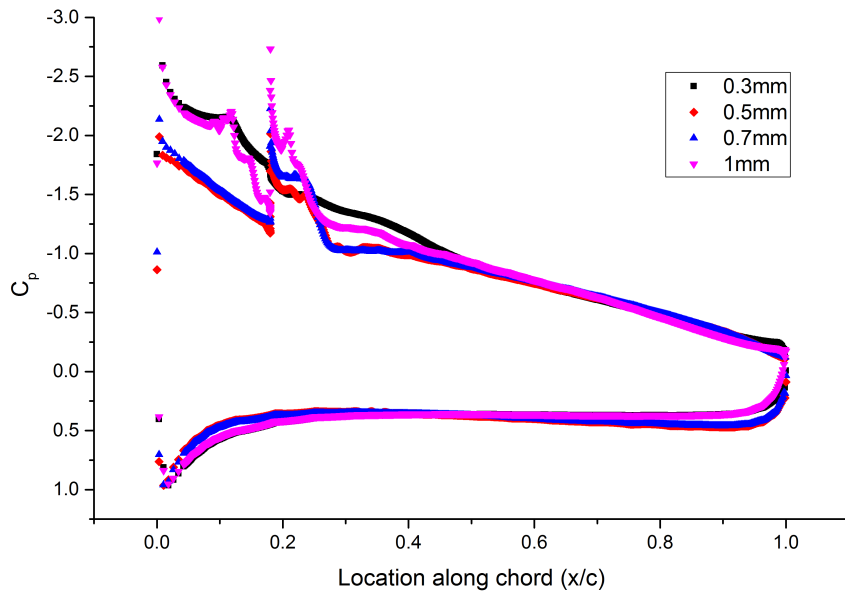
(a)



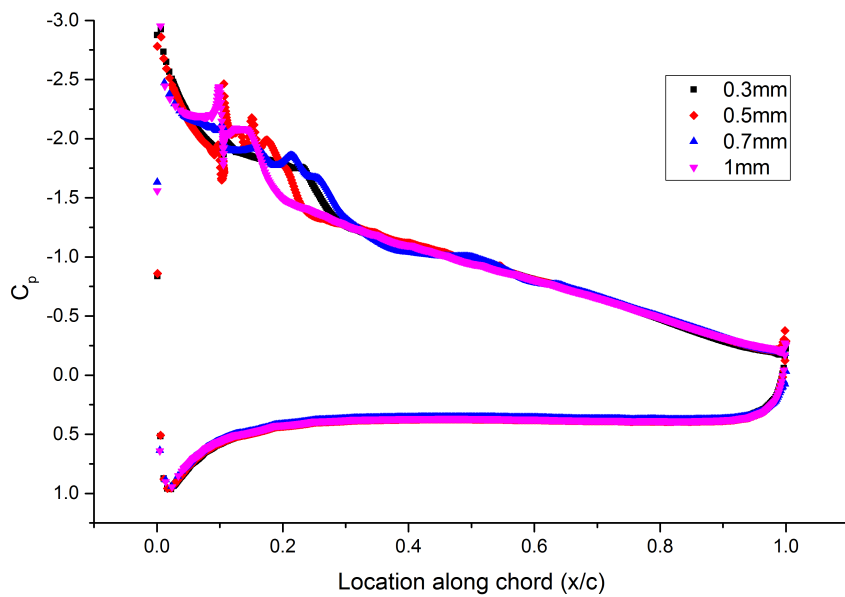
(b)

Figure 4.17:  $C_p$  distribution on the airfoil surface for AOA of  $6^\circ$ : (a) trip at location-1 and (b) trip at location-2

nates LSB for all the trip heights and trip locations by successfully transiting laminar flow to turbulent. The LSB is observed at distance of  $0.20c$  from leading edge in the numerical analysis for the base airfoil for AOA of  $8^\circ$ . Trip in location-1 is very near to



(a)



(b)

Figure 4.18:  $C_p$  distribution on the airfoil surface for AOA of  $8^\circ$ : (a) trip at location-1 and (b) trip at location-2

LSB. But still it eliminates LSB for all the trip heights (Figure 4.18a).  $C_p$  distribution over suction surface with trip at location-2 is also smooth as in the previous cases and it does not show any traces of LSB (Figure 4.18b).

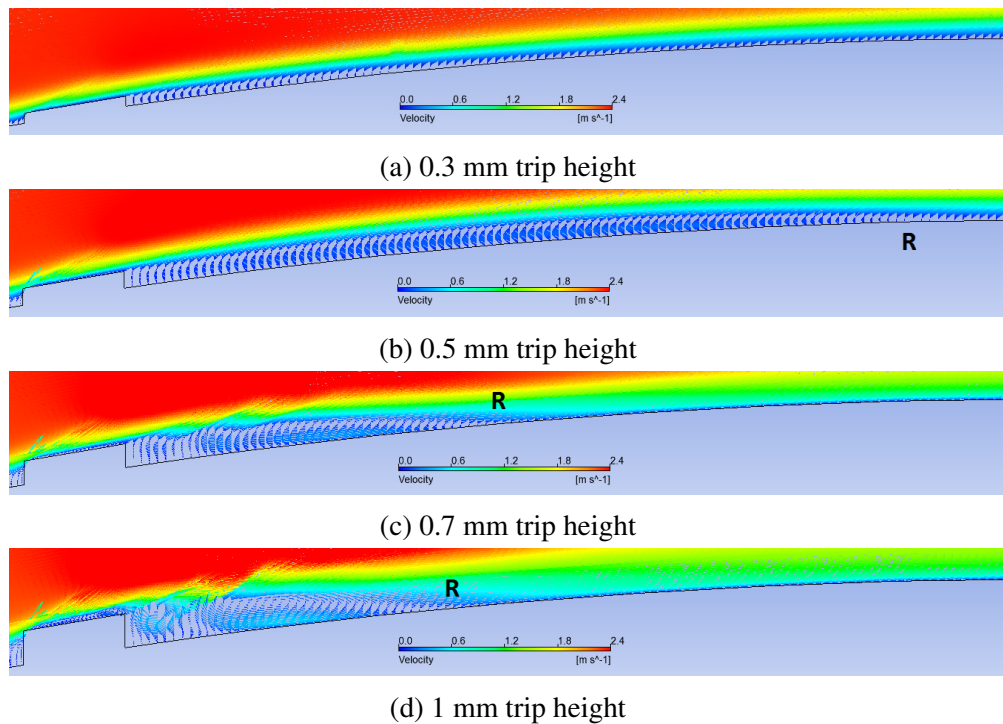


Figure 4.19: Velocity vector plot over the airfoil at AOA  $4^{\circ}$  and different trip heights for location-1 (R represents reattachment location)

Figures 4.19 & 4.20 show the velocity vector plots for airfoil with BLT for AOA of  $4^{\circ}$ . From the vector plot, it is clear that the BLT significantly alters the flow pattern and velocity distribution over the airfoil. The velocity vector directions gives the separation and reattachment point locations. The flow is from right side to left side. As explained previously, reversed velocity vector represents the flow separation. Just behind the BLT, the velocity vectors are reversed indicates separated flow. after a certain length the reversed velocity vectors turns and align to flow direction and is the point of reattachment (represented by R). This is due to the induces turbulence in the boundary layer over the airfoil and re-energize the boundary layer. This induced turbulence varies with BLT height. More the BLT height, more the induced turbulence and hence shorter the re-attachment length. For all trip heights, except for the 0.3 mm, the velocity vectors remain attached to the airfoil surface after passing over the trip and there is no sign of LSB formation. In the re-circulation region, region with reversed velocity vector, the



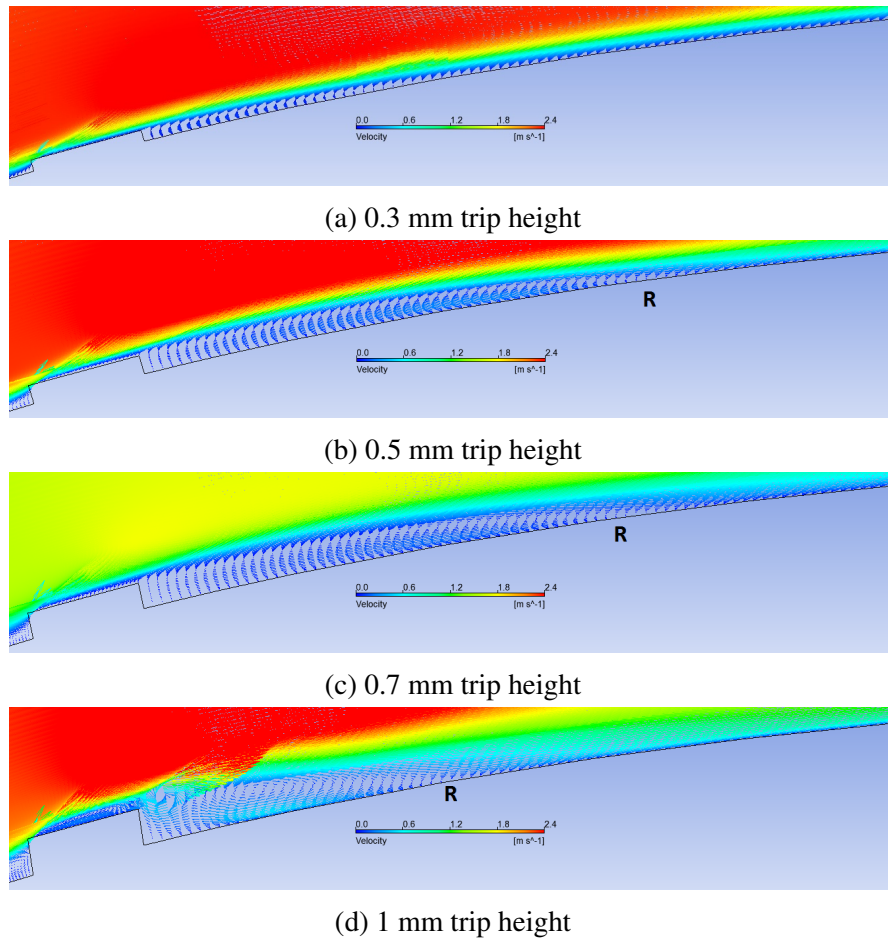


Figure 4.20: Velocity vector plot over the airfoil at AOA  $4^0$  and different trip heights for location-2 (R represents reattachment location)

transition of boundary layer from laminar to turbulent occurs. This transition length reduces as the trip height increased due to the higher strength of induced vortex. The plots show that shorter BLTs are insufficient to completely eliminate LSB. So there exist a minimum height for BLT to eliminate LSB completely. But, elimination of LSB with BLT of optimum height merely not mean that it is aerodynamically efficient. In order say the BLT performs better, its aerodynamic advantage also need to be considered.

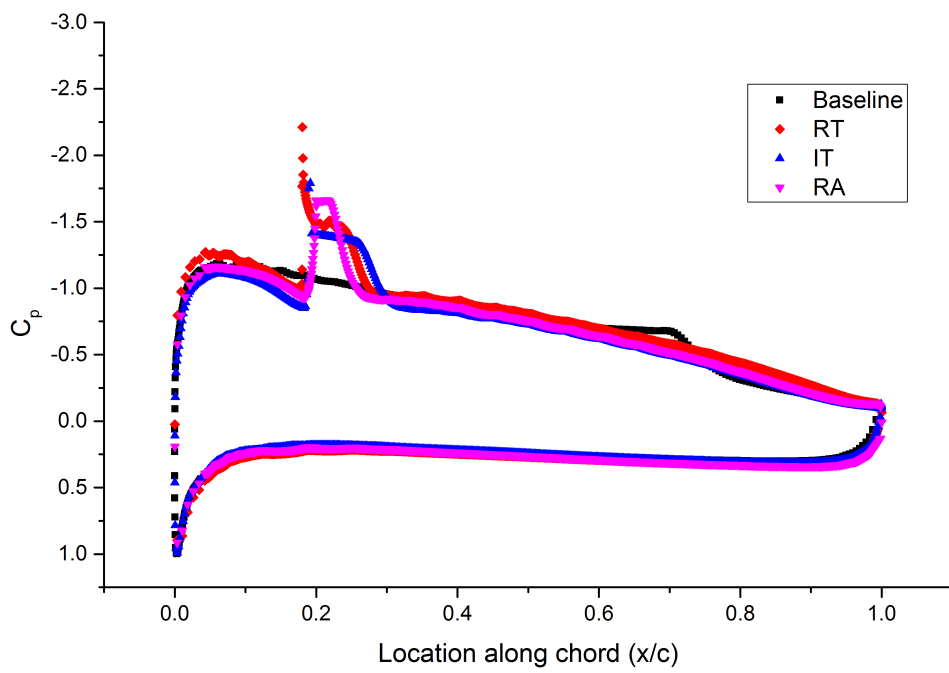
The above discussion shows that rectangular (RT) BLT is effective in reduction/elimination of LSB over the airfoil considered in the study. Net drag reduction is the sum of reduced drag from the elimination of LSB, increased device drag due to the trip

blockage and increased skin friction drag due to flow turbulence. From the velocity vector plots it is observed that there exists a recirculation region behind the BLT and a surface pressure jump in streamwise direction. This may induce detrimental effect on the aerodynamic performance of the airfoil. Further study is carried out to reduce this recirculation region and to minimise the pressure jump. To fulfil the objective an attempt is made by using BLTs of different geometrical cross-sections and is discussed in the succeeding sections.

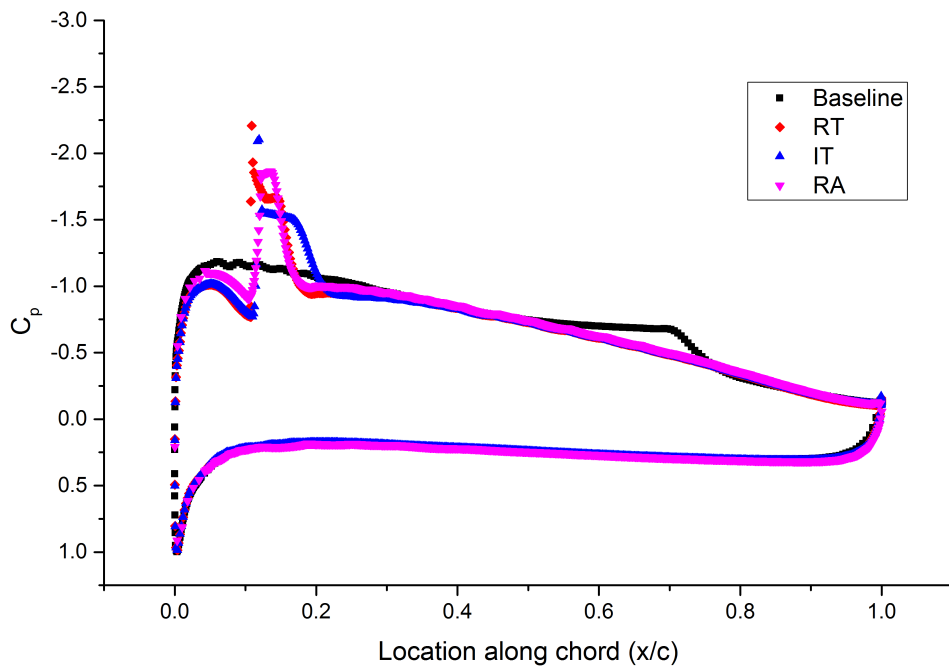
## **4.6 AIRFOIL WITH BLT OF DIFFERENT SHAPE**

### **4.6.1 Coefficient of surface pressure distribution**

The effect of different trip shape on  $C_p$  distribution is shown in Figure 4.21a and 4.21b. The pressure distribution is plotted for the trip height of 0.7 mm and AOA of  $4^\circ$ . For location-1 and location-2, LSB is completely eliminated with the trip configuration. The reattachment point of the flow for rectangular (RT) and right angled triangular (RA) trip are almost same but for the isosceles (IT), it is further down-stream from the point where flow reattached on airfoil surface for other trips. This is due to the geometrical peculiarity of the trip. Unlike other trips, IT trips have gradually declining surface after its maximum height. This surface makes the recirculating flow to attach gradually to airfoil surface resulting in an greater reattachment length. The pressure distribution of the RA trip is flatter than other kind of trips but the flow re-attaches at the same point as that of the RT trip.

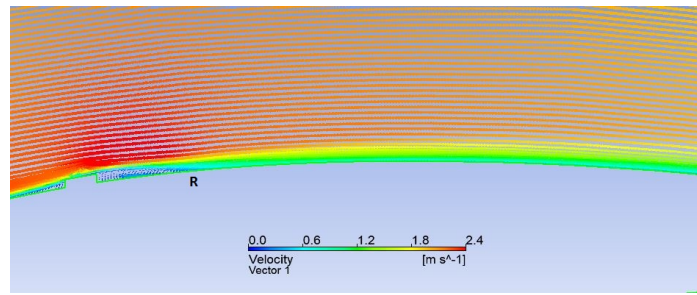


(a)

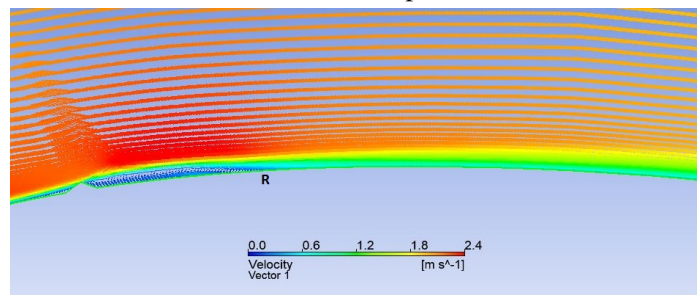


(b)

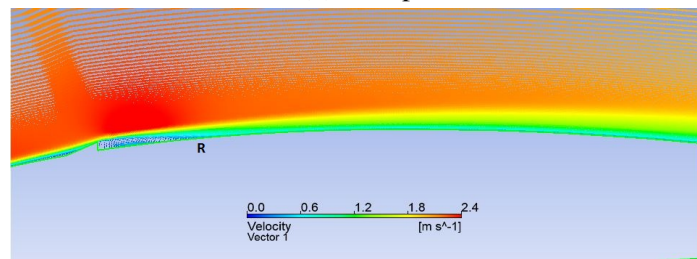
Figure 4.21:  $C_p$  distribution around airfoil for trip of different shape with height 0.7 mm for AOA of  $4^\circ$  at (a) location-1 and (b) location-2



(a) RT trip



(b) IT trip

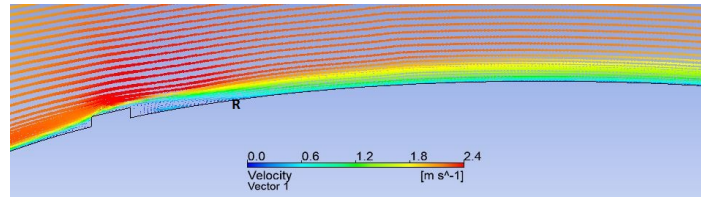


(c) RA trip

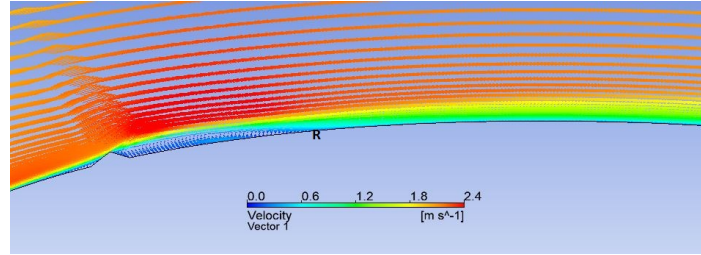
Figure 4.22: Velocity vector profile over the airfoil with trip height of 0.7 mm and different trip shapes at location-1 for AOA of  $4^\circ$  (R - flow re-attachment point)

#### 4.6.2 Velocity vector plots

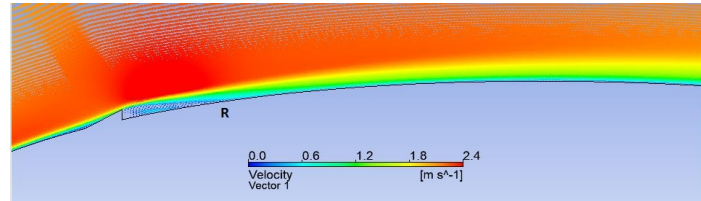
Effect of trip shape on the flow structure over the airfoil is analyzed based on the results of the trip height of 0.7 mm at AOA of  $4^\circ$  shown in Figure 4.22a and 4.23a. As observed in the respective  $C_p$  plot IT trip has longest reattachment length for the cases with the trip at location-1 and location-2. There is no spot of LSB formation indicating the complete elimination the LSB formation.



(a) RT trip



(b) IT trip



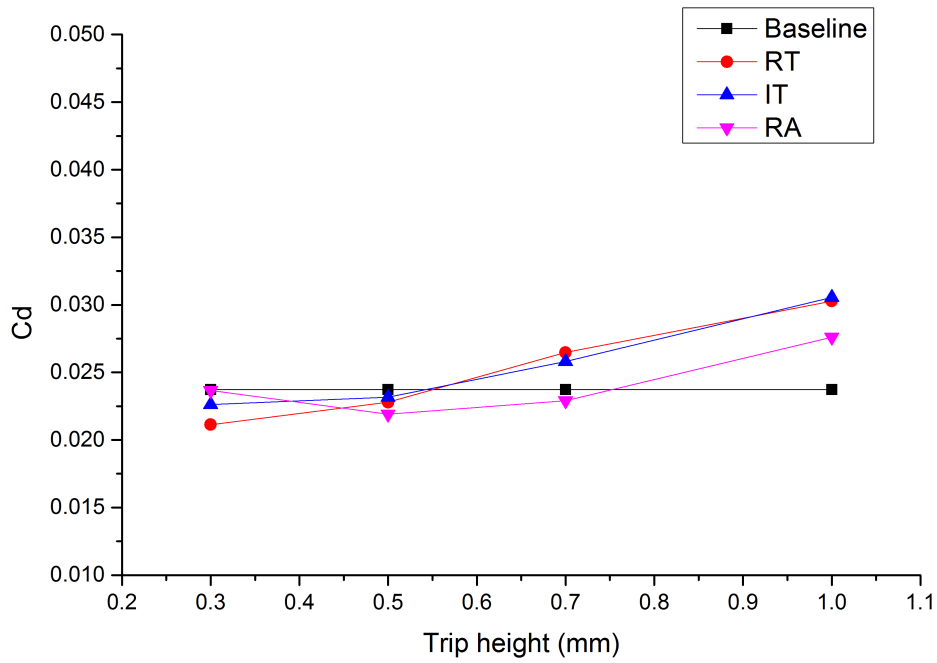
(c) RA trip

Figure 4.23: Velocity vector profile over the airfoil with trip height of 0.7 mm and different trip shapes at location-2 for AOA of  $4^0$  (R - flow re-attachment point)

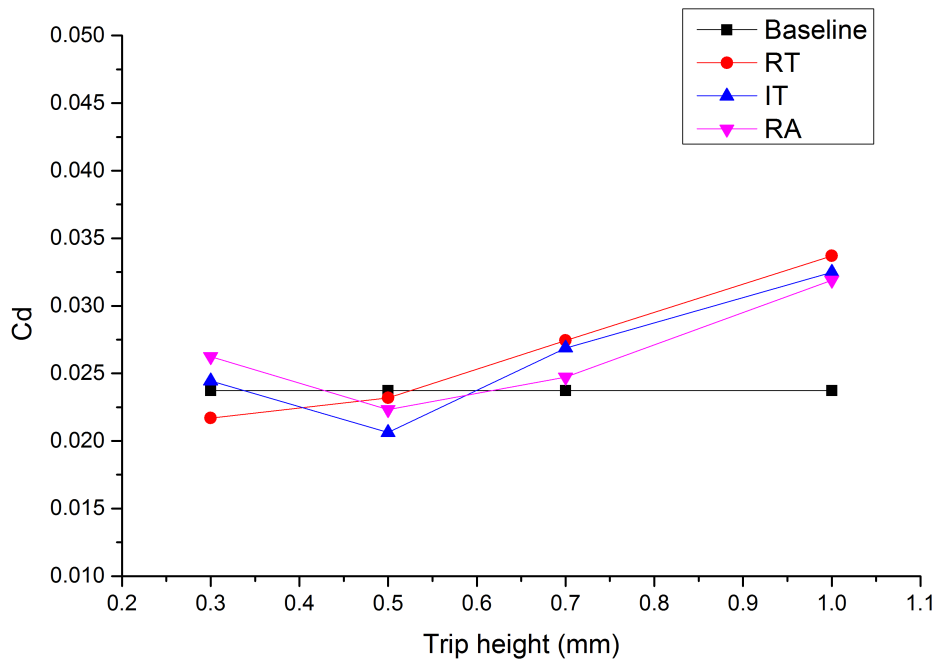
### 4.6.3 Aerodynamic performance analysis

AOA  $4^0$

The effectiveness of BLT can be examined by analyzing aerodynamic performance of the airfoil with and without BLT. Figure 4.24a shows the variation of  $C_d$  with BLT for different heights and shapes at location-1 (0.17c) for AOA of  $4^0$ . Tripped airfoils show better performance compared to baseline and the performance varies with trip heights and shapes. Different BTLs show improved performance at different trip heights. RT BLT has the maximum advantage in reduction of  $C_d$  by 8.6% at lowest trip height of 0.3 mm at location-1 compared to baseline and the performance is better than other BLTs. As the BLT height increases, the total  $C_d$  also increases and beyond BLT height of 0.5 mm, the total drag of the model becomes higher than that of the baseline. A

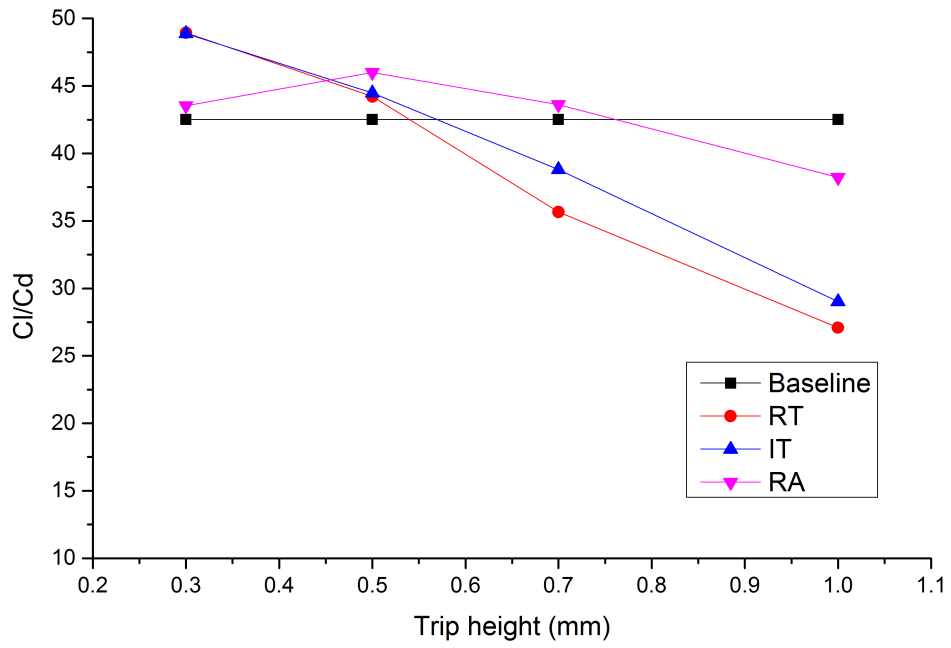


(a)

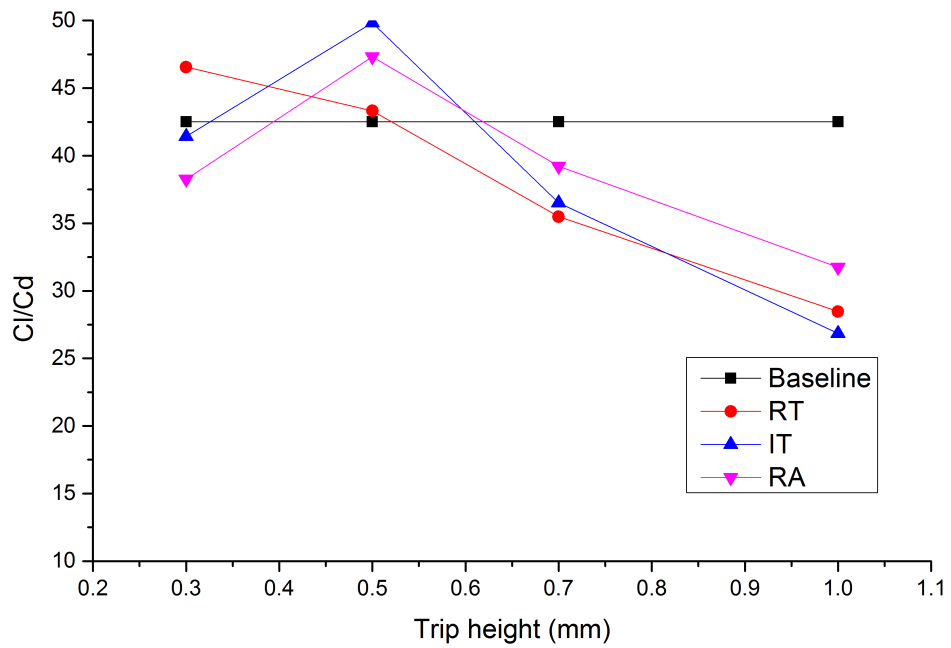


(b)

Figure 4.24: Effect of trip on  $C_d$  of airfoil at  $AOA = 4^0$  at (a) location-1 and (b) location-2



(a)



(b)

Figure 4.25: Effect of trip on  $C_l/C_d$  of airfoil at  $AOA = 4^\circ$  at (a) location-1 and (b) location-2

similar trend is observed for the IT trip, with higher drag than the RT trip but lesser than baseline till 0.5 mm height. For RA trip, initial drag is closer to baseline and as the trip height increased it produced lesser drag than baseline till the trip height of 0.7 mm. The total drag is always lower than that for other kinds of BLTs with trip height beyond 0.3 mm. BLTs are effective only if the induced device drag due to trip is less than the drag reduction achieved from limiting the LSB formation. For the RT trip with trip height 0.3 mm, the flow blockage induced by the BLT is sufficient to induce enough eddies into the flow which effectively trips the flow to turbulent and reduces the LSB formation. As the trip height increases, device drag also increases and it reaches a limiting value at 0.5 mm, beyond which the induced drag dominates the drag reduction due to the elimination of LSB. For any trip height, RT BLT produced the maximum device drag because its face is aligned normal to the flow. The drag reduced as the edge(face) which faces the incoming flow inclines towards trailing edge as in the case of IT and RA trips. Thus, the device drag reduces for IT trip and is the lowest for RA trip for same trip height. Due to the same reason at minimum BLT height of 0.3 mm, the RT trip performs best compared to other BLTs. The blockage is minimal for RA trip, hence it could produce enough drag at higher trip heights compared to other BLTs. Another important fact observed from the plot is that, the  $C_d$  value for IT BLT is closer to that for the RT trip than that for RA trip. This is due to two reasons - 1: increased device drag due to face inclination than RA trip, 2: increased frictional drag due to farther reattachment point (and longer recirculation region) of flow behind the trip due to the geometrical shape.

For all kind of trips similar performance is observed when the trip is located at location-2. For 0.3 mm trip height, both IT and RA trips produce higher drag than that of baseline. For these trips at this height, the turbulence induced is insufficient to reduce LSB. Trip at location-1 shows better performance over than at location-2. The LSB is observed at a distance of  $0.40c$  on baseline airfoil from leading edge at AOA  $4^0$ . The trip location is fixed at a distances of  $0.17c$  and  $0.10c$  respectively from leading

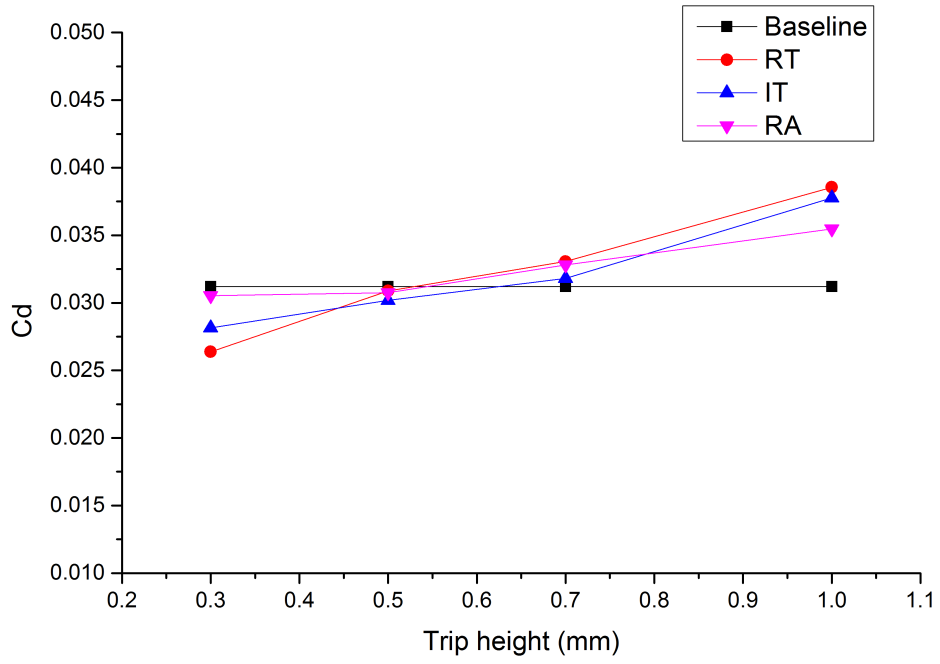


edge for location-1 and 2. When trip is present on the airfoil, the flow turns to turbulent. This high energy flow avoid LSB and tries to remain attached to airfoil surface. Trip at location-2 is far upstream compared to trip in location-1. This results in longer region of turbulent flow over the airfoil than that in location-1. Hence for the trip at the location-2, the laminar flow region prior to the trip is shorter and turbulent region is longer compared to location-1. So larger frictional drag is induced for the trip at location-2 compared to location-1.

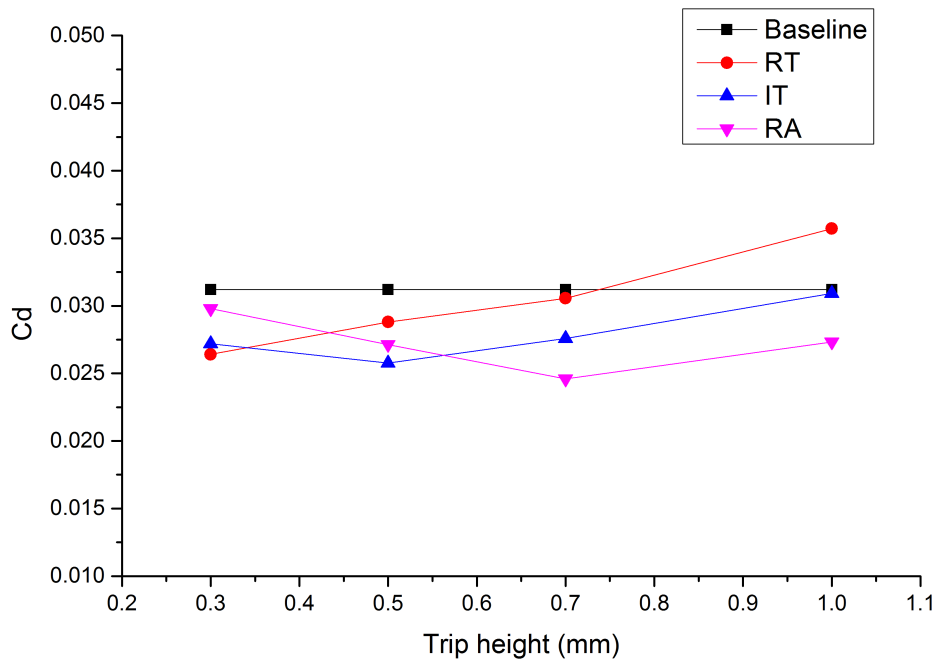
Airfoil models with BLT at location-1 have better  $C_l/C_d$  ratio value for both RT trip and IT trip up to trip height of 0.5 mm and up to 0.7 mm for RA trip as shown in Figure 4.25a. For higher trip heights, performance degraded due to the higher total drag of the models when compared to baseline. The model with RA trip has a high drag at 0.3 mm trip height and is reflected in the low value of  $C_l/C_d$ . Also, the extended reattachment region with the IT trip at higher trip height also affects the lift coefficient, resulting in value of  $C_l/C_d$  close to that for RT BLT. When the trip is located at 0.10c, the RT trip has the highest  $C_l/C_d$  ratio value of 47.56, which is higher than the baseline by 11.9%, but for other kind of trips, the value is lesser than baseline. But for the trip height of 0.5 mm, IT and RA trips have higher  $C_l/C_d$  ratio than baseline and RT trip. Beyond 0.5 mm height, all trips have lower  $C_l/C_d$  ratio than baseline.

### **AOA $6^0$**

The  $C_d$  of the airfoil with BLT at  $6^0$  AOA, for location-1, is shown in Figure 4.26a. Up to trip height of 0.5 mm for location-1, all BLTs produced lower drag than baseline. The RT trip generates the least drag for the trip height of 0.3 mm, whereas, as the trip height increases, drag with RA trip becomes lesser than other kind of trips. For the models with trip located at 0.10c (location-2), RT trip performs better than baseline till 0.7 mm trip height. At the same time, models with other trip shapes perform better than base-

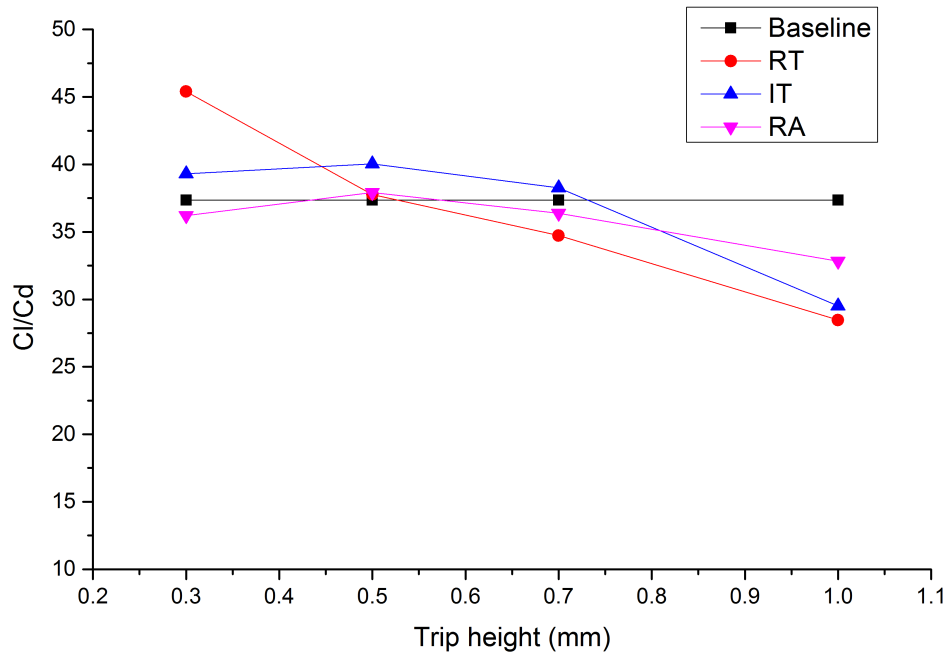


(a)

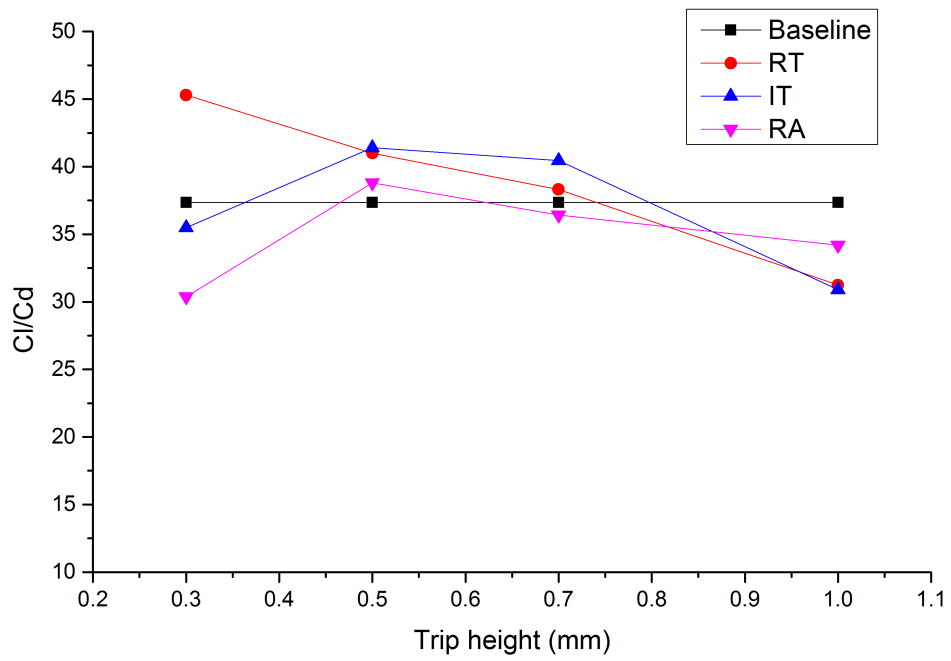


(b)

Figure 4.26: Effect of trip on  $C_d$  of airfoil at  $AOA = 6^\circ$  at (a) location-1 and (b) location-2



(a)



(b)

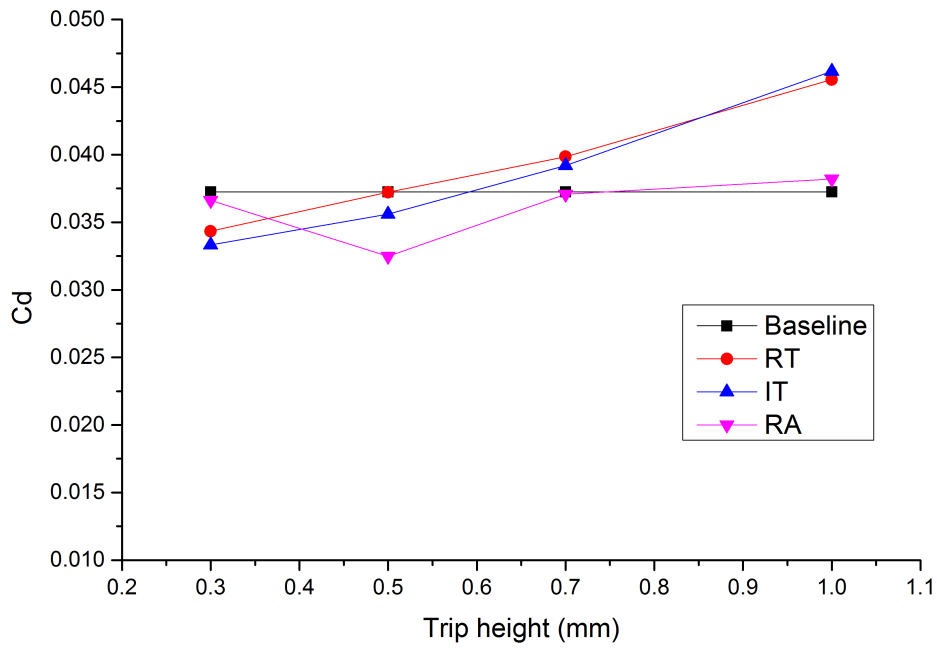
Figure 4.27: Effect of trip on  $C_l/C_d$  of airfoil at  $AOA = 6^\circ$  at (a) location-1 and (b) location-2

line for all the trip heights studied. The RA trip has superior performance over other models beyond the trip height of 0.7 mm due to its low resistance to flow. Reduction in net drag for the modified models results from the reduction of bubble drag which outweighs the induced device drag due to trips. As depicted previously, extended flow reattachment length of IT trip than other trips results in long recirculation region and increase in the total drag of the model. This makes the total drag value of the model to come nearer to that for the RT trip. Trip at location-2 is far upstream from LSB than that at location-1 (but the distance is lesser than that for AOA  $4^\circ$ ). Hence, trip at location-2 could induce sufficient turbulence than the trip at location-1 which in turn eliminates LSB more effectively and hence produces lesser total drag than that in location-1.

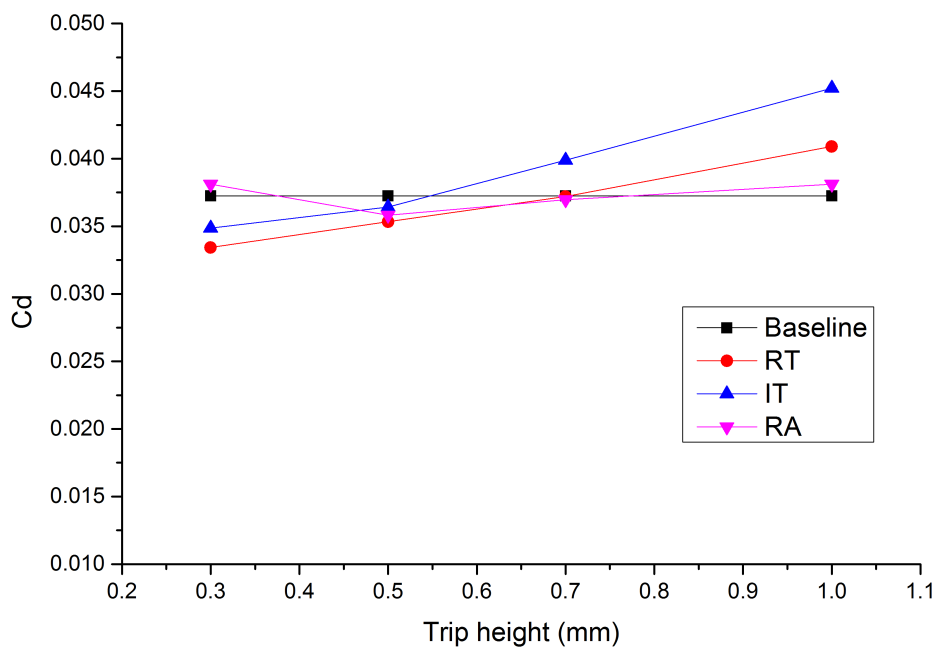
Effect of trip on  $C_l/C_d$  ratio is presented in Figures 4.27a and 4.27b. As in the case for  $C_d$ , the RT trip is effective up to height of 0.5 mm for location-1 and up to 0.7 mm for location-2. IT trip has slightly better ratio till 0.7 mm for location-1 than baseline. For the same case with the trip at location-2, the improvement is restricted between 0.5 mm to 0.7 mm trip heights. The RA trip has no advantage over baseline for any cases. Except for trip height of 0.3 mm, in all other cases, location-2 has more advantage over the other.

### **AOA $8^\circ$**

At AOA of  $8^\circ$  similar trend is observed as that in  $6^\circ$  AOA as shown in Figure 4.28a & 4.28b. As the AOA increases, LSB moves upstream and the distance between LSB and trip at locations- 1 and 2 gets reduced. This results in slight increase in drag than that at  $6^\circ$  AOA when compared to their corresponding baselines. The same reason holds good for the reduction in  $C_l/C_d$  ratio beyond the trip height of 0.7 mm, as compared to baseline and shown in Figures 4.29a and 4.29b. The IT trip has lowest  $C_l/C_d$  ratio at higher trip heights, especially for location-1. The reason behind this is the existence

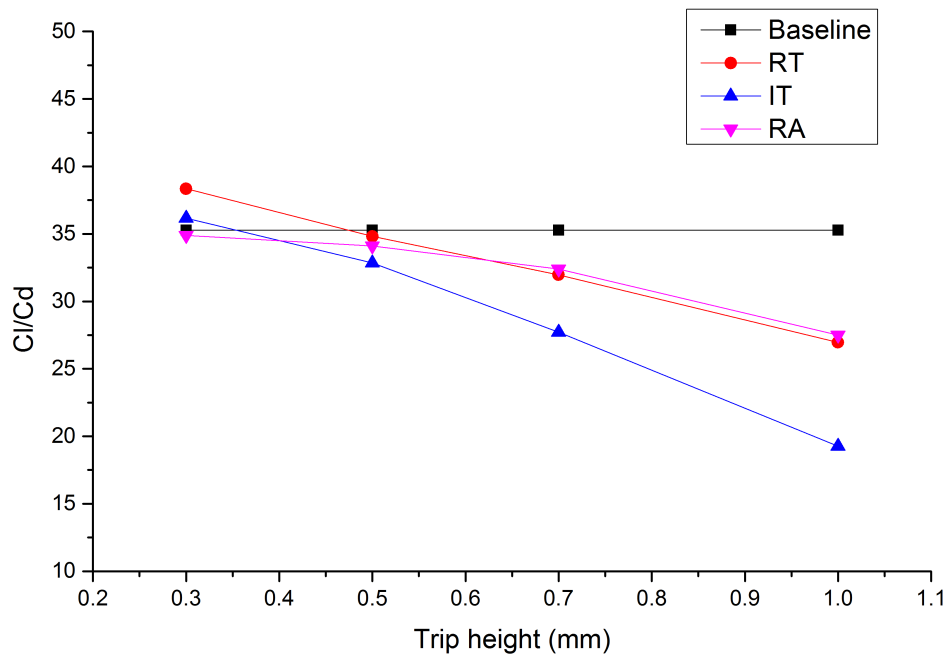


(a)

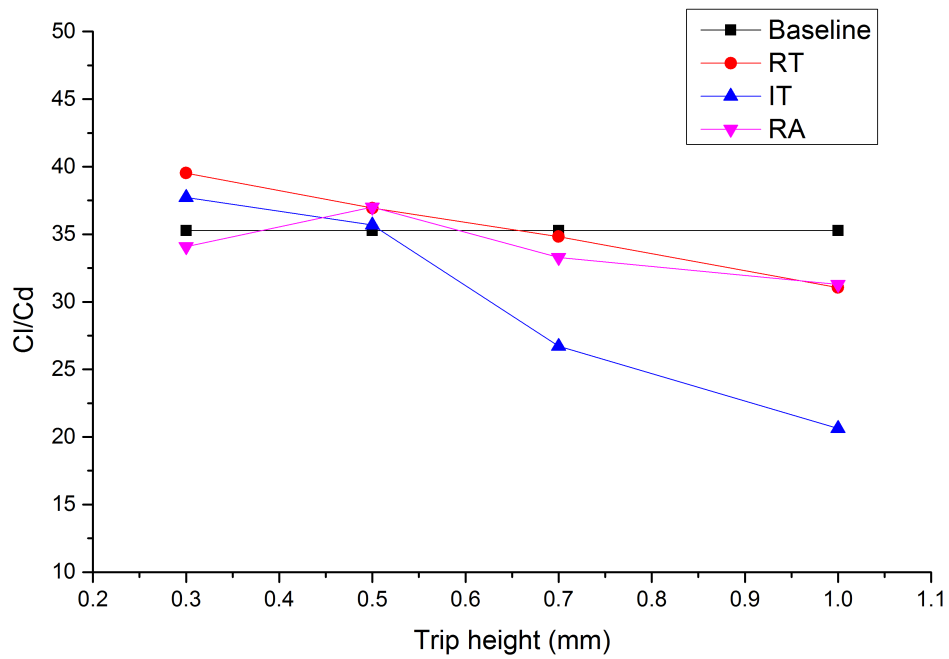


(b)

Figure 4.28: Effect of trip on  $C_d$  of airfoil at AOA =  $8^\circ$  at (a) location-1 and (b) location-2



(a)



(b)

Figure 4.29: Effect of trip on  $C_l/C_d$  of airfoil at  $AOA = 8^\circ$  at (a) location-1 and (b) location-2

of longer reattachment length of the flow. The LSB is formed very close to the trip at location-1 and the separated flow attaches to the surface after the LSB formation.

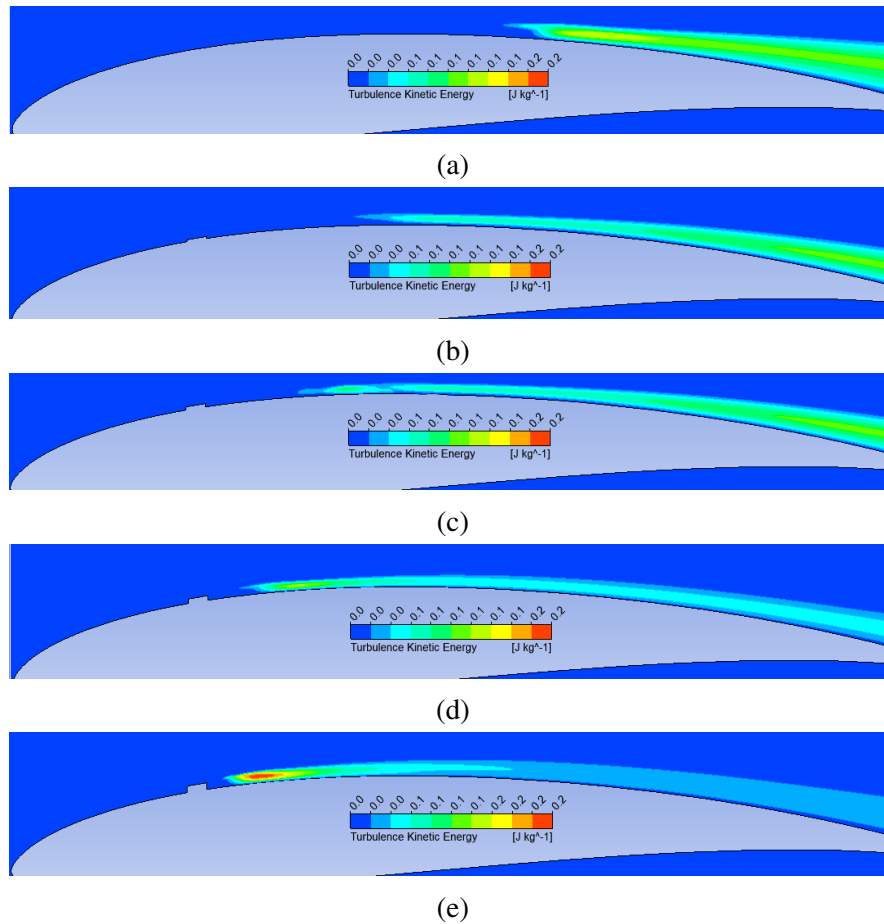


Figure 4.30: Distributions of TKE without (4.30a) and with BLT (4.30b - 4.30e) at AOA  $6^\circ$  for RT trip

Figure 4.30a shows the distributions of turbulent kinetic energy (TKE) for baseline airfoil at AOA of  $6^\circ$ . High TKE is observed at a distance of  $0.6c$  from leading edge and at this location the flow reattaches to the airfoil surface after the LSB formation. It means the flow is turbulent after the LSB. The trip induces turbulence into the flow and some flow length (transition region) is required for transition into turbulence. The region of high TKE starts where flow re-attaches to the airfoil surface after the transition. The distance between trip aft and region of high TKE reduces with increase in

trip height as shown in Figures 4.30b -4.30e where the contour is shown for the RT trip. Airfoil with the highest trip height has the lowest transition length. Higher the trip height, higher turbulence will be induced and hence shorter transitional length. From the figure, it is clear that trip energizes the flow by transiting laminar flow to turbulent and eliminates high turbulent region due to LSB formation.

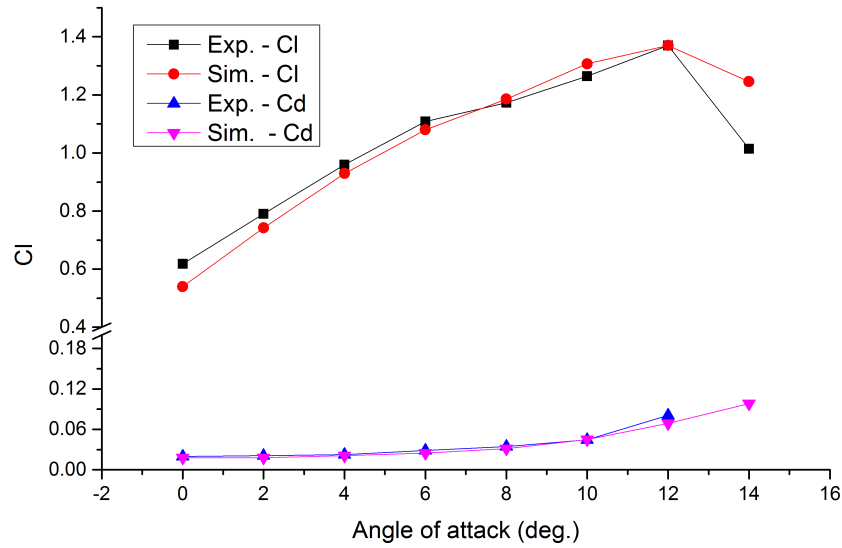
## **4.7 EFFECT OF LEADING EDGE TUBERCLES ON AERODYNAMIC PERFORMANCE OF THE AIR-FOIL**

The influence of leading edge tubercles on the aerodynamic characteristics (lift, drag, and lift to drag ratio) of E216 airfoil at Re of  $1 \times 10^5$  are discussed in this section. Nine tubercle models are numerically studied whereas three amongst them are used in experiments. The experimental results are used to validate the numerical results.

### **4.7.1 Validation of numerical simulation**

Figure 4.31a shows the variation of  $C_l$  and  $C_d$  with AOA for baseline airfoil model obtained from numerical study along with experimental result. Average deviation of 5.81% in lift and 4.31% in the drag between simulation results and experimental results are obtained and is in acceptable range. Combinations of various numerical schemes with turbulence models and grid density may be a reason for deviation of the results. Properties of the pure air are used for simulation (without moisture and salt contents) whereas in experiment the air may contain impurities, which could lead deviation in results. Reliable coincidence of values are obtained in the pre-stall region where the study is mainly focused. Compared to 2D simulation results, 3D results are in better





(a)

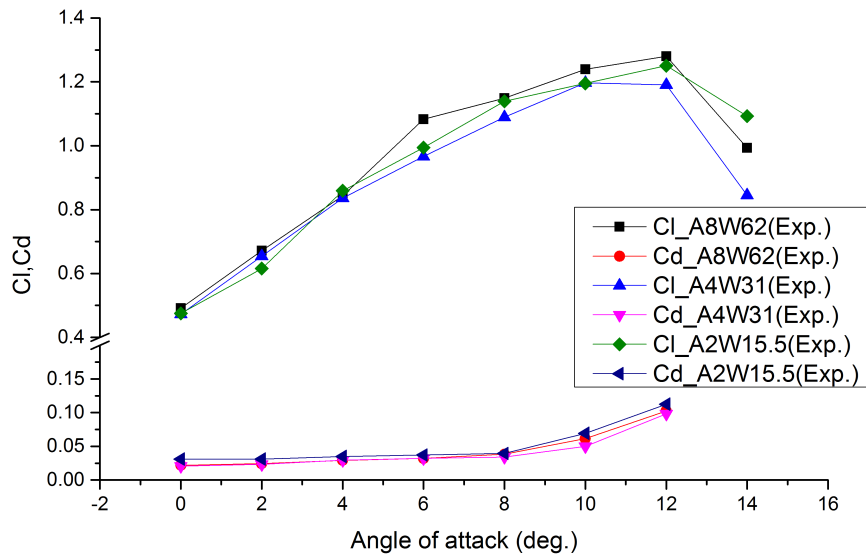
(b)

Figure 4.31: Validation of baseline 3D simulation with experimental results

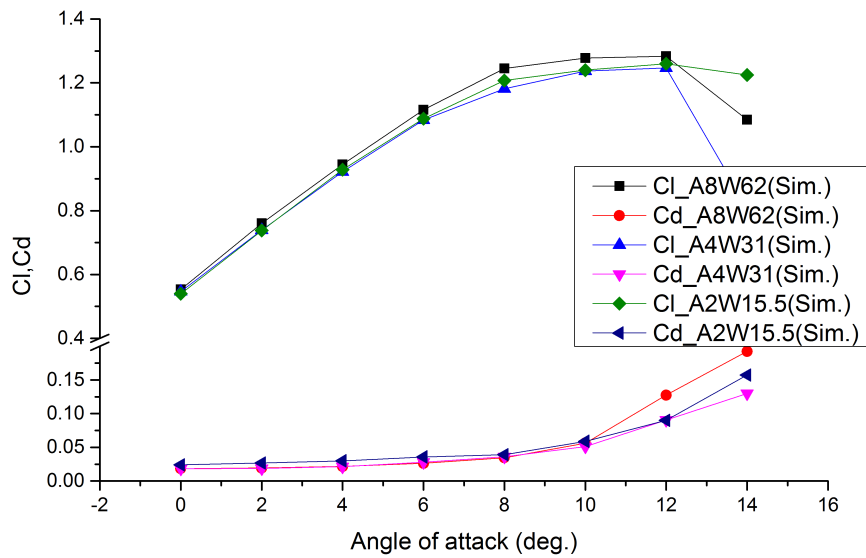
congruence with experimental results.

Stall is noticed at AOA of  $12^{\circ}$  with maximum  $C_l$  value of 1.37 (Figure 4.31a). The  $C_d$  value of 0.069 is obtained at stall angle and a drastic increment is observed thereafter. Variation of  $C_l/C_d$  with AOA compared with experimental results are shown in Figure 4.31b. Peak value of 44.39 is observed in simulation and 42.47 is observed in the experiment at AOA of  $4^{\circ}$ . Average deviation of 8.21% is observed between numerical and experimental results.

Experimental study is done on three tubercle models namely, A2W15.5, A4W31 and A8W64. The results are used to validate the simulation results as shown in Figure 4.32a and 4.32b. The simulation results are in good agreement with experimental results. The numerical study of other models are carried out after the validation and the results are presented in the succeeding subsections.



(a)



(b)

Figure 4.32: Experimental results (4.32a) and simulations (4.32b) for tubercled models

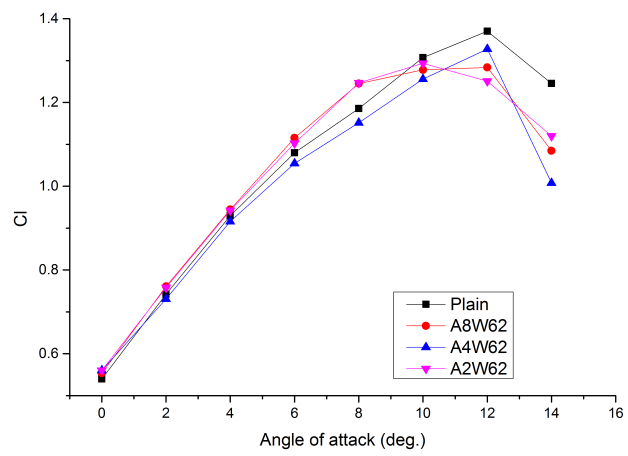
## 4.7.2 Simulation results for the airfoil with tubercle

### Effect of Amplitude

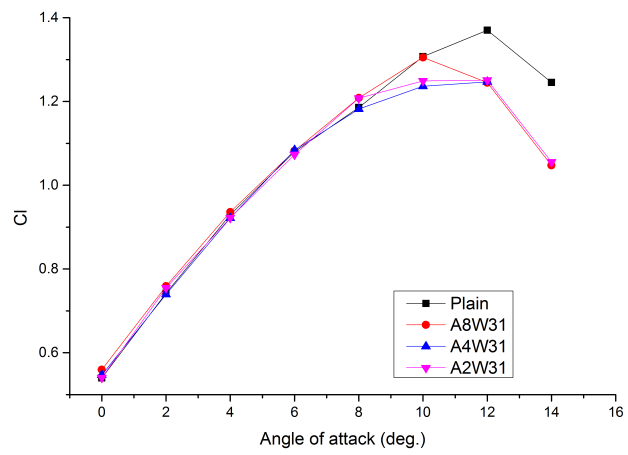
The effects of amplitude of the leading-edge protuberances (tubercles) on the performance of the airfoil is compared to that of baseline and are shown in figures 4.33a - 4.33c. The study is mainly focused in the pre-stall regime of the airfoil.

Figure 4.33a shows the effect of varying amplitude from 2 mm to 8 mm for the constant wavelength of 62 mm on the aerodynamic performance of the airfoil. All models have a similar trend in  $C_l$  variation as a function of AOA similar to that for baseline till AOA  $\approx 10^\circ$ . Baseline airfoil stalls at AOA of  $12^\circ$ . The airfoils A2W62 and A8W62 perform better than baseline in the pre-stall region. The performance enhancement is nominal at lower AOA ( $\leq 4^\circ$ ) but apparent at higher AOA ( $4^\circ \geq \alpha \leq 10^\circ$ ). Both the airfoils stall at AOA of  $10^\circ$ . The baseline airfoil has higher  $C_l$  value beyond  $10^\circ$  compared to the other two modified airfoils. The highest improvement in  $C_l$  of 5.14% is obtained for A2W62 airfoil at AOA  $\approx 8^\circ$ . Airfoil model with protuberance configuration of A4W62 has the lowest lift coefficients as shown in the plot 4.33a. Unlike other airfoils, A4W62 stalls at AOA  $\approx 12^\circ$  and generates highest  $C_{l_{max}}$  of 1.33 among the modified airfoils.

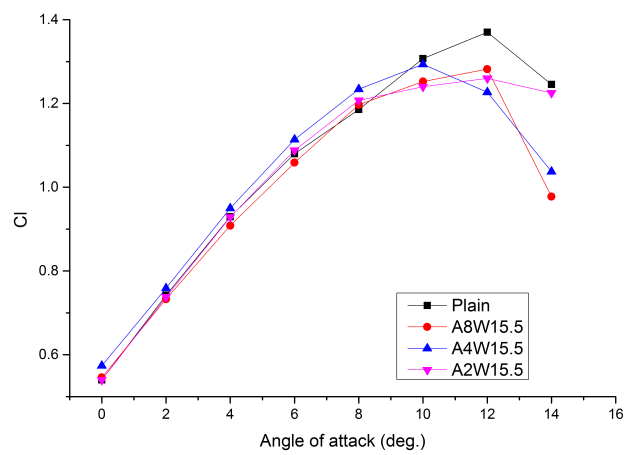
When the wavelength is 31 mm, no significant improvement in  $C_l$  values is observed and graph follows the same trend as of the baseline till AOA  $\approx 8^\circ$  as shown in Figure 4.33b. Airfoil model with the highest amplitude (A8W31) stalls at AOA  $\approx 10^\circ$  and generated  $C_l$  approximately equal to that for the baseline. Other two airfoils with tubercle configurations A2W31 and A4W31 stall at AOA  $\approx 12^\circ$  and have smooth  $C_l$  variations from  $10^\circ$  to  $12^\circ$  and produce lower  $C_{l_{max}}$  than baseline airfoil. No notable improvement in  $C_l$  is identified for the modified airfoils.



(a)



(b)



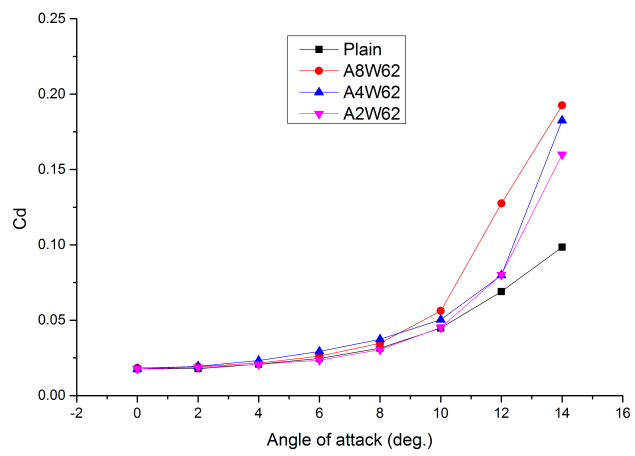
(c)

Figure 4.33: Effect of amplitude on  $C_l$  of airfoil

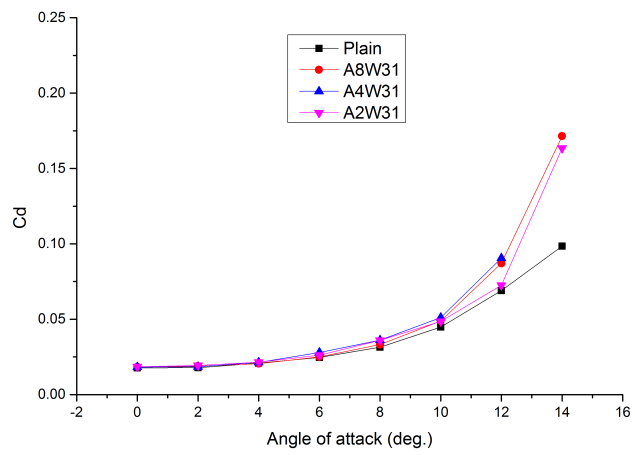
For airfoil models with wavelength 15.5 mm,  $C_l$  variation with respect to AOA followed the same trend as of the baseline till AOA  $\approx 10^\circ$  as shown in Figure 4.33c. The modified model A4W15.5 generates higher lift than all other tubercled models in the group till it stalls at an angle of  $10^\circ$ . Maximum lift improvement of 4.1% is observed at  $8^\circ$  AOA. The modified airfoils A2W15.5 and A8W15.5 stall at AOA of  $12^\circ$  which is same as that of baseline. The airfoil A2W15.5 exhibits smooth  $C_l$  variation than other models.

Figure 4.34 shows the effect of varying amplitude on  $C_d$  generated by tubercled airfoils with the protuberance and is compared with the unmodified airfoil for different AOA. The  $C_d$  generated by all modified airfoils are higher than the unmodified airfoil. No clear drag reduction is observed compared to the unmodified airfoil. The  $C_d$  of modified airfoils lies closer to the unmodified airfoil in the lower AOA range ( $\alpha \leq 6^\circ$ ) and the deviation increases with increase in AOA. Highest  $C_d$  is observed for A2W15.5 configuration.

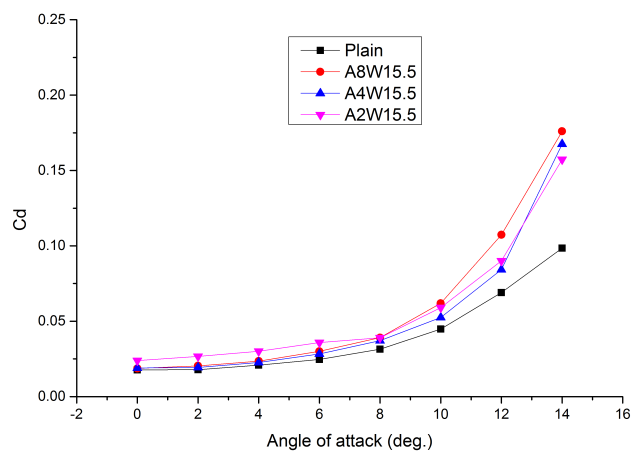
Figures 4.35 show effect of varying amplitude on  $C_l/C_d$  of the airfoil for different AOAs. The graphs represent combined effect of  $C_l$  and  $C_d$  and the ratio indicate, whether the modification is beneficial or not. Baseline airfoil has maximum  $C_l/C_d$  of 44.39 at AOA  $\approx 4^\circ$ . All modified airfoils follow the same trend as that of unmodified airfoil except A2W62. All modified airfoils show maximum  $C_l/C_d$  at AOA  $\approx 4^\circ$  except for airfoil A2W62. The airfoil A2W62 shows the maximum ratio at AOA =  $6^\circ$ . Except for the airfoils A2W62 and A8W31, no other airfoils show better performance than the unmodified airfoil. The airfoil A8W31 generates 2.78% higher  $C_l/C_d$  ratio than unmodified one at AOA of  $4^\circ$ . The model A2W62 generates highest  $C_l/C_d$  ratio of 46.91 at AOA of  $6^\circ$ . The value is 7.37% higher at the AOA of  $6^\circ$  and 5.68% higher than that at AOA of  $4^\circ$  compared to unmodified airfoil.



(a)

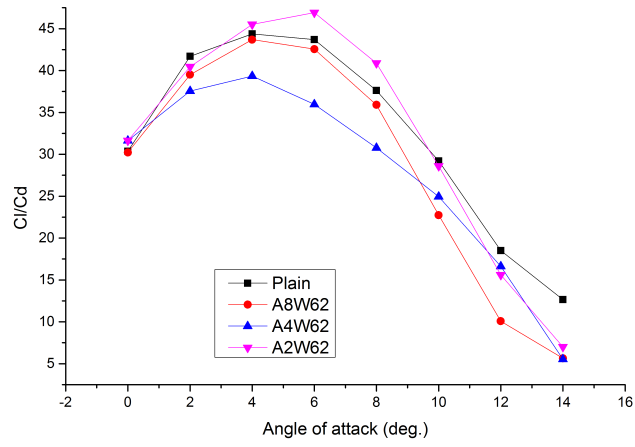


(b)

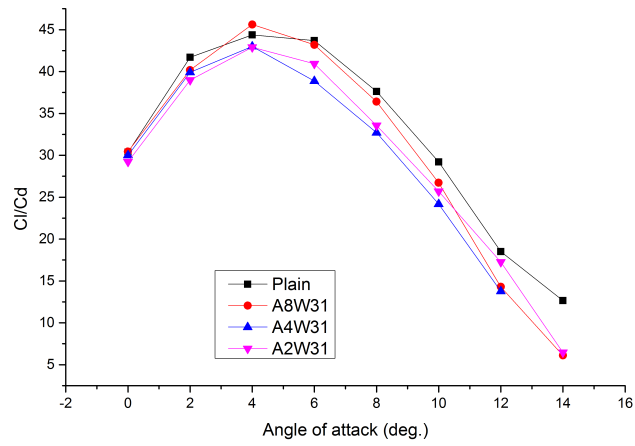


(c)

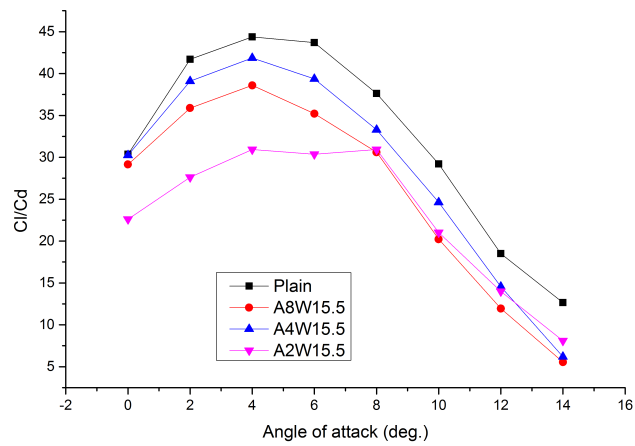
Figure 4.34: Effect of amplitude on  $C_d$  of airfoil



(a)



(b)



(c)

Figure 4.35: Effect of amplitude on  $C_l/C_d$  of airfoil

### Effect of wavelength

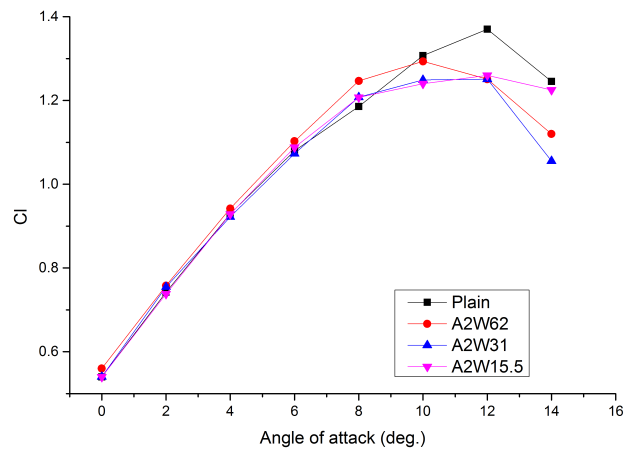
Variation of  $C_l$  with respect to AOA for different wavelength and amplitude of 2 mm is shown in Figure 4.36a. All the modified airfoils followed same  $C_l$  variation trend with respect to AOA as that for baseline airfoil. The marginal advantage of  $C_l$  value is obtained for A2W62 than baseline till stalling. The model stalls at  $10^\circ$  unlike the unmodified airfoil. Other two modified airfoils exhibit extended stall angle of  $12^\circ$ . Airfoil model A2W15.5 has smoother  $C_l$  variation at higher AOA.

When the amplitude is 4 mm, A4W31 and A4W62 airfoils stall at  $12^\circ$ , shown in Figure 4.36b. The model A4W31 shows smoother  $C_l$  variation than other models. Though A4W15.5 stalls at  $10^\circ$ , it has better  $C_l$  in the pre stall region compared to other models. When the amplitude is 8 mm, delayed stall angles are observed for models A8W15.5 and A8W62 as shown in Figure 4.36c. The model A8W62 airfoil has higher  $C_l$  value in the pre-stall region than all other airfoils, where as the model A8W15.5 has smooth  $C_l$  variation. The airfoil A8W31 has similar characteristics as that of baseline airfoil.

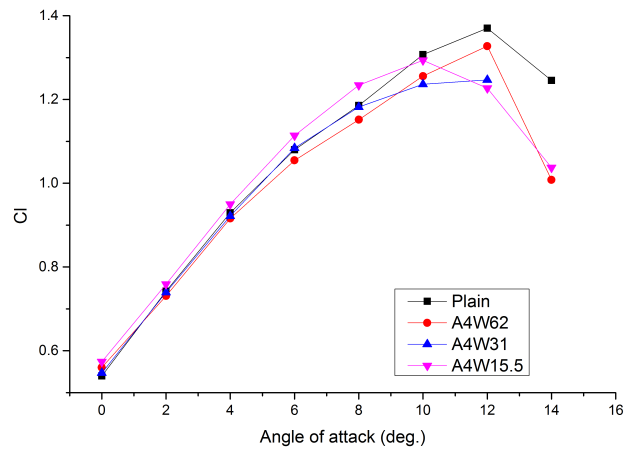
Figure 4.37 shows the effect of varying wavelength of the tubercles on  $C_d$  generated by airfoils with the protuberance and is compared with the unmodified airfoil for different AOA. As explained previously, all the tubercled airfoils have higher  $C_d$  than the unmodified airfoil. The  $C_d$  of these modified airfoils lies closer to the unmodified airfoil in the lower AOA range ( $\alpha \leq 6^\circ$ ) and the deviation increases with AOA. Highest  $C_d$  are observed for A2W15.5 configuration.

Figures 4.38 shows effect of varying wavelength on airfoil performance for different AOA. All the modified airfoils follow the same trend as that of unmodified airfoil except A2W62. All the modified airfoils have maximum  $C_l/C_d$  at AOA  $\approx 4^\circ$  except for airfoil A2W62 (for which maximum ratio occurred at AOA =  $6^\circ$ ). Only the airfoils A2W62 and A8W31 show better performance than the unmodified airfoil. The performance variation does not show any particular trend with variation of amplitude or

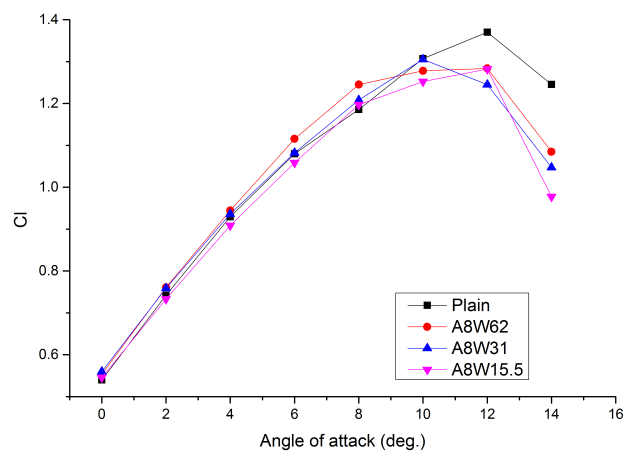




(a)

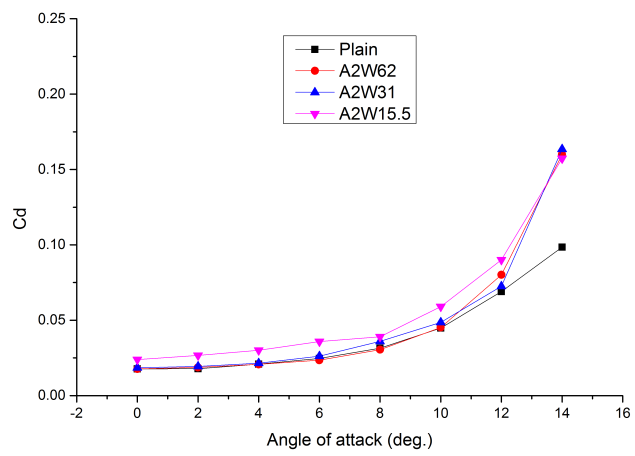


(b)

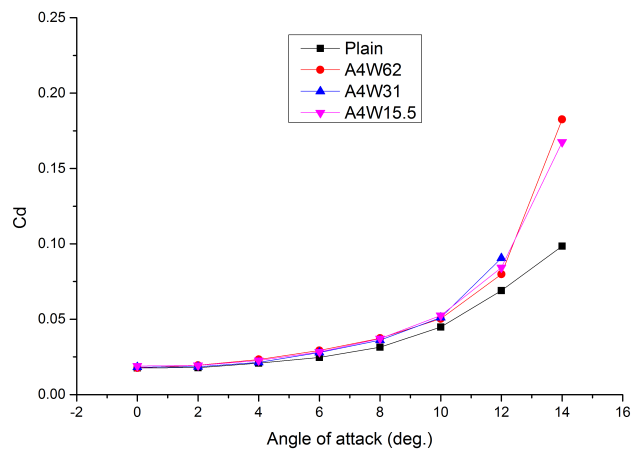


(c)

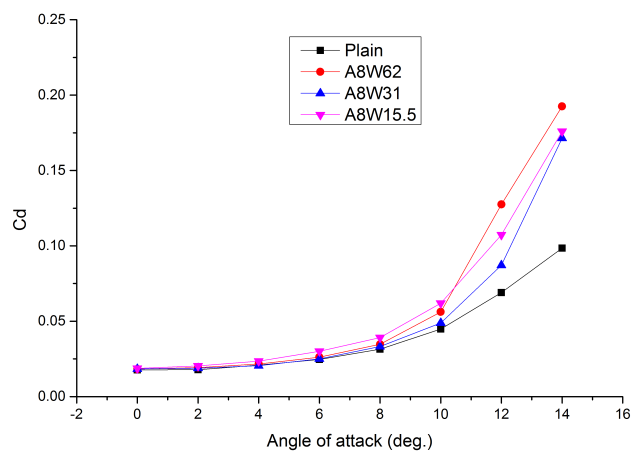
Figure 4.36: Effect of wavelength on  $C_l$  of airfoil



(a)

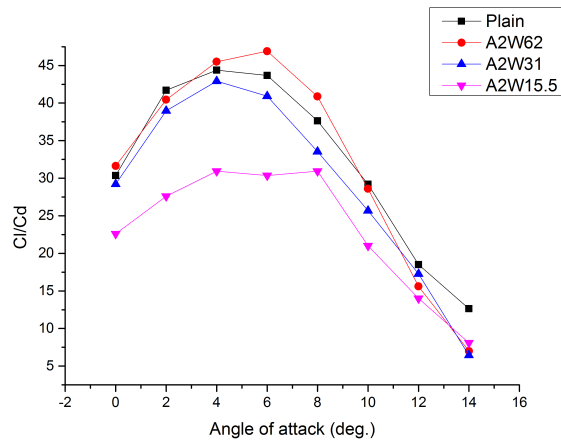


(b)

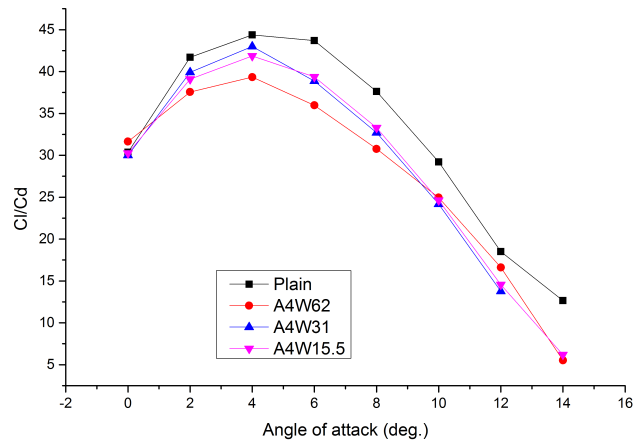


(c)

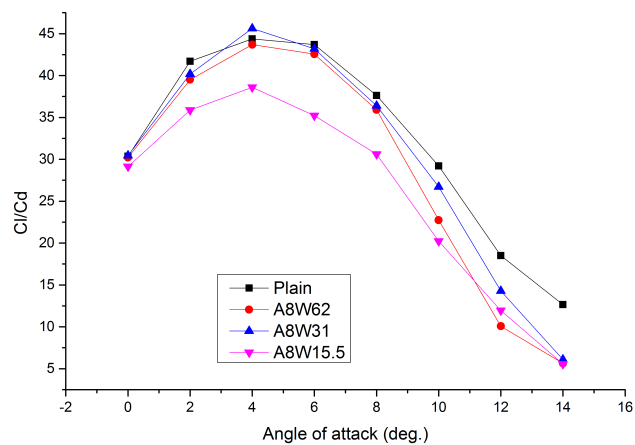
Figure 4.37: Effect of wavelength on  $C_d$  of airfoil



(a)



(b)



(c)

Figure 4.38: Effect of wavelength on  $C_l/C_d$  of airfoil

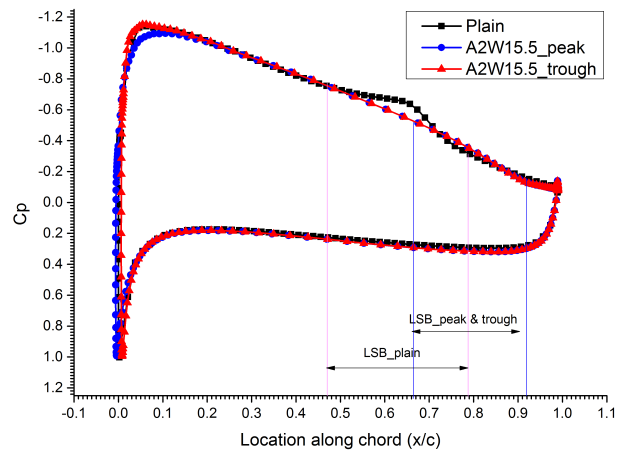
wavelength alone but it depends on the combination of amplitude and wavelength.

### 4.7.3 Distribution of coefficient of surface pressure

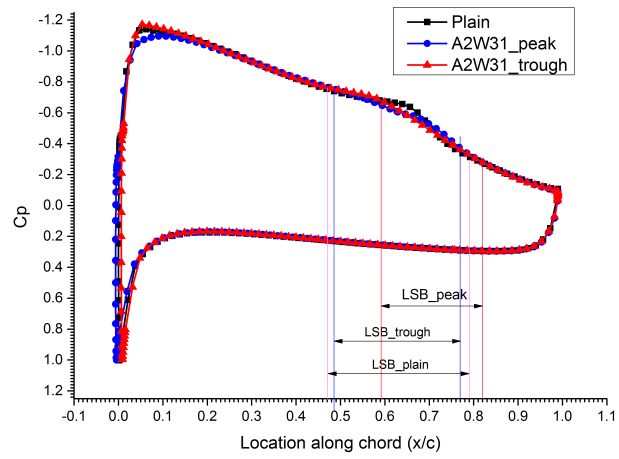
Figures 4.39 - 4.41 shows the distribution of coefficient of surface pressure on tubercled models along with baseline model at AOA of  $4^0$ . The  $C_p$  distributions are plotted with respect to  $x/c$  locations of airfoils along the steam wise direction. The  $C_p$  distribution of baseline model is plotted at midspan. The  $C_p$  distribution of modified airfoils are plotted at two different span-wise locations, one along the peak and one along the trough of the model.

The suction peak of -1.05 is observed for the baseline model near to leading edge on the upper surface as shown in figure 4.39a and the flow accelerates thereafter. Distinct pressure plateau followed by sudden variation in the value of  $C_p$  is observed on the suction surface. This surface pressure pattern is generally expected on an airfoil at low Re (Karthikeyan *et al.* 2014). Presence of pressure plateau and sudden increase in  $C_p$  value is an indication of the LSB formation. The laminar boundary layer separates at around  $x/c = 0.48$ , represented by the initiation of pressure plateau in the  $C_p$  plot, and subsequent reattachment at  $x/c = 0.79$  from leading edge of the baseline model. As shown in the figure, length of LSB is observed to be  $0.31c$  for the baseline model.

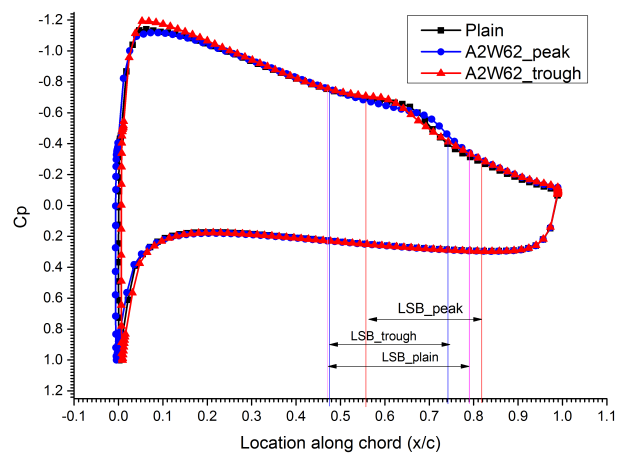
Figures 4.39a - 4.39c show the  $C_p$  distribution on modified models with varying wavelength and for constant amplitude of 2 mm, compared with unmodified model. Pressure distribution over the models have similar pattern as that of baseline. The modified models have highest suction peak along the peak and least along the trough of the tubercle on the suction surface. The vlue of the suction peak for the modified model with tubercles having the least amplitude and wavelength (A2W15.5) is same at peak



(a)



(b)



(c)

Figure 4.39:  $C_p$  distribution on modified and unmodified models at AOA of  $4^\circ$

and trough, which is equal to -1.14 and is slightly higher than that of baseline. A very weak LSB with vague pressure plateau is formed close to trailing edge compared to baseline. Location of LSB formation behind peak and trough in stream-wise direction are observed to be at identical locations. The flow starts to separate at  $0.63c$  and reattaches at  $0.92c$  resulting in bubble size of  $0.29c$ . Length of the bubble is reduced by 6.5% than the baseline model. There is no strong pressure plateau in the pressure distribution compared to unmodified model which indicates the reduction in the strength of the bubble.

When the wavelength is increased to 31 mm (A2W31), peak suction pressure of modified model becomes -1.10 and -1.18 respectively for peak and trough as shown in Figure 4.39b. The suction peak of baseline lies between these two values. In this case, stronger LSB is formed compared to A2W15.5. Unlike A2W15.5, the position of LSB formation differs behind peak and trough along the stream-wise direction. The LSB behind the trough starts at  $x/c = 0.49$  and ends at  $x/c = 0.77$  with a total length of  $0.28c$ . The position of LSB in stream-wise direction is located ahead of that for peak as well as for the baseline model. Behind the peak, LSB formation starts at around  $x/c = 0.59$  and ends at  $x/c = 0.82$  resulting in total length of  $0.23c$ . The strength of both the LSB is lesser than the baseline with an average 17.7% reduction in length for the bubble. Location shift of LSB behind trough and peak causes the formation of LSB in a wavy manner on the suction surface of the modified airfoil unlike the straight LSB on the baseline model.

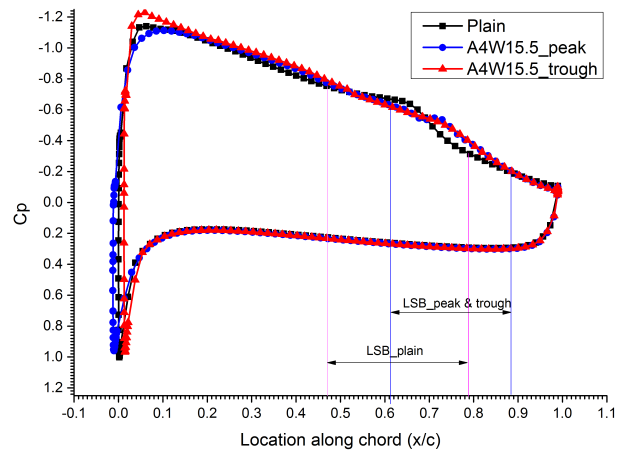
For the model with amplitude 2 mm and wavelength 62 mm (A2W62), peak-suction pressure for both peak and trough sections is increased to -1.06 and -1.20 respectively as shown in Figure 4.39c. The pressure distribution of peak near the leading edge is similar to the baseline with a slight shift of suction peak position towards trailing edge. The separation behind trough starts at  $x/c = 0.48$  and reattaches at  $0.74$  resulting in LSB

length of  $0.26c$  and for peak starts at  $x/c = 0.55$  and ends at  $0.81$  with total bubble length of  $0.26c$ . The intensity and net length of LSB formed is less than baseline model. The LSB formed in wavy shape in the span-wise direction with average reduction in LSB length by  $16.1\%$ .

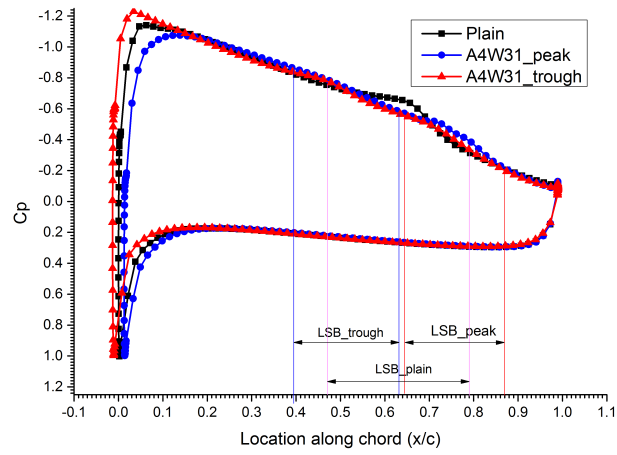
The  $C_p$  distribution of airfoil A4W15.5 is similar to A2W15.5 with a suction peak of  $-1.12$  and  $-1.22$  respectively as in Figure 4.40a. Compared to the unmodified airfoil, a weak LSB is formed in similar locations along peak and trough at  $x/c = 0.61$  to  $0.88$ . When the wavelength is increased to  $31$  mm and  $62$  mm, trend of  $C_p$  distribution is similar to that in case of the model with amplitude  $2$  mm. Here the LSB has a wavy shape for models with wavelength of  $31$  mm and  $62$  mm. Further details are listed in Table 4.1.

For the model A8W15.5, the suction peak is similar to that of baseline model on peak and trough as shown in Figure 4.41a. The LSB formation reduced, with smooth surface pressure variation compared to the baseline. Here the LSB is formed at same stream-wise locations, from  $x/c = 0.65$  to  $0.87$ , along trough and peak. The LSB has a length of  $0.22c$ , which is shorter than baseline model by  $29\%$ . The location of LSB is shifted towards trailing edge compared to baseline. When the wavelength is increased, the LSB forms in a wavy shape with higher intensity as in the previous cases. For the model A8W31, length of LSB along trough is  $0.22c$  and that along the peak is  $0.21c$  with average length reduction of  $31.6\%$ . The LSB length for A8W62 is  $0.21c$  and  $0.25c$  behind trough and peak respectively with average bubble length reduced by  $25.8\%$ . More details are given in Table 4.1.

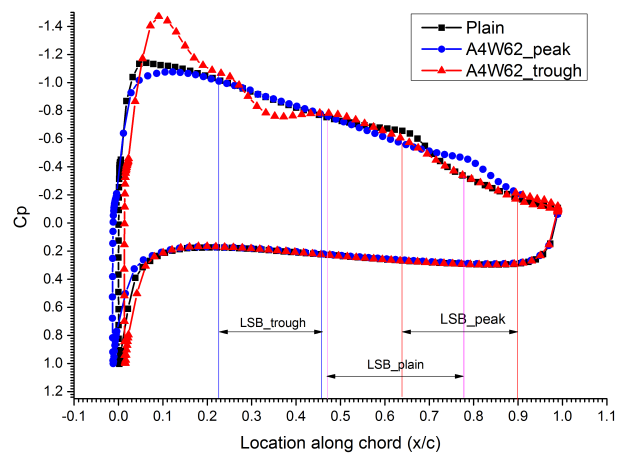
Increasing wavelength at constant amplitude reduces the length of LSB behind trough and increases behind the peak. Except for lowest wavelength, LSB is formed in a wavy shape. For smallest wavelength ( $15.5$  mm), flow disturbance generated by the tubercle promotes immediate span-wise mixing of fluid owing to its the smallest



(a)



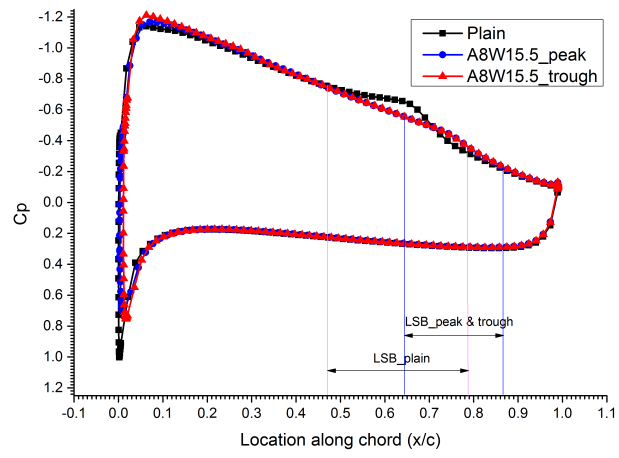
(b)



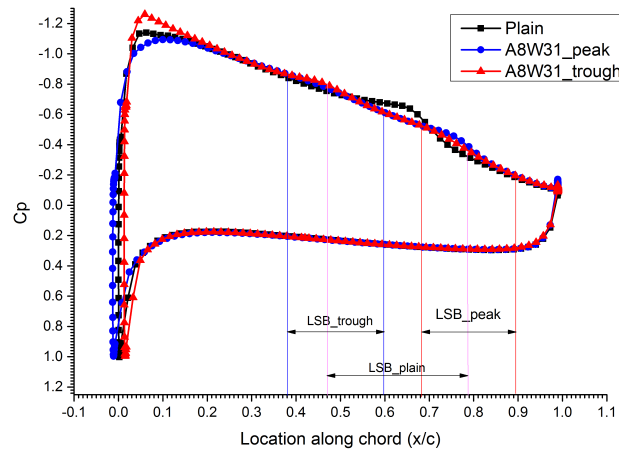
(c)

Figure 4.40:  $C_p$  distribution on modified and unmodified models at AOA of  $4^\circ$

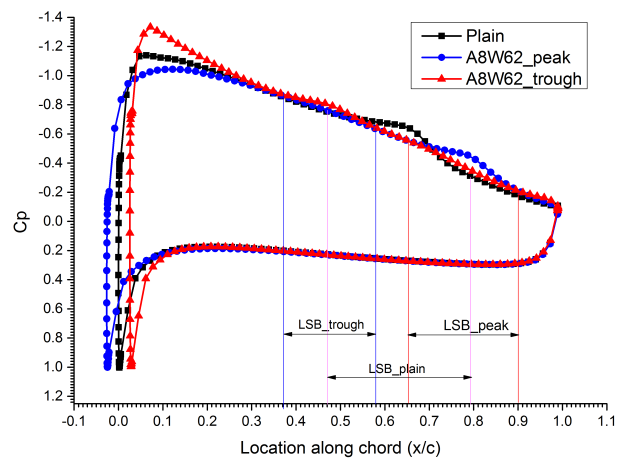




(a)



(b)



(c)

Figure 4.41:  $C_p$  distribution for modified and unmodified models at AOA of  $4^\circ$

Table 4.1: Laminar separation bubble location and size on baseline and modified models

Model	Laminar Seaparation bubble					
	trough			peak		
	Begin(x/c = )	End(x/c = )	Length(%c)	Begin(x/c = )	End(x/c = )	Length(%c)
Plain	0.48	0.79	0.31	0.48	0.79	0.31
A2W15.5	0.63	0.92	0.29	0.63	0.92	0.29
A2W31	0.49	0.77	0.28	0.59	0.82	0.23
A2W62	0.48	0.74	0.26	0.55	0.81	0.26
A4W15.5	0.61	0.88	0.27	0.61	0.88	0.27
A4W31	0.39	0.63	0.24	0.65	0.87	0.22
A4W62	0.23	0.46	0.23	0.64	0.90	0.26
AW15.5	0.65	0.87	0.22	0.65	0.87	0.22
A8W31	0.38	0.60	0.22	0.69	0.90	0.21
A8W62	0.37	0.58	0.21	0.65	0.90	0.25

amplitude and wavelength. This results in uniform flow property along the span-wise location prior to LSB formation and formation of the LSB at the same span-wise location behind trough and peak of the model. It also energizes the flow which results in the formation of smaller LSB compared to other models. Size of LSB formed behind trough reduces with increase in wavelength and at the same time the size increases behind the peak. Laminar separation point is also slightly moved towards leading edge during the formation of LSB behind trough and peak at a higher wavelength. Increasing amplitude results in the reduction of LSB length in all the cases. Laminar separation point slightly moves towards leading edge behind trough and the point moves towards the trailing edge for the LSB formed behind the peak.

#### 4.7.4 Surface flow pattern analysis

Surface flow visualization over the baseline and modified airfoil A4W31 near the leading edge is shown in Figure 4.42. Flow near the airfoil leading edge is divided into two parts by a bifurcation line, one flow passes over the suction surface and the other over pressure surface. Also for baseline model, the flow after the bifurcation line, goes straight towards trailing edge (Figure 4.42(a)) but for modified one, it turns slightly in spanwise direction as seen in Figure 4.42(b).

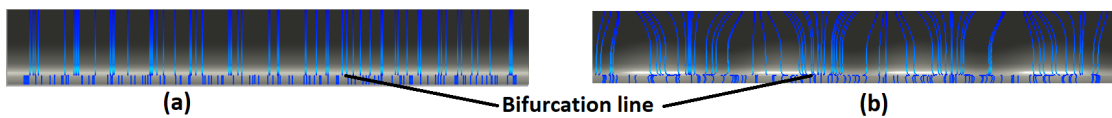


Figure 4.42: Front view of the (a)baseline and (b)modified airfoil-A4W31 with surface streamlines, showing the bifurcation line

It indicates that the tubercle modifies the flow from the leading edge itself by inducing some spanwise flow component. As the flow approaches the leading edge of the modified airfoil, the flow is redirected due to the waviness and the bulk of the flow is

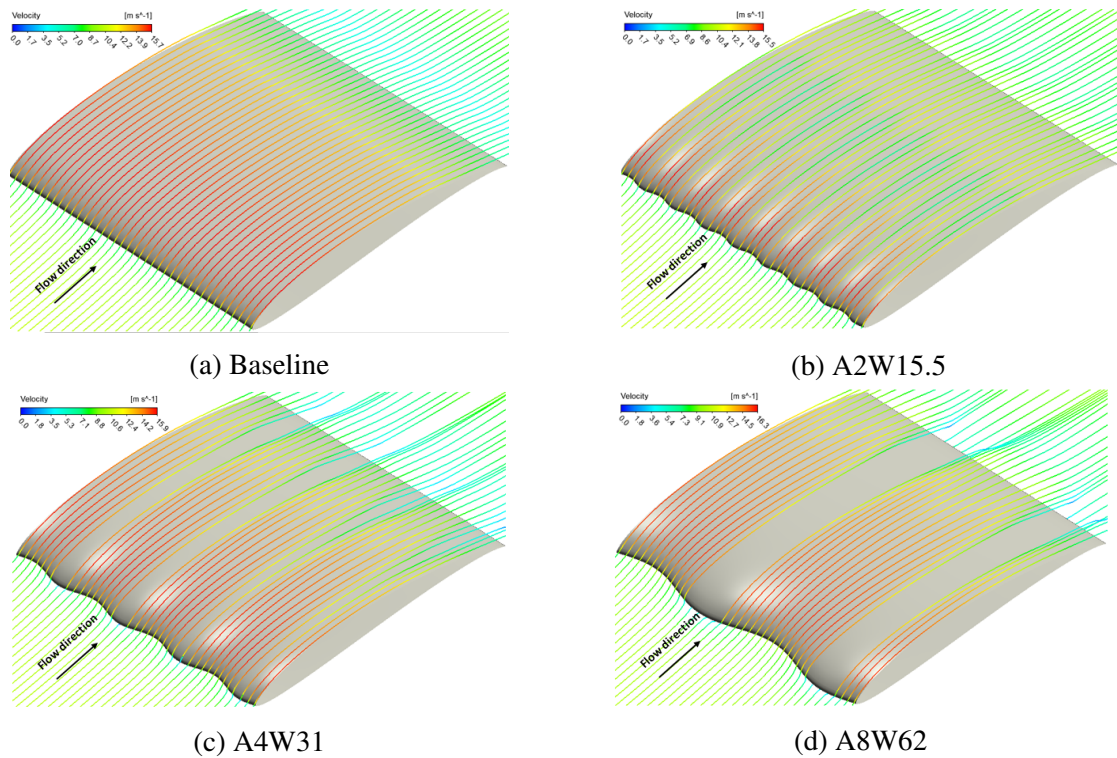


Figure 4.43: Three dimensional streamline over the airfoils

bunched and flows towards the trough region as shown in Figure 4.43. For comparison purpose, flow over baseline airfoil is shown in Figure 4.43a, where the flow passes uniformly over the leading edge. The redirected flow gets accelerates in the trough and attains high velocity as seen in figures (with red coloured streamlines) compared to peak and baseline flow. Consequently, there is lower pressure in the trough and higher pressure in the peak.

The same is illustrated in Figure 4.44 where the comparison of pressure contour on various tubercle models along with baseline at AOA of  $4^0$  is shown. The baseline has specific regions of constant pressure zones along the spanwise direction as seen in Figure 4.44a. The pressure gradient is observed only in streamwise direction. In case of the modified airfoils, a strong spanwise pressure gradient is established by the tubercle in a cyclic manner compared to baseline on account of the accelerated flow though the trough. The low-pressure region is developed in the trough and high-pressure region

is formed over the peak. It indicates that the lowest suction peak is formed at trough rather than at the peak. This pressure gradient is observed on all the modified models and the region of influence increases with wavelength.

The flow has a tendency to turn spanwise from peak to trough driven by this cyclic pressure gradient, where the low-inertia near-wall fluid is drawn towards the low-pressure trough region from the peak as shown in Figure 4.45. The model with lowest amplitude and wavelength has less tendency for the movement (Figure 4.45a) whereas the tendency increases with increase in wavelength due to the larger low-pressure region as shown in Figure 4.45b and 4.45c. The inclined flow further leads to complex flow structures like laminar separation bubble and multiple three-dimensional vortices as shown in Figure 4.45.

Flow separation from the airfoil surface first occurs at the point S1 along the trough, marked in the Figures 4.46 and the separation is bounded by a parting line around these vortices along spanwise. The foci F1 and F2 lie inside the separation region (LSB). The separated flow re-attaches at point R1 along the trough as shown in the Figure 4.46. After formation of primary vortices, a part of the stream flows downstream whereas the other part of the flow forms a pair of vortices behind the primary vortices called the secondary vortices with foci F3 and F4 marked in the Figure 4.46. The secondary vortices are larger in size than the primary vortices. The flow moving downstream serves as a parting line between the vortices in both primary and secondary pair of vortices and the stream does not participate in any of the vortex formation.

Along the peak, the secondary vortices serve as the reference for laminar separation. The region between the secondary vortices, marked by point S2 and R2 serves as the separation and re-attachment points. Since the separation points S1 and S2 as well as the re-attachment points R1 and R2 are at different streamwise locations, it can be in-

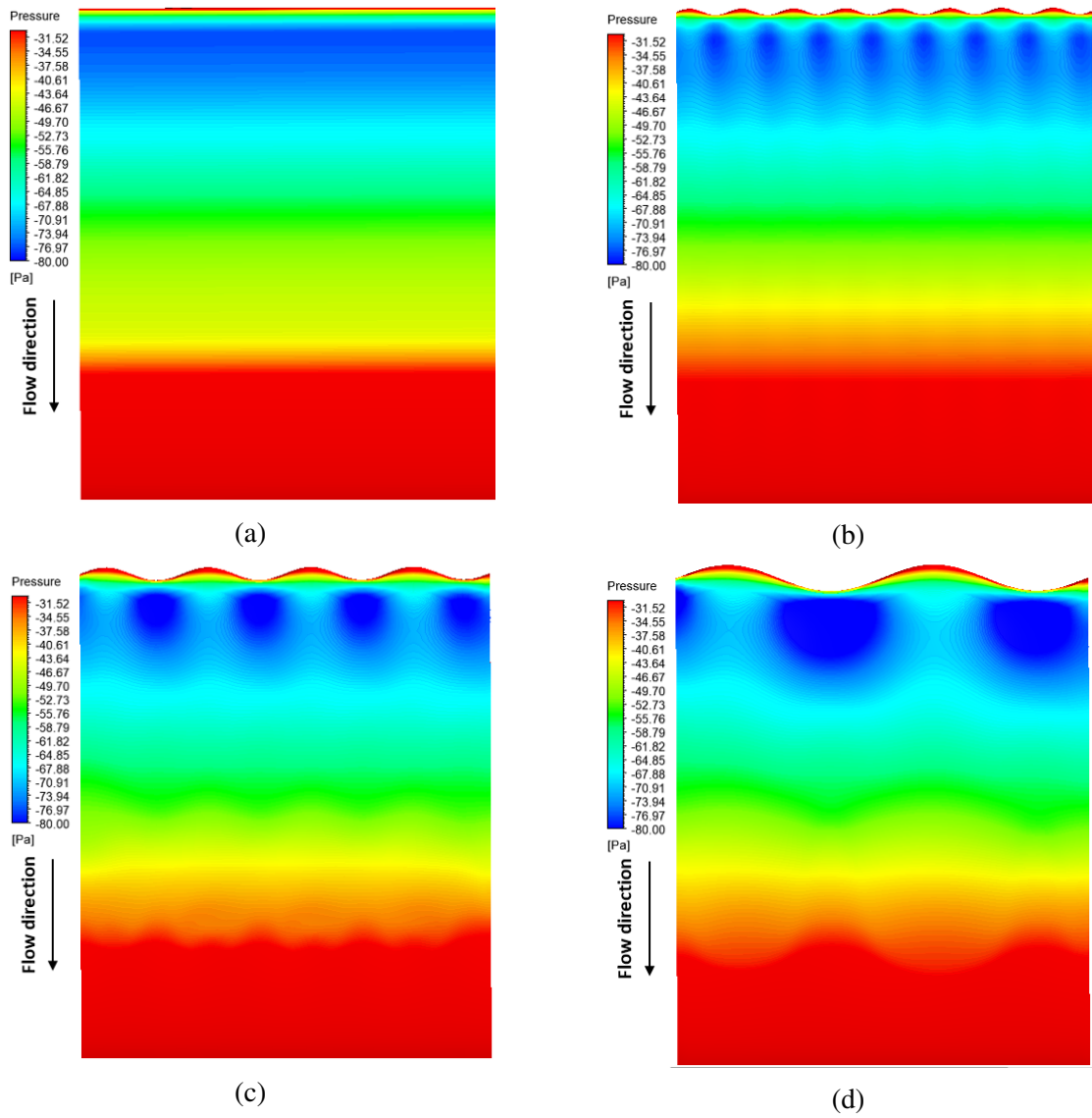
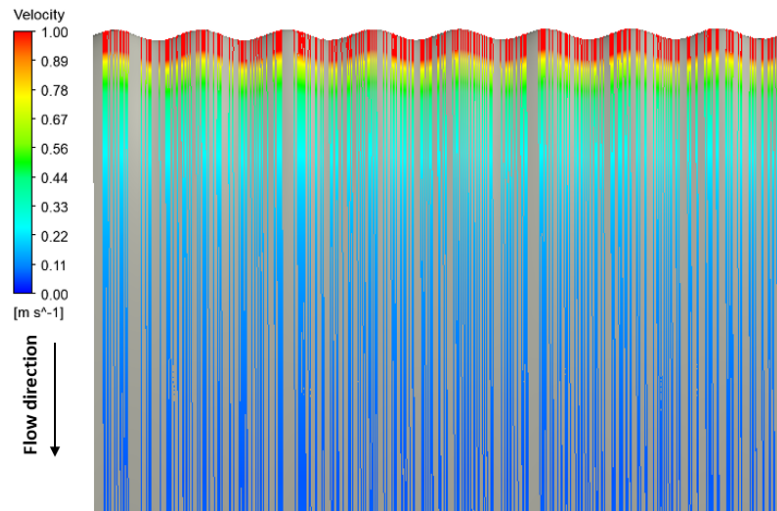
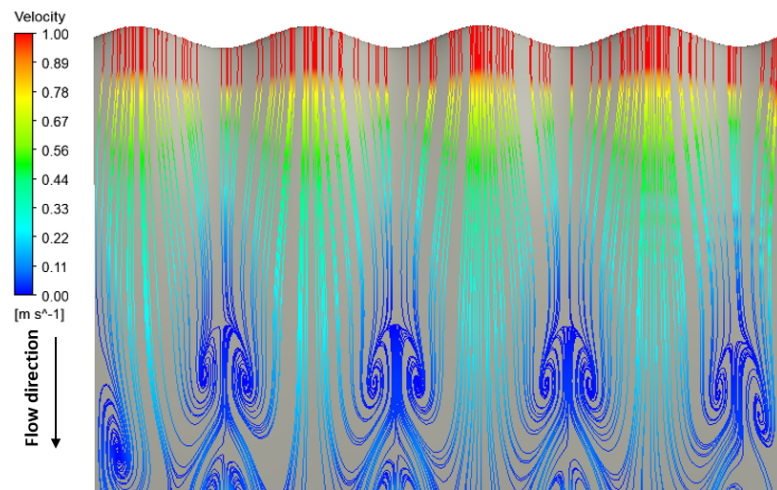


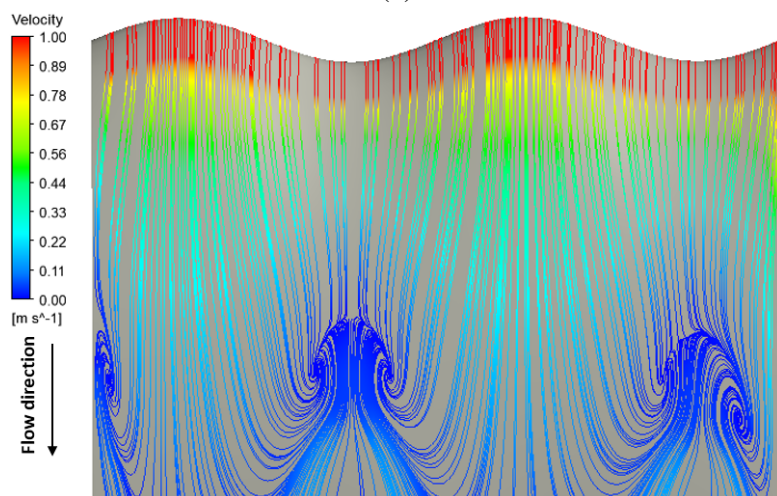
Figure 4.44: Contours of pressure on the suction surface: (a) Baseline (b)A2W15.5, (c) A4W31 and (d) A8W62 at  $AOA = 4^{\circ}$ .



(a)



(b)



(c)

Figure 4.45: Velocity streamlines on the suction surface showing the flow inclining from peak to trough at  $AOA = 4^\circ$  : (a) A2W15.5, (b) A4W31 and (c) A8W62.

ferred that the LSB forms a sinusoidal shape, resembling the leading edge of the airfoil.

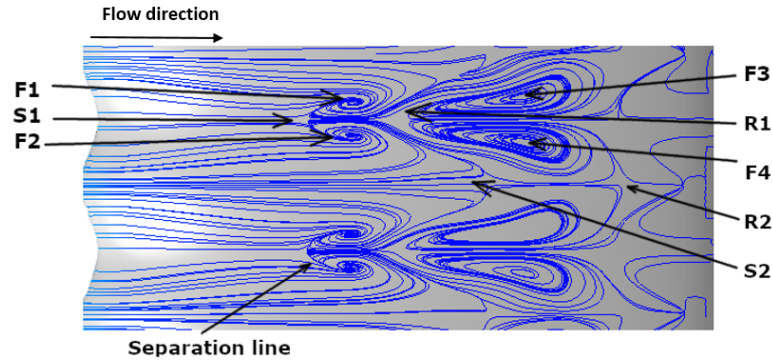


Figure 4.46: Surface streamlines on A4W31 marked with different regions in the flow pattern at  $AOA = 4^\circ$  (flow is from left to right)

The separation region is well seen in the Figure 4.47 where iso-surface of zero velocity is plotted. The blue region represents the separated flow. The baseline model has specific region of separation bounded by clear straight separation and reattachment line along the spanwise direction as seen in Figure 4.47a. Trailing edge (TE) separation also occurs in a straight manner. The A2W15.5 model has no LSB formation as depicted previously with wavy TE separation. The A4W31 model has wavy laminar separation with clear separation and reattachment lines with wavy TE separation as shown in figure 4.47c. For the model A8W62, due to high amplitude, some portion of the laminar separation coalesce with TE separation as shown in Figure 4.47d. The corresponding plots for other models are given in Appendix A, Figure A.4. The velocity of flow through the trough is high compared to peak due to the tunnelling effect as explained. This results in increase of local  $Re$  which promotes early separation of laminar flow compared to that in the peak giving rise to wavy LSB. The presence of streamwise vortices enhances the boundary layer momentum exchange, which leads to reduced size of the LSB on modified models compared to baseline.

To probe further details of the flow structure formation, three-dimensional behaviors of flow is studied. The streamlines, after the primary vortex formation, are lifted



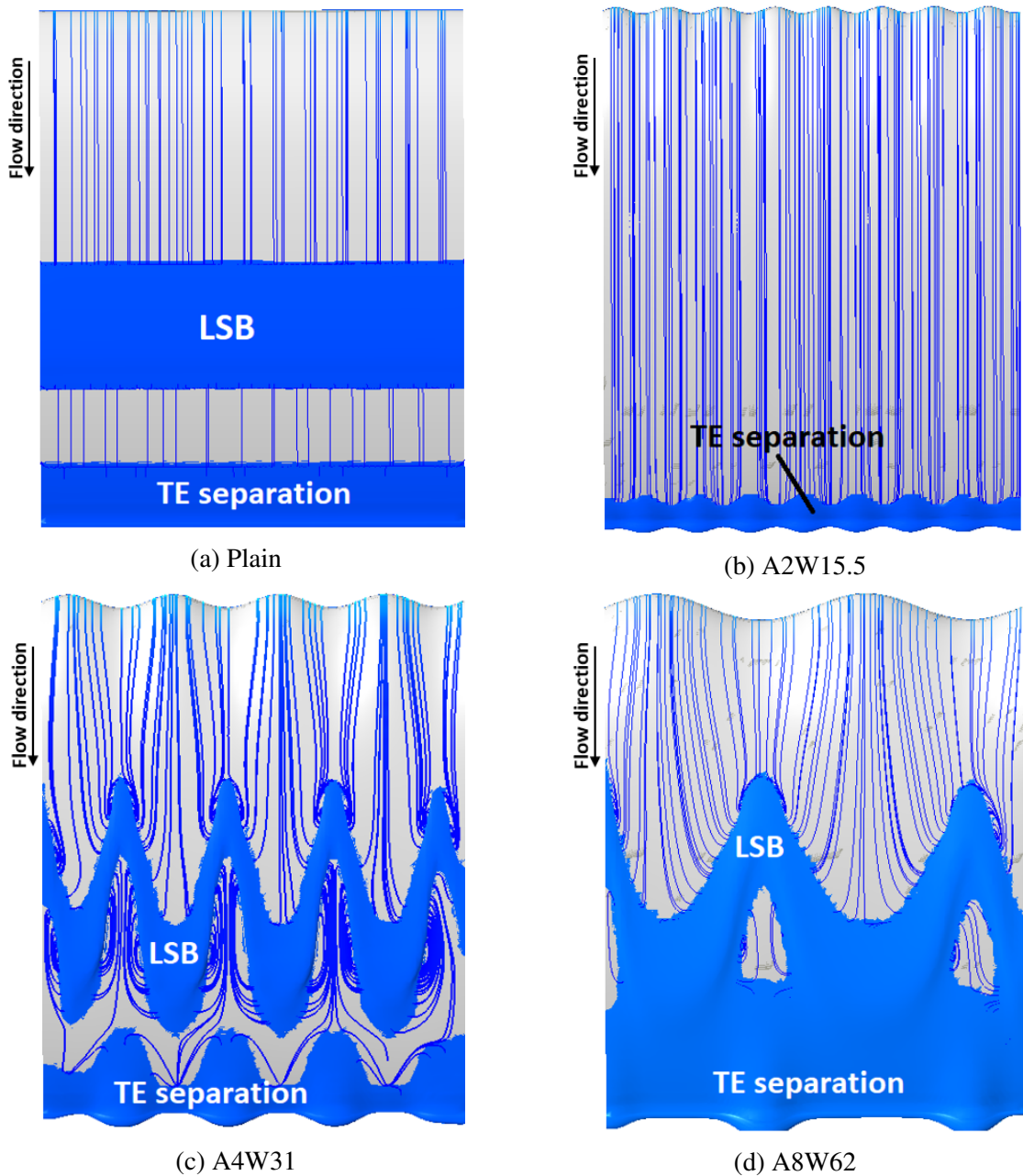


Figure 4.47: Iso surface of zero velocity over the airfoils showing the region of separation(LSB) along with surface streamlines at AOA of  $4^\circ$  (continuous blue area shows the separation region and flow is from top to down)

away from the surfaces and move downstream in a path between the secondary vortices as shown in the Figure 4.48. Since the flow initially participates in the primary vortex formation and then lifts up, thorough mixing of the flow with higher energy flow takes

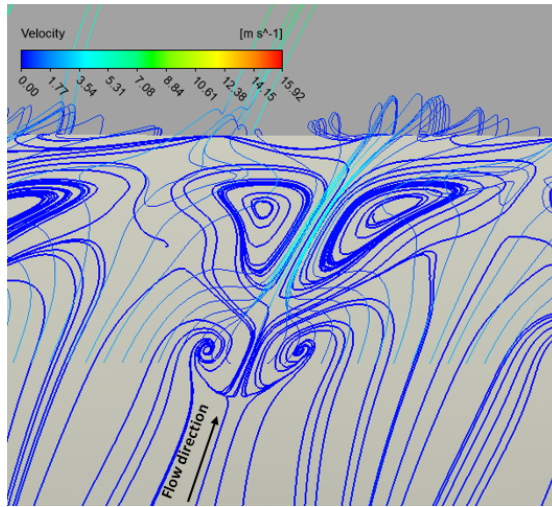


Figure 4.48: Three dimensional velocity streamlines emerging from the primary vortices(A4W31 at AOA =  $4^{\circ}$ )

place and higher energy exchange is achieved as seen in the Figure 4.48. The flow directly coming from the peak, without any spanwise trend, participates in secondary vortex formation. To further investigate the 3D flow structure over the airfoil, streamlines are plotted on multiple planes normal to the flow direction starting at  $x/c = 0.33$  as shown in Figure 4.49. The first plane is at the beginning of primary vortex formation region where the flow separates from airfoil surface as seen in the Figure 4.49a. As the plane moves towards the trailing edge, the separation increases and starts forming 3D vortices as seen in Figure 4.49e. A pair of clear 3D vortices is formed then (Figure 4.49f) with foci F5 and F6 and these vortices themselves circulate about the foci F1 and F2 which is formed on the surface of the airfoil (Figures 4.49g-4.49i). Once it reaches the points F1 and F2, the flow rises up and mixes with mainstream flow.

#### 4.7.5 Flow physics

It is seen from the Figure 4.43 that as the flow approaches the leading edge of the tubercled airfoil, with the flow direction or streamline curvature changes suddenly resulting in re-organisation of spanwise vorticity into the transverse and streamwise directions, generating streamwise vorticity as seen in the Figure 4.49. This kind of vorticity is re-

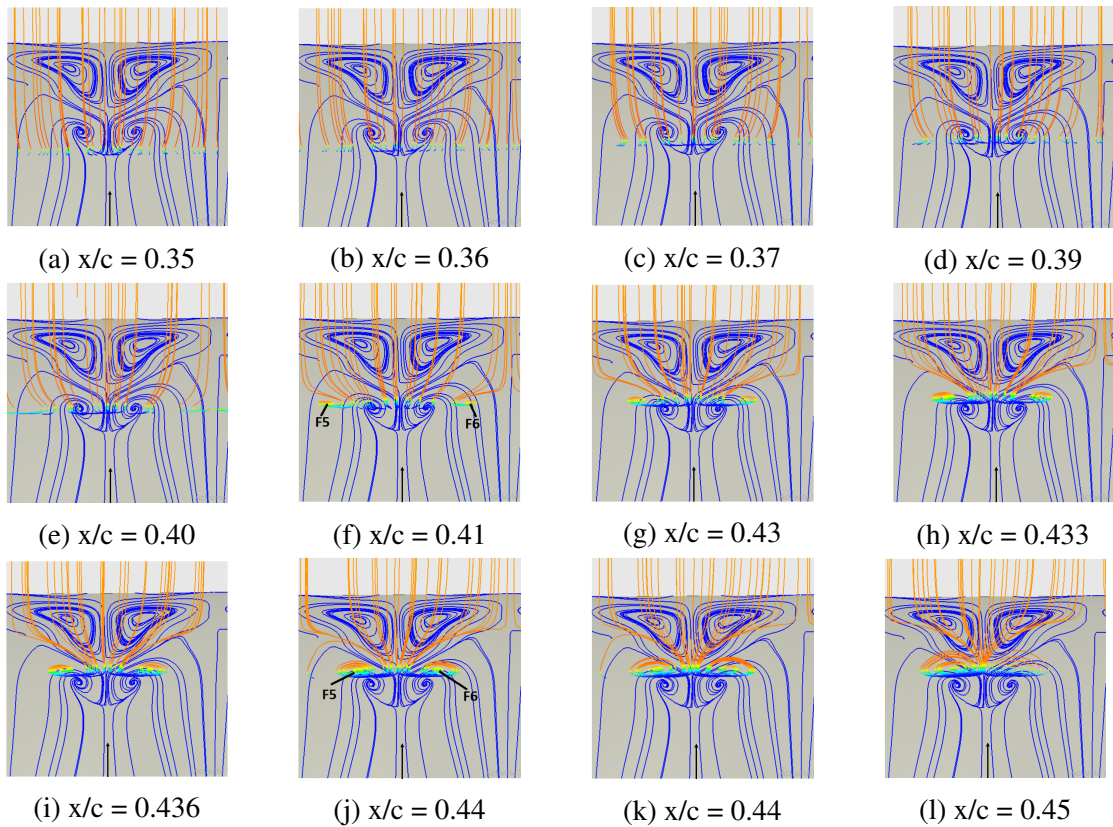


Figure 4.49: Three-Dimensional vortex formation plotted on different planes normal to airfoil surface at different  $x/c$  distance starting from leading edge of the tubercle model A4W31 at AOA of  $4^\circ$

ferred to as “skew-induced” vorticity and the phenomena is called *Prandtl’s secondary flow of the first kind* (Rostamzadeh *et al.* 2014). This streamwise vortices induce high near-wall velocity gradient resulting in high shear stress. Such high shear stress results in additional skin friction drag and net increase in total drag for the modified airfoil.

When the spacing between the tubercles is less (model A2W15.5), they act like turbulence generator resulting in high boundary layer mixing. The flow becomes turbulent all over the airfoil with attached boundary layer over the airfoil surface. This turbulent flow produces detrimental effect on the performance as noticed for vortex generator (Godard and Stanislas 2006) and results in reduced performance of the model even with the LSB elimination.

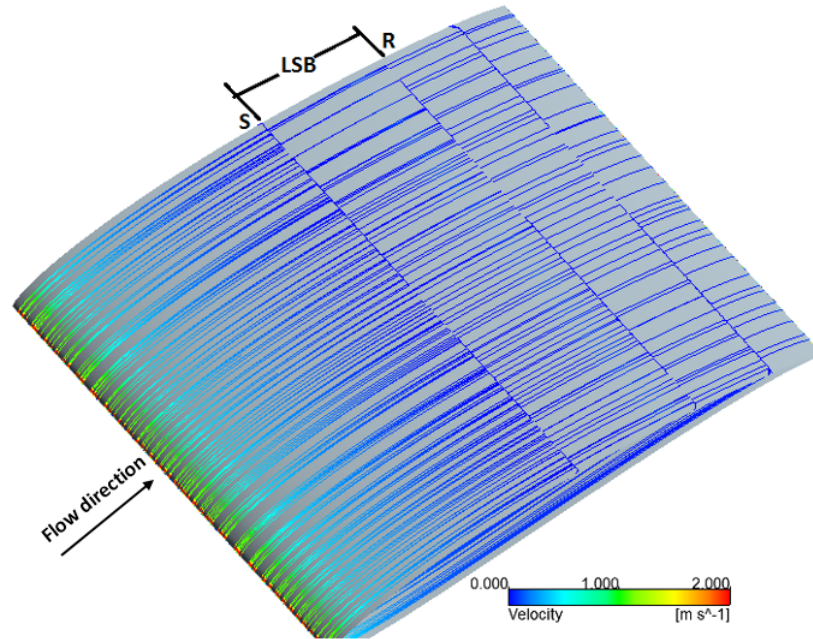
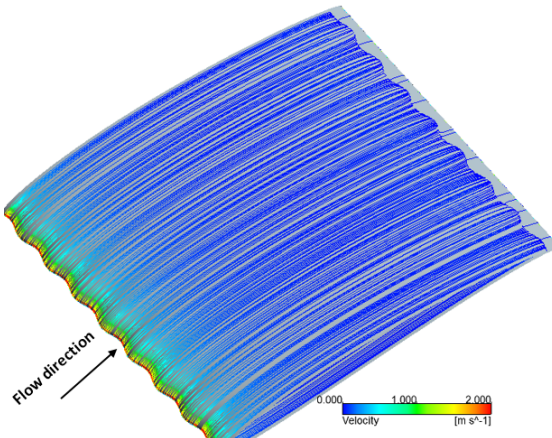


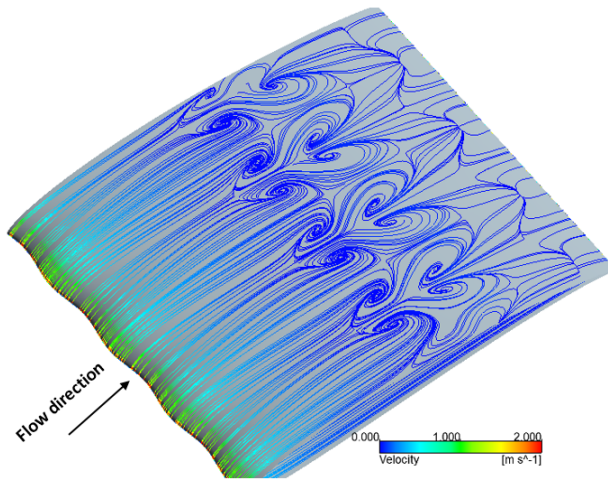
Figure 4.50: Surface streamline pattern on plain airfoil model at AOA of  $4^\circ$

Figure 4.50 shows the surface streamlines on the suction surface of the baseline airfoil at AOA of  $4^\circ$ . The region of LSB is clearly visible on the surface streamline pattern. The observed location is in-line with the  $C_p$  distribution plot for the baseline. The separation starts at nearly  $0.47c$  represented by the reduced density of streamlines. Once the separation starts, the streamlines move away from the airfoil surface and streamline density reduces thereafter. A clear parting line can be observed at the separation (S) and the reattachment point (R). Thereafter, the flow continues as turbulent.

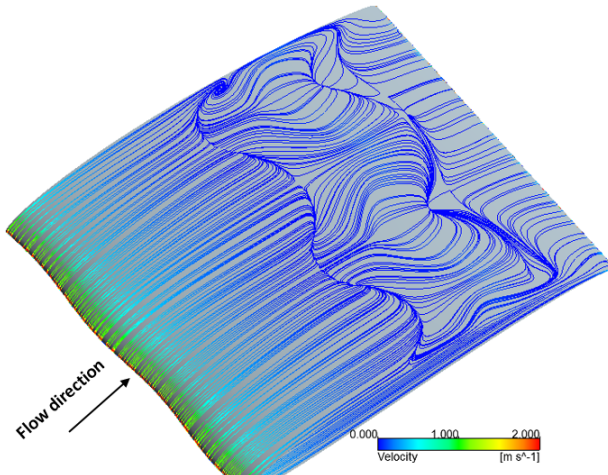
Streamline distribution of modified airfoils at  $4^\circ$  AOA is shown in Figure 4.51 for various combination of amplitude and wavelength. The model with the lowest amplitude and wavelength (A2W15.5) (Figure 4.51a) shows no sign of LSB compared to the baseline as observed in  $C_p$  plot. Presence of tubercle on airfoil causes shifting of LSB closer to its trailing edge and streamlines continue as attached till there. Increase in wavelength results in a complex flow pattern over the surface compared to baseline as



(a) A2W15.5

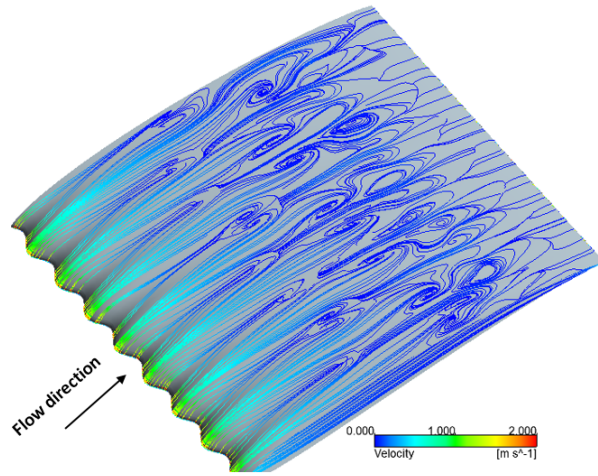


(b) A2W31

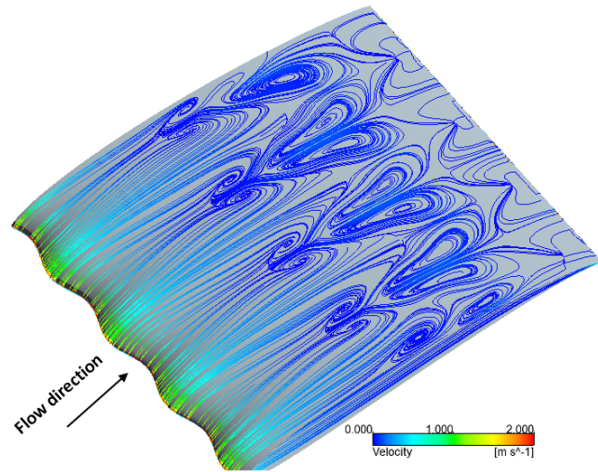


(c) A2W62

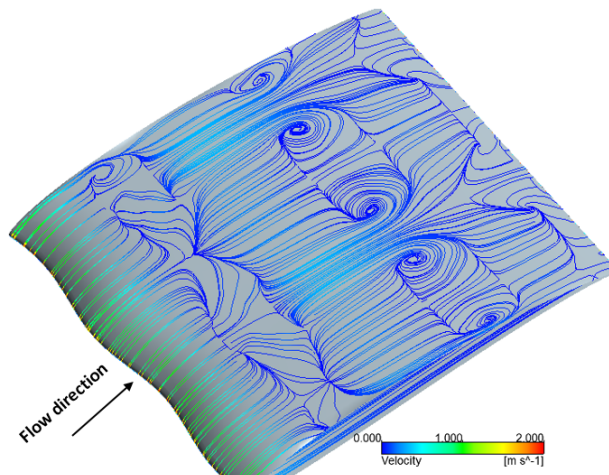
Figure 4.51: Surface streamlines distribution over modified airfoils



(d) A4W15.5

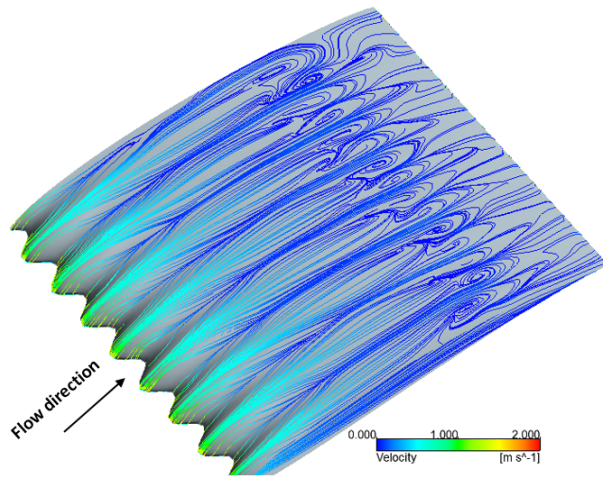


(e) A4W31

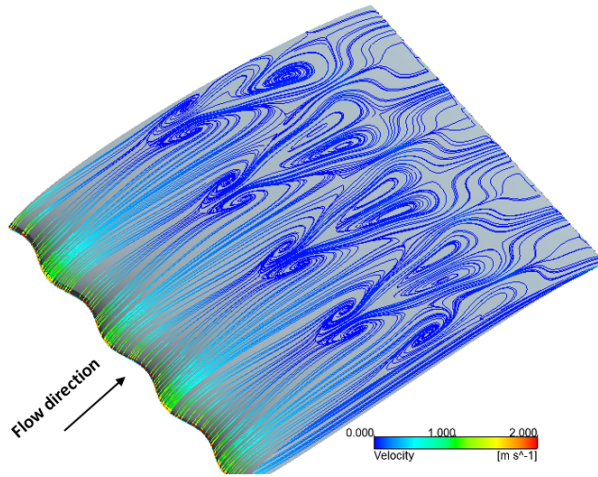


(f) A4W62

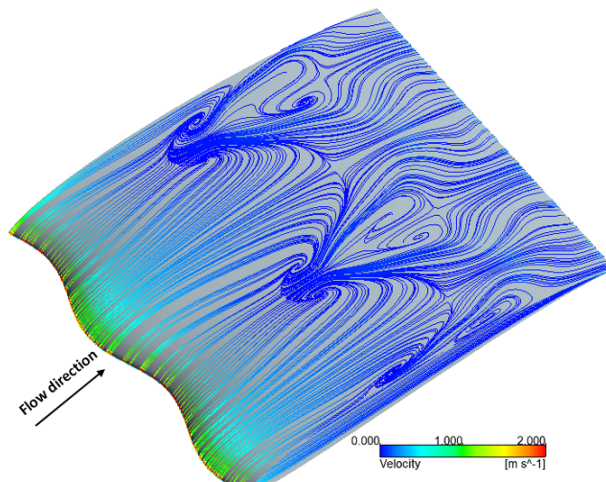
Figure 4.51: Surface streamlines distribution over modified airfoils



(g) A8W15.5



(h) A8W31



(i) A8W62

Figure 4.51: Surface streamlines distribution over modified airfoils

shown in Figure 4.51b. A certain portion of the flow emerging from leading edge moves from peak to trough and forms a recirculation region (primary vortices) in the space between the peak and the trough. At the same time, the flow in the trough interacts with the recirculating flow from the peak and participate in the vortex formation. Once the flow achieves sufficient energy, the flow further moves in stream-wise direction and forms secondary vortices. The LSB formation is observed for the model from  $C_p$  distribution curve as discussed previously and its position along peak and trough are at different location in stream-wise direction. The point where the flow starts to diverge and form primary vortex serves as the starting point of LSB in trough, whereas the similar point for formation of secondary vortices marks the beginning of LSB along the peak. The position of primary vortices is ahead of secondary vortices along the stream-wise direction and hence the beginning point of LSB along the trough is ahead of that along the peak which results in the formation of LSB in a sinusoidal shape. When the amplitude is increased to 62 mm (A2W62) (Figure 4.51c) there is no clear spot of span-wise vortex formation, instead, the flow is redirected from the peak to trough from the point of separation of flow (LSB). The flow is re-energized as it propagates towards the trailing edge due to turbulent mixing of the span-wise flow and finally forms an attached turbulent flow. A clear parting line for flow separation and reattachment can be observed in a sinusoidal manner along the span-wise direction. The location of LSB along the trough is ahead of that at the peak in stream-wise direction.

Multiple small vortices along the stream-wise direction are formed on model with a medium amplitude of 4 mm and least wavelength of 15.5 mm (A4W15.5) (Figure 4.51d). Two kinds of primary vortex formations are observed at the trough of the airfoil surface, a strong vortex, which is tri-periodic and a weaker vortex at the two troughs in between. Both type of vortices start from the same location along the span-wise direction which represents the beginning of laminar separation. After forming multiples vortices, finally, the flow re-attaches at the same chord-wise location towards the trailing edge. Also, the LSB formation occurs at the same chord-wise location along



peak and trough, and the same is depicted in  $C_p$  plot in the previous section. When the wavelength is increased to 31 mm (A4W31)(Figure 4.51e) the streamline pattern is formed exactly similar to that for A2W31 but differ only in size. When the amplitude is increased, more shallow flow passages are formed which causes elongated vortices in the stream-wise direction. Laminar separation points are represented by the beginning of vortices as described previously.

Further increase in amplitude to 8 mm with a wavelength of 15.5 mm (A8W15.5) makes the surface with deep bumps. This restricts the flow to stream-wise direction and slightly energizes the flow that results in delayed LSB formation or vortex formation. The counter-rotating vortices are formed in the region between the peak and trough at the same chord-wise location. With further increase of wavelength to 31mm (A8W31, Figure 4.51h) and 62 mm (A8W62, Figure 4.51i), vortex formation is same as their respective previous cases with amplitude 2 mm and 4 mm as described previously with the slight difference only in the strength and shape of vortices. As the amplitude is increased, the vortices become longer in chord-wise direction and shorter in width. Further, the primary vortices become more dominant with increase in amplitude, compared to previous shorter amplitudes.

The modified airfoil models generate lift similar to baseline model. This trend is similar to that for vortex generator (Stein and Murray 2005) and hence the pair of counter-rotating vortices act like vortex generator. The presence of stream-wise, counter-rotating vortices thins the boundary layer in down-wash areas on the airfoil surface(Bolzon *et al.* 2015). This results in increased near-wall velocity gradient, and therefore increased shear stress. This increased shear stress induces additional skin friction drag and net increase in total drag of the modified models as seen in Figures 4.34 and 4.37.

It is seen that as the spacing between the tubercles is reduced (cases with wavelength 15.5 mm) they act more like turbulence generator. It is noticed that more uniform boundary layer mixing leading to better attachment of boundary layer over the airfoil surface takes place. This mixing makes the flow turbulent and produces detrimental effect on the performance as was found for vortex generator (Godard and Stanislas 2006). This is the reason for the reduced performance of model with the least wavelength (15.5 mm) even with the LSB elimination.

Hansen (2012) observed down-wash along peak and comparatively up-wash along trough on airfoil with tubercles. The presence of down-wash flow along peak results in suppression of Tollmien-Schlichting wave (T-S wave) formation which is one of the mechanism in transition of flow from laminar to turbulent as seen in LSB formation. Along with that, modification of airfoil with tubercle considerably varies the chord length from peak to peak in span-wise direction. This results in variation of chord-based Re of airfoil from peak to peak in span-wise direction. In case of an airfoil with tubercle, the Re is maximum at peak and it gradually reduces to minimum at trough and it increases again. Increase in Re makes the LSB to move downstream of the flow (Lyon *et al.* 1997). Combined effect of suppressed T-S wave due to down-wash flow along the peak and the variation in Re delays the LSB formation delayed along peak compared to trough. This results in the formation of LSB in a wavy-manner.

Location and size of LSB on airfoil depends on many kinds of flow and geometrical parameters. Figure 4.52 shows velocity variation at different stream-wise and span-wise locations on A2W31 model at AOA of  $4^{\circ}$ . It can be seen from the figure that, along the peak the flow has higher velocity in stream-wise direction compared to that in the trough. Because of this momentum difference, flow from the peak has a tendency to move towards trough as flow progress and which constitute a span-wise flow from peak to trough as shown in the Figure 4.52.

From the Figure 4.53 it can be noted that pressure over the peaks is greater than in the troughs. This causes span-wise flow from peak to trough as shown in Figure 4.52. Due to this low pressure over the troughs, the pressure gradient in the troughs remains higher than that over the peaks (in turn velocity gradient as shown in the Figure 4.52). This high pressure gradient (velocity gradient) leads to premature separation and hence it also contributes for the occurrence of LSB upstream that of peak and formation of LSB in wavy manner. The momentum exchange rate increases due to the combined effect of this span-wise flow from peak to trough as well as the formation of counter-vortices between the peak and the trough, consequently bubble size reduces.

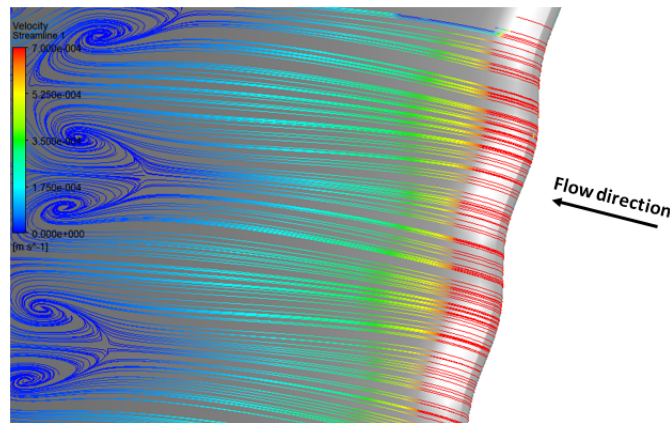


Figure 4.52: Velocity stream lines on A2W31 at AOA of  $4^\circ$ , showing velocity variation at different stream-wise and span-wise locations

## 4.8 BLADE DESIGN

Length of blade to deliver 100 W of rated power is calculated from equation 3.41 and found to be 1 m. Tip speed ratio is fixed to 5.8 (Manwell *et al.* (2010)) which corresponds to wind speed of 6.5 m/s. The chord and pitch distribution along the span of designed blade obtained from the BEM theory coded in MATLAB is given in table.4.2.

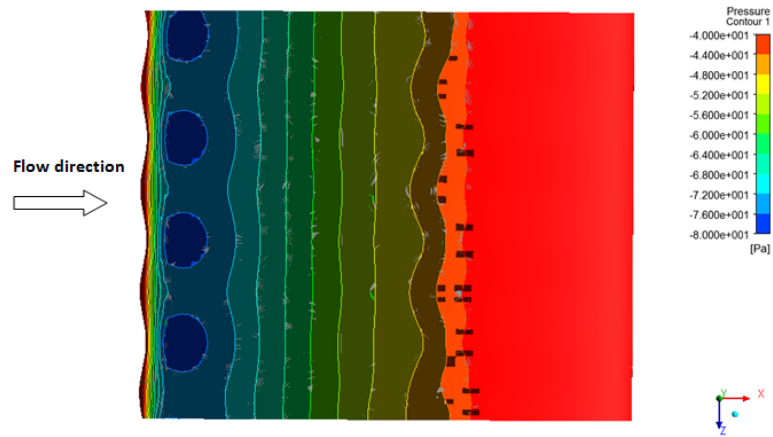


Figure 4.53: Pressure contour on A2W31 at AOA of  $4^\circ$ , showing pressure variation at peak and trough

Corresponding airfoil configuration and orientation along the blade length is shown in Figures 4.54 & 4.55 respectively. The CAD model of the generated turbine geometry is shown in Figure 4.56.

Table 4.2: Geometrical parameters of blade

Radial sections ( $r/c$ )	$c$ (m)	$\beta$ ( $^\circ$ )
0.1	0.17	33.07
0.15	0.17	25.81
0.20	0.16	20.34
0.25	0.15	16.22
0.30	0.13	13.07
0.35	0.12	10.62
0.4	0.11	8.67
0.45	0.10	7.09
0.50	0.09	5.79
0.55	0.08	4.70
0.60	0.08	3.77
0.65	0.07	2.97
0.70	0.07	2.27
0.80	0.06	1.07
0.85	0.05	0.52
0.90	0.05	-0.07
0.95	0.04	-0.84

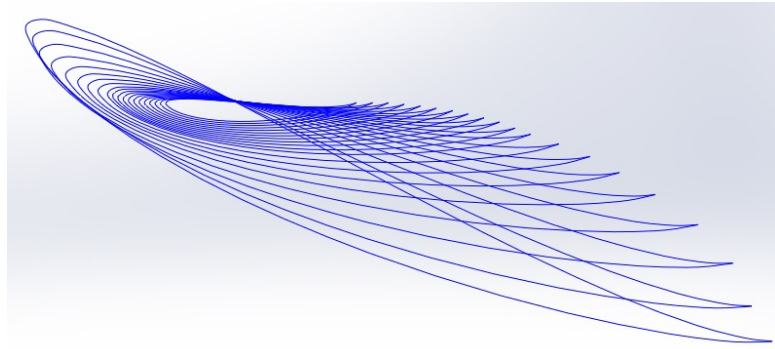


Figure 4.54: Blade sections (bottom view)



Figure 4.55: Blade sections

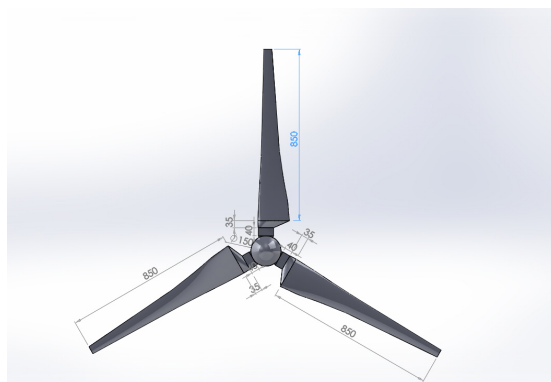


Figure 4.56: CAD geometry of generated turbine model

### 4.8.1 Performance analysis

Axial induction factors ( $a$ ) and coefficient of power ( $C_P$ ) are the main aerodynamic performance measures of a wind turbine blade. The performance is analyzed using the BEM-code and the results are presented in this section. The required input parameter for the BEM code are: Wind velocity ( $U$ ), Tip speed ratio (TSR), radius of the blade ( $R$ ), number of blade ( $B$ ), hub radius ( $r_h$ ), tip radius ( $r_t$ ), kinematic viscosity of air ( $\nu$ ), number of blade section ( $N$ ), lift coefficient ( $C_l$ ) and drag coefficient ( $C_d$ ).

Variation of axial induction factor ( $a$ ) along the blade length is shown in Figure 4.57. Axial induction factor varies from 0.3 at the tip to 0.38 at the root. The theoretical value of the induction factor, from the actuator disc model in the Betz limit, for maximum power extraction is 0.33 (Manwell *et al.* 2010). The result is in the acceptable range of axial induction factor for a small scale wind turbine blade and it proves the validity of the code.

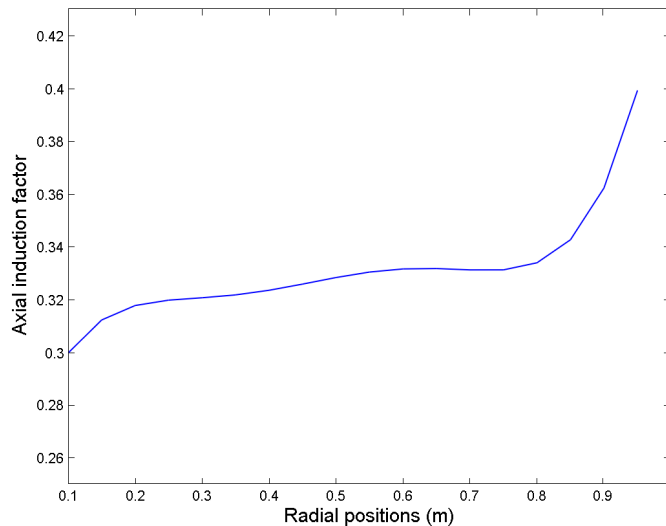


Figure 4.57: Variation of axial induction factor with radius of blade

One of the most important characteristic curves for a wind turbine is its coefficient

of power ( $C_P$ ) variation with respect to tip speed ratio (TSR). Power coefficient for the designed blade at various TSR are obtained from the turbine simulation using the code and it shows a maximum  $C_P$  value of 0.46 at the design TSR of 5.8 (figure4.58). Beyond this TSR the  $C_l/C_d$  of blade sections reduces, consequently, power generation reduced. According to Betz limit maximum theoretical  $C_P$  value is 0.59 and maximum  $C_P$  value of 0.46 obtained in this work matches well with the literature value of 0.41 for SSWT.

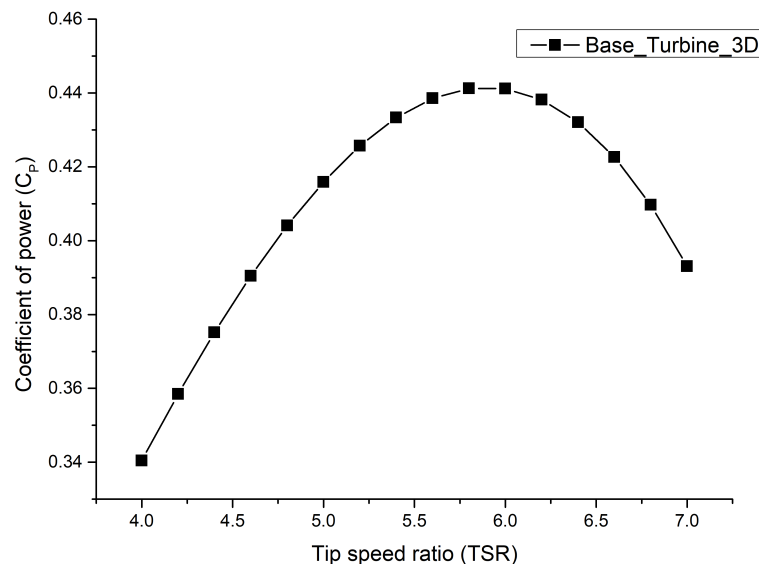


Figure 4.58: Variation of Coefficient of power with Tip Speed Ratio

## 4.9 EFFECT OF BLT AND TUBERCLES ON THE PERFORMANCE OF SSWT

The BLT and tubercles are not directly incorporated on the blade of the turbine, instead the effect is studied by using the respective change in the  $C_l/C_d$  value of modified airfoil with BLT and tubercles. The maximum improvement in  $C_l/C_d$  is obtained for airfoil with rectangular BLT at location-1 and trip height of 0.3 mm and with tubercle

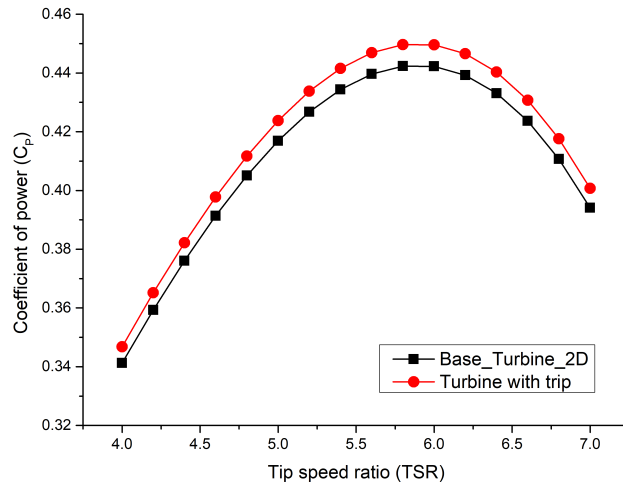


Figure 4.59: Variation of power coefficient of SSWT with BLT for various tip speed ratio

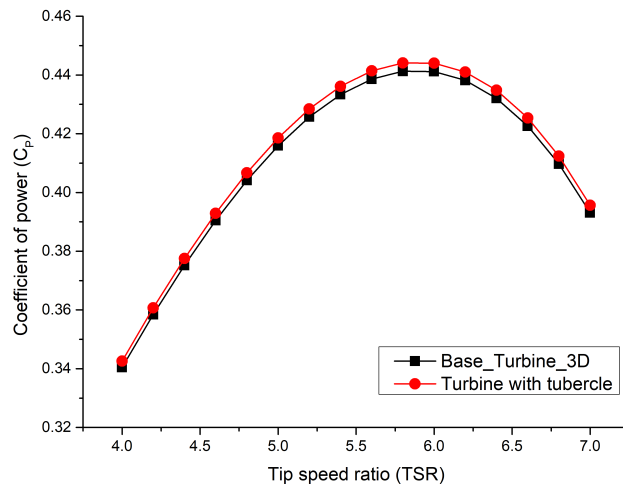


Figure 4.60: Power coefficient variation of SSWT with tubercle for various tip speed ratio

modification, the maximum improvement is achieved with configuration A8W31. The corresponding  $C_l$  and  $C_d$  values are given as input to BEM Matlab code to find out the corresponding improvement in  $C_P$  of the designed turbine. The results are plotted in Figures 4.59 and 4.60 along with baseline  $C_P$  at various tip speed ratio. From the result it can be proposed that average improvement of 1.65% in  $C_P$  can be obtained with the BLT and 0.64% improvement can be achieved with the tubercles.





## CHAPTER 5

### CONCLUSIONS AND SCOPE FOR FUTURE WORK

#### 5.1 CONCLUSIONS

Experimental and numerical investigations are carried out to assess the aerodynamic performance of airfoil E216 with boundary layer trip and tubercles at Reynolds number of  $1 \times 10^5$ . The study examined the effect of these modification on laminar separation bubble formation over the airfoil. The effect of boundary layer trip on the airfoil performance is investigated for different trip shapes (Rectangular, Right angled triangular and Isosceles triangular), heights and position. Whereas, in case of tubercles amplitude and wavelength are varied, to study its effect on airfoil performance and laminar separation bubble formation.

Wind tunnel experimental results showed a lift coefficient of 1.37 and drag coefficient of 0.063 for the airfoil at stall angle of  $12^\circ$ . Maximum  $C_l/C_d$  of 42.46 is observed at critical AOA of  $4^\circ$ . The  $C_p$  plot clearly depicted the presence of laminar separation bubble and the flow separation from the airfoil surface at approximately 0.22c from leading edge at AOA  $6^\circ$ . Numerical results are in good agreement with experimental results and are used for flow pattern study. It is observed that laminar separation bubble moved upstream with increase in angle of attack. The size of the bubble is seen to be reduced with increase in angle of attack. Beyond AOA of  $8^\circ$ , the bubble coalesces with upstream flow. The same is observed in vector plot, which clearly showed the formation of laminar separation bubble.

The  $C_p$  results showed that BLT eliminated LSB partially or completely. The trips

improved aerodynamic performance of the airfoil in majority of the cases. The location-2 is more effective than location-1 and the distance between trip location and LSB plays an important role in net value of  $C_d$ . Increase in trip height beyond 0.7 mm results in increased device drag and net increase in drag than baseline. Highest improvement of 16.7% in  $C_d$  and 34.6% in  $C_l/C_d$  are obtained for location-2 with the rectangular trip having lowest trip height of 0.3 mm at AOA of  $8^\circ$ . In all the cases, improvement in performance is observed only up to trip height of 0.5 mm. There is no observable advantage for isosceles and right-angled triangular trips over rectangular trips.

The tubercled models produced higher  $C_l$  than baseline. However, improvement in  $C_l/C_d$  is marginal for the modified models due to high  $C_d$ . The highest improvement in  $C_l/C_d$  by 7.37% is observed for A2W62 model which produced the peak value of 46.91 at AOA  $6^\circ$ .

It is seen that the tubercles significantly affect the surface pressure distribution on the airfoil and associated flow characteristics. Further, tubercles induce three-dimensional flow features and alter the surface pressure distribution at different configuration of wavelength and amplitude. In most of the cases, suction peak pressure is noticed to be higher along the trough and lower along peak compared to baseline. The difference observed is more at high wavelength. The low amplitude and low wavelength model are noted to exhibit smooth  $C_p$  distribution without any sign of strong LSB formation. The LSB is seen to be formed at different stream-wise direction behind trough and peak inducing three-dimensional wavy LSB unlike straight as in baseline. The tubercles considerably reduce length and width of LSB compared to baseline.

The surface streamline pattern implicate the inclined flow from peak to trough as it advances towards trailing edge. High velocity flow is observed on the peak than the trough. Unlike the previous studies, two pairs of counter rotating vortices are observed

on the airfoil surface between the peak and the trough of the tubercle model at two different chord-wise location. One pair of the counter vortices formed ahead of the other in stream-wise direction. The span-wise flow from peak to trough pre-energize the flow by momentum exchange and the vortices also contribute to momentum exchange in the LSB region, promoting reduction in the length of LSB. The variation in  $Re$  at different span-wise location is the cause of wavy shape of LSB formation.

A conceptual turbine which produces 100 W power with baseline airfoil for its blade is redesigned with best performing boundary layer trip configuration and tubercle configuration. The result proposed that average improvement of 1.65% in  $C_P$  is obtained with the boundary layer trip and 0.64% improvement can be achieved with the tubercle modification.

## **5.2 SCOPE FOR FUTURE WORK**

Experimental studies may be extended to all the modified models. The PIV need to be implemented to experimentally study the flow features and mechanisms. Simulation study can be carried out for transient mode to collect more information related to transition phenomena. Simulation for airfoil with BLT may be done in three dimensional approach to study the span-wise flow effect if any. The simulation may be extended with large eddy simulation to capture much more information related to transition phenomena.



# APPENDIX A

## ADDITIONAL DETAILS RELATED TO EXPERIMENTAL AND NUMERICAL WORK

### A.1 Airfoil terminology

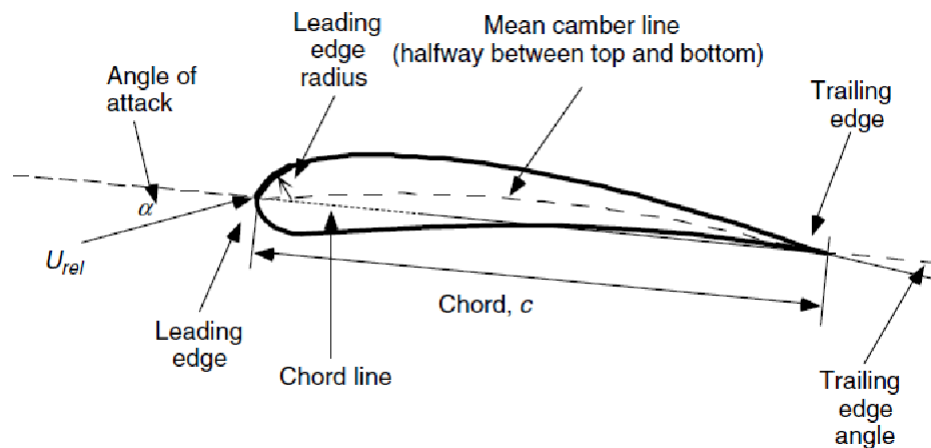


Figure A.1: Airfoil terminology (Manwell *et al.* 2010)

- Mean camber line: locus of points halfway between the upper and lower surfaces of the airfoil
- Leading edge: most front point or frontward end of camber line.
- Trailing edge: extreme rear end of airfoil or most rearward point of camber line
- Chord line: the straight line connecting trailing edge and leading edge.
- Chord length or chord: the length of chord line.
- Camber: distance measured from mean camber line perpendicular to chord line.
- Thickness: distance between upper and lower surface of airfoil measured perpendicular to chord line
- Angle of attack: the angle between relative wind velocity direction and chord line.

## A.2 Drag force and Lift force

When airfoils exposed to incident wind, encounters aerodynamic forces (Figure A.2). Force parallel to wind direction is called Drag force (D) and that perpendicular in direction is called Lift force (L). These forces can be calculated from equations as given below (Kishore 2013).

$$D = C_d \frac{\rho}{2} A' U_\alpha^2 \quad (\text{A.1})$$

$$L = C_l \frac{\rho}{2} A' U_\alpha^2 \quad (\text{A.2})$$

Where,  $A'$  is projected area of airfoil perpendicular to flow direction,  $\rho$  is density of air,  $U_\alpha$  is free stream wind velocity,  $C_l$  coefficient of lift and  $C_d$  coefficient of drag.

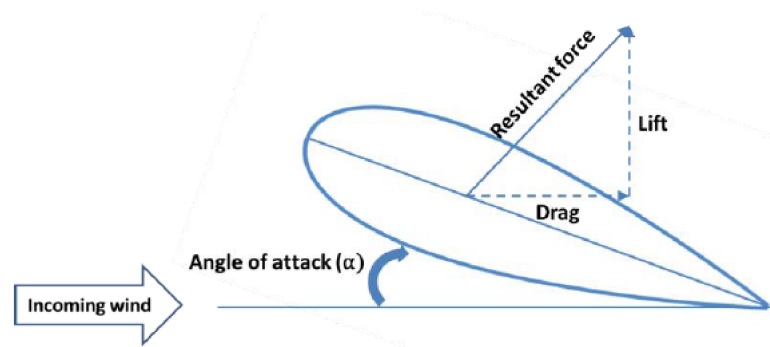


Figure A.2: Lift and drag components of aerodynamic forces (Manwell *et al.* 2010)

## A.3 Airfoil coordinates

Table A.1: E216 airfoil coordinates (UIUC 2014)

x	y	x	y	x	y
1	0	0.3056	0.09475	0.15401	-0.01932
0.99692	0.00141	0.26249	0.09144	0.1942	-0.01742
0.98842	0.00552	0.22169	0.0869	0.23817	-0.0146
0.97564	0.01157	0.18354	0.08119	0.28554	-0.01098
0.95877	0.0184	0.14836	0.07439	0.33588	-0.00675
0.93743	0.02552	0.11644	0.06665	0.38868	-0.0021
0.91162	0.033	0.08803	0.05809	0.44341	0.00276
0.8817	0.04079	0.06333	0.04891	0.49945	0.00757
0.84805	0.04868	0.04254	0.0393	0.55614	0.01211
0.81104	0.05651	0.02576	0.02951	0.61279	0.01611
0.77107	0.06407	0.01311	0.01981	0.66862	0.01937
0.72855	0.0712	0.00461	0.01058	0.72287	0.02167
0.6839	0.07773	0.00031	0.00238	0.77471	0.02284
0.63757	0.08353	0.00108	-0.00385	0.82331	0.02277
0.59004	0.08847	0.00769	-0.00866	0.86782	0.02137
0.54177	0.09243	0.01979	-0.01291	0.90737	0.01863
0.49323	0.09532	0.03703	-0.0163	0.94105	0.01456
0.4449	0.09704	0.05924	-0.01869	0.96763	0.00945
0.39722	0.09754	0.08628	-0.01999	0.98608	0.00449
0.35064	0.09678	0.11795	-0.0202	0.99661	0.00113

## A.4 Wind tunnel calibration

Wind tunnel calibration was conducted on empty tunnel. Wind tunnel was run for different rpm and corresponding airflow velocity is measured using pitot-static tube as well as inclined manometer. The pressure is measured using electronic pressure sensor.



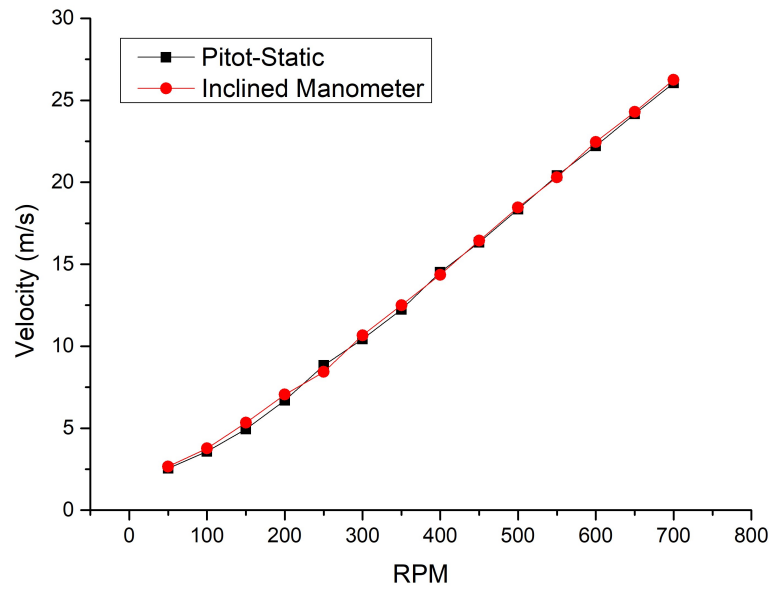


Figure A.3: Wind tunnel calibration chart

The result is shown in Figure A.3. Using the chart, wind tunnel rpm was set to get required flow velocity for further experiment.

## A.5 Iso surface plot of zero velocity

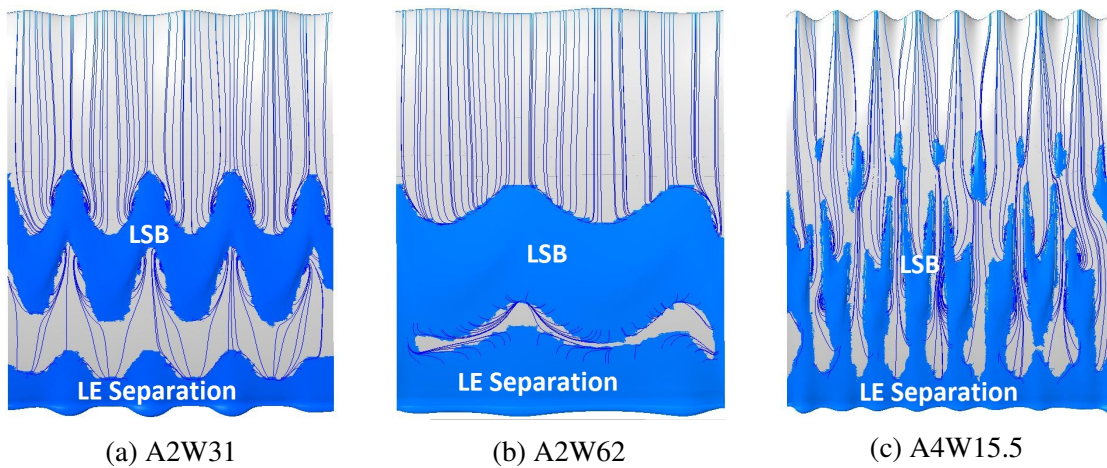
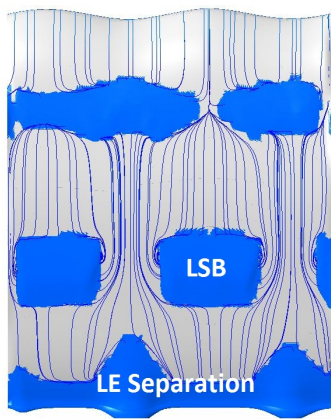
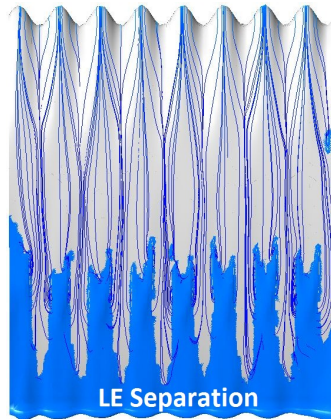


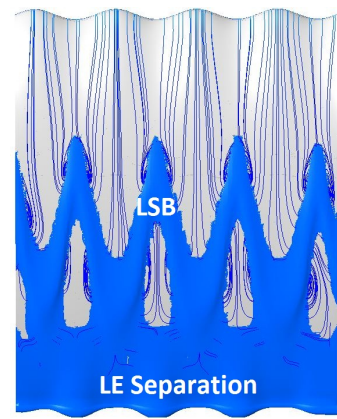
Figure A.4: Iso surface of zero velocity showing flow separation regimes



(d) A4W62



(e) A8W15.5



(f) A8W31

Figure A.4: Iso surface of zero velocity showing flow separation regimes



## APPENDIX B

# MATLAB CODE FOR SSWT BLADE DESIGN AND PERFORMANCE ASSESSMENT USING BEM THEORY

```
clc;
clear all;
close all;
%%%%%%%%%%%%%%%%%%%%%%%%%%%%%%%%%%%%%%%%%%%%%%%%%%%%%%%%%%%%%%%%%%%%%%%% input parameters (E216) %%%%%%%%%%
U =6.5 ;                % wind velocity
rpm = 360;              % rotor rpm
R = 1;                  % Radius of blade
alpha = 6 ;            % angle of attack
B = 3;                  % No. of blades
r_t = 1;                % Tip radius
r_h = 0.15;            % hub radius
Cl = 1.3523;
Cd = 0.01915;
lamda = 5.8;           % tip speed ratio
N = 10 ;               % No. of blade elements
nu = 16.46*10(-6);      % kinematic viscosity
%%
omega =2*pi * rpm./60 ; % angular velocity

for i = 1:N
r(i) = R./N.*i;
```

```

lamda_r(i) = r(i)./ R .* lamda;
Res1 =10; % residue..
Res2 =10; % residue..
a(i)=0; % axial induction factors
a1(i)=0; % angular induction factors
iter=0;

while ((Res1 >=0.00001 || Res2 >=0.00001) && iter <10000)

x1(i)=a(i);
x2(i)=a1(i);

U_rel(i) = (((1-a(i))*U).^2 + ((1+a1(i))
              *omega*r(i)).^2)^0.5
% relative wind velocity
phi_rad(i) = atan((1-a(i))*U./((1+a1(i))*omega*r(i)));
% relative wind flow angle in rad
phi(i) = phi_rad(i).*180./pi;
% relative wind flow angle in deg
beta(i) = phi(i) - alpha;
% Twist angle

c(i) = 8*pi*r(i).*(1-cosd(phi(i)))./(B*C1);
% chord length
S(i)=B*c(i)./(2*pi*r(i)) ;
% solidity

```

```

Re(i) = c(i) .* U_rel(i) ./ nu;
% Reynolds No.
f(i) = (B./2)*((R-r(i))./(r(i).*sind(phi(i))));
F(i) = (2./pi).*acos(exp(-f(i)));
% Tip loss factor
% C_T = (S*(1-a)^2*Cl*cosd(phi)+
          Cd*sind(phi))/((sind(phi))^2);

cn(i) = Cl.*cosd(phi(i))+Cd*sind(phi(i));
ct(i) = Cl*sind(phi(i))-Cd*cosd(phi(i));
k(i) = 4.*F(i).*(sind(phi(i)))^2./ (S(i).*cn(i));
ac = 0.25;
%%
if a(i)<0.25
a(i) = (k(i)+1).^(-1)
else
a(i) = 0.5*(2+k(i).*(1-2*ac)-sqrt((k(i).*(
          (1-2*ac)+2).^2+4.*(k(i)*ac.^2-1)));
end
%%
a1(i) = ((4*F(i)*sind(phi(i))*
cosd(phi(i))./(S(i).*ct(i)))-1).^(-1);

Res1 = abs(a(i)-x1(i));
Res2 = abs(a1(i)-x2(i));
iter = iter+1;

```

```

end
CP(i) = (F(i)*(sind(phi(i))).^2 * (cosd(phi(i))
- lamda_r(i).* sind(phi(i))) .* (sind(phi(i))
+ lamda_r(i)* cosd(phi(i))) .* (1-(Cd./Cl) *
cotd (phi(i))) * (lamda_r(i)).^2)

end
Cp = (8./(lamda * N)).* sum(CP) %coefficient of power.
xlswrite('Result.xlsx',[r' c' a' phi' beta' Re'
CP' ],4,'R4')

```

## APPENDIX C

### UNCERTAINTY IN EXPERIMENTAL MEASUREMENTS

#### C.1 Uncertainty associated with coefficient of pressure

( $C_p$ )

Uncertainty associated with the  $C_p$  measurement is calculated using the Equation C.1

$$\delta_{C_p} = \left[ \left( \frac{h_i - h_0}{h_\infty - h_0} \right)^2 (h_\infty \cdot \delta_{h_\infty})^2 + \left( \frac{1}{h_\infty - h_0} \right)^2 (h_i \cdot \delta_{h_i})^2 + \left( \frac{h_\infty - h_i}{h_\infty - h_0} \right)^2 (h_0 \cdot \delta_{h_0})^2 \right]^{\frac{1}{2}} \quad (\text{C.1})$$

where  $\delta_h$  is uncertainty associated with pressure measurement, which is equal to  $\pm 0.003$ .

#### C.2 Uncertainty associated with coefficient of normal force ( $C_n$ )

Uncertainty in coefficient of normal force is calculated using Equation C.2.

$$\begin{aligned} \delta_{C_n}^2 = & \left( \frac{dssin\theta}{c} \cdot C_p \delta_{C_p} \right)_{lower}^2 + \left( \frac{C_p sin\theta}{c} \cdot ds \delta_{ds} \right)_{lower}^2 + \left( \frac{C_p dscos\theta}{c} \cdot \theta \delta_\theta \right)_{lower}^2 + \\ & \left( \frac{C_p dssin\theta}{c^2} \cdot c \delta_c \right)_{lower}^2 - \left( \frac{dssin\theta}{c} \cdot C_p \delta_{C_p} \right)_{upper}^2 - \left( \frac{C_p sin\theta}{c} \cdot ds \delta_{ds} \right)_{upper}^2 - \\ & \left( \frac{C_p dscos\theta}{c} \cdot \theta \delta_\theta \right)_{upper}^2 - \left( \frac{C_p dssin\theta}{c^2} \cdot c \delta_c \right)_{upper}^2 \end{aligned} \quad (\text{C.2})$$



### C.3 Uncertainty associated with coefficient of normal force ( $C_n$ )

Uncertainty in coefficient of normal force is calculated using Equation C.3.

$$\begin{aligned} \delta_{C_t}^2 = & \left( \frac{dscos\theta}{c} \cdot C_p \delta_{C_p} \right)_{lower}^2 + \left( \frac{C_p cos\theta}{c} \cdot ds\delta_{ds} \right)_{lower}^2 + \left( \frac{C_p dssin\theta}{c} \cdot \theta\delta_\theta \right)_{lower}^2 + \\ & \left( \frac{C_p dscos\theta}{c^2} \cdot c\delta_c \right)_{lower}^2 - \left( \frac{dscos\theta}{c} \cdot C_p \delta_{C_p} \right)_{upper}^2 - \left( \frac{C_p cos\theta}{c} \cdot ds\delta_{ds} \right)_{upper}^2 - \\ & \left( \frac{C_p dssin\theta}{c} \cdot \theta\delta_\theta \right)_{upper}^2 - \left( \frac{C_p dscos\theta}{c^2} \cdot c\delta_c \right)_{upper}^2 \end{aligned} \quad (C.3)$$

where  $\theta$  is the angle in radian.

### C.4 Uncertainty associated with coefficient of lift ( $C_l$ )

Equation C.4 is used to calculate the uncertainty in coefficient of lift.

$$\delta_{C_l} = \left[ (\cos\theta)^2 \cdot (C_n \cdot \delta_{C_n})^2 + (C_n \cdot \sin\theta + C_t \cdot \cos\theta)^2 \cdot (\theta \cdot \delta_\theta)^2 + (\sin\theta)^2 \cdot (C_t \cdot \delta_{C_t})^2 \right]^{1/2} \quad (C.4)$$

### C.5 Uncertainty associated with coefficient of drag ( $C_d$ )

Following equations are used to find uncertainty in  $C_d$  measurement.

#### C.5.1 Uncertainty associated with $u/U_\infty$ ( $\delta_{u/U_\infty}$ ) :

$$\delta_{u/U_\infty} = \frac{1}{(U_\infty)^2} (u \cdot \delta_u)^2 + \left( \frac{u}{(U_\infty)^2} \right)^2 \cdot (U_\infty \cdot \delta_{U_\infty})^2 \quad (C.5)$$

Let,  $H = u/U_\infty$ ; and  $I = H(1-H)$ . Uncertainty in I,

$$\delta_I = [(1 - 2H)^2 \cdot (H \cdot \delta_H)^2] \quad (C.6)$$

Let  $\Theta = \frac{\Delta x}{2} [(I_1 + I_N) 2 \sum (I_{i+1} + I_{N-1})]$  and,  $C_d = \frac{2\Theta}{c}$

Then, Uncertainty in  $C_d$ ,

$$\delta_{C_d} = \sqrt{\left(\frac{2}{c}\right)^2 (\Theta \cdot \delta_\Theta)^2} \quad (C.7)$$

Table C.1: Uncertainty in  $C_p$  at AOA of  $4^\circ$

Coefficient of Pressure	Uncertainty in Coefficient of Pressure measurement
0.6	0.13
0.4	0.20
0.2	0.27
0.2	0.27
0.2	0.27
0.2	0.27
0.2	0.27
0.2	0.27
0.2	0.27
0.2	0.27
0.2	0.27
0	0.34
-0.2	0.40
-0.4	0.47
-0.4	0.47
-0.4	0.47
-0.6	0.54

-0.6	0.54
-0.6	0.54
-0.6	0.54
-0.6	0.54
-0.8	0.60
-0.8	0.60
-0.8	0.60
-0.8	0.60
-0.8	0.60
-0.8	0.60
-0.8	0.60

**Max. value = 0.60**

Table C.2: Uncertainty in  $C_l$ ,  $C_d$  and  $C_l/C_d$

Lift coefficient	Uncertainty in lift measurement (%)	Drag coefficient	Uncertainty in drag coefficient (%)	Lift to drag ratio	Uncertainty in lift to drag ratio (%)
0.54	0.91	0.0178	0.38	10.07139	1.72
0.55	0.91	0.01832	1.01	12.65265	2.31
0.60	0.99	0.03103	0.76	28.47835	2.41
0.61	0.99	0.10259	0.69	2.30603	3.74
0.62	1.22	0.12746	0.41	42.46742	5.69
0.74	1.37	0.01926	1.02	16.91	1.04
0.76	1.51	0.01974	0.72	18.51342	1.17
0.79	1.52	0.02093	0.81	19.86947	1.75
0.79	1.53	0.02093	0.47	22.73843	2.65
0.80	1.72	0.03103	0.92	30.05225	1.07

0.82	1.39	0.02069	0.58	28.86936	3.71
0.85	1.37	0.19253	0.63	42.5536	5.08
0.93	2.1	0.09827	0.98	29.15297	3.48
0.94	2.1	0.021	0.5	28.30867	5.07
0.96	2.19	0.02162	0.57	29.19915	2.19
0.96	2.17	0.0226	0.53	29.20241	4.77
0.99	3.42	0.03496	0.91	31.84148	2.78
1.01	2.7	0.02314	0.76	33.8436	4.78
1.08	1.37	0.0219	0.84	43.68528	5.24
1.09	3.01	0.0614	0.97	1.78658	3.7
1.11	2.19	0.02472	0.38	30.22276	4.21
1.12	1.21	0.02621	0.4	30.34739	4.04
1.16	3.74	0.02876	0.41	30.35421	4.57
1.17	1.18	0.02936	1.01	30.07201	4.96
1.19	1.78	0.03709	0.98	24.05269	2.78
1.20	2.16	0.03151	1.09	31.30133	4.1
1.24	3.07	0.0244	0.77	43.68565	4.98
1.25	2.06	0.03444	1.02	34.04026	4.08
1.26	1.97	0.03216	0.69	19.20795	2.47
1.28	2.7	0.03468	0.72	35.90542	0.78
1.37	1.64	0.03949	0.66	12.11288	1.97
<b>Max.</b>	<b>= 3.74</b>	0.04977	0.57	22.82379	4.37
<b>value</b>		0.06932	0.43	12.47354	1.97
		0.03422	0.72	43.68881	5.21
		0.02922	0.83	44.385	5.13
		0.032	0.32	37.62	3.7
		0.04467	1.42	37.62932	4.74
		0.11263	0.63	38.5165	4.39

0.04476	1.77	44.3956	4.72
0.0562	0.91	39.50927	4.26
0.0382	1.07	41.69719	4.91
0.06895	0.98	41.70656	4.79
0.081	0.97	5.63497	1.58
0.09843	0.47	<b>Max.</b>	<b>= 1.77</b>
0.01779	1.04	<b>value =</b>	
<b>Max.</b>	<b>= 1.77</b>		
<b>value</b>			

## REFERENCES

- Abate, G., D. N. Mavris, and L. N. Sankar (2019). Performance effects of leading edge tubercles on the nrel phase vi wind turbine blade. *Journal of Energy Resources Technology*, 141(5), 051206.
- Adu-Gyamfi, S. (2013). “*Computer-Aided Design Optimisation of Wind Turbine Airfoil for Low Wind Speed Applications*”. Ph.D. thesis.
- Barlow, J. B., W. H. Rae Jr, and A. Pope (2015). “Low Speed Wind Tunnel Testing”. *INCAS Bulletin*, 7(1), 133.
- Bergman, T. L., F. P. Incropera, D. P. DeWitt, and A. S. Lavine, *Fundamentals of heat and mass transfer*. John Wiley & Sons, 2007.
- Bolzon, M. D., R. M. Kelso, and M. Arjomandi (2015). “Tubercles and their applications”. *Journal of Aerospace Engineering*, 29(1), 04015013.
- Boudet, J., J.-F. Monier, and F. Gao (2015). “Implementation of a roughness element to trip transition in large-eddy simulation”. *Journal of Thermal Science*, 24(1), 30–36.
- Braslow, A. L., R. M. Hicks, and R. V. Harris (1966). “Use of grit-type boundary-layer-transition trips on wind-tunnel models”.
- Bushnell, D. M. and K. Moore (1991). “Drag reduction in nature”. *Annual Review of Fluid Mechanics*, 23(1), 65–79.
- Cabanillas Sanchez, V. (2013). “Blade performance analysis and design improvement of a small wind turbine for rural areas”.
- Cai, C., Z. Zuo, S. Liu, and T. Maeda (2018). “Effect of a single leading-edge protuberance on NACA 634-021 airfoil performance”. *Journal of Fluids Engineering*, 140(2), 021108.
- Cencelli, N. A., T. Von Bakstrom, and T. Denton (2006). “*Aerodynamic optimisation of a small-scale wind turbine blade for low windspeed conditions*”. Ph.D. thesis, Stellenbosch: Stellenbosch University.
- Custodio, D. (2007). “The Effect of Humpback Whale-like Leading Edge Protuberances on Hydrofoil Performance”. sl: Worcester polytechnic institute, 2007. *Google Scholar*.
- Dearing, S., S. Lambert, and J. Morrison (2007). “Flow control with active dimples”. *The Aeronautical Journal*, 111(1125), 705–714.

- Dewar, S. W., P. Watts, and F. E. Fish (2013). “Turbine and compressor employing tubercle leading edge rotor design”. US Patent 8,535,008.
- Drela, M., Xfoil: An analysis and design system for low Reynolds number airfoils. *In Low Reynolds number aerodynamics*. Springer, 1989, 1–12.
- Drela, M. and H. Youngren (2001). Xfoil 6.94 user guide.
- Eleni, D. C., T. I. Athanasios, and M. P. Dionissios (2012). “Evaluation of the turbulence models for the simulation of the flow over a National Advisory Committee for Aeronautics (NACA) 0012 airfoil”. *Journal of Mechanical Engineering Research*, 4(3), 100–111.
- Energypress (2019). <https://energypress.eu>. Accessed: 2019-22-04.
- Fagbenro, K., M. Mohamed, and D. Wood (2014). “Computational modeling of the aerodynamics of windmill blades at high solidity”. *Energy for Sustainable Development*, 22, 13–20.
- Favier, J., A. Pinelli, and U. Piomelli (2012). “Control of the separated flow around an airfoil using a wavy leading edge inspired by humpback whale flippers”. *Comptes Rendus Mecanique*, 340(1-2), 107–114.
- Fernandes, I., Y. Sapkota, T. Mammen, A. Rasheed, C. Rebello, and Y. H. Kim, “Theoretical and Experimental Investigation of Leading Edge Tubercles on the Wing Performance”. *In 2013 Aviation Technology, Integration, and Operations Conference*. 2013.
- Fish, F. E. and J. M. Battle (1995). “Hydrodynamic design of the humpback whale flipper”. *Journal of Morphology*, 225(1), 51–60.
- FLUENT (2014). 15.0. *Theory Guide*.
- Godard, G. and M. Stanislas (2006). “Control of a decelerating boundary layer. Part 1: Optimization of passive vortex generators”. *Aerospace Science and Technology*, 10(3), 181–191.
- Gopalarathnam, A., B. A. Broughton, B. D. McGranahan, and M. S. Selig (2003). “Design of low Reynolds number airfoils with trips”. *Journal of aircraft*, 40(4), 768–775.
- Hansen, K., R. Kelso, and B. Dally, “The effect of leading edge tubercle geometry on the performance of different airfoils”. *In Proc. 7th World Conference on Experimental Heat Transfer, Fluid Mechanics and Thermodynamics, Krakow, Poland*. 2009.
- Hansen, K. L. (2012). *Effect of leading edge tubercles on airfoil performance*. Ph.D. thesis.
- Hansen, K. L., R. M. Kelso, and B. B. Dally (2011). “Performance variations of leading-edge tubercles for distinct airfoil profiles”. *AIAA journal*, 49(1), 185–194.

- Horton, H. P. (1968). “*Laminar separation bubbles in two and three dimensional incompressible flow*”. Ph.D. thesis.
- Hu, H. and Z. Yang (2008). “An experimental study of the laminar flow separation on a low-Reynolds-number airfoil”. *Journal of Fluids Engineering*, 130(5), 051101.
- Jahanmiri, M. (2011). “Laminar separation bubble: its structure, dynamics and control”. Technical report, Chalmers University of Technology.
- Johari, H., C. W. Henoeh, D. Custodio, and A. Levshin (2007). “Effects of leading-edge protuberances on airfoil performance”. *AIAA journal*, 45(11), 2634–2642.
- Jones, A., N. Bakhtian, and H. Babinsky (2008). “Low Reynolds number aerodynamics of leading-edge flaps”. *Journal of Aircraft*, 45(1), 342–345.
- Kale, S. A. and R. N. Varma (2014). “Aerodynamic design of a horizontal axis micro wind turbine blade using naca 4412 profile”. *International Journal of Renewable Energy Research (IJRER)*, 4(1), 69–72.
- Karthikeyan, N., S. Sudhakar, and P. Suriyanarayanan, “Experimental studies on the effect of leading edge tubercles on laminar separation bubble”. 52nd Aerospace Sciences Meeting, AIAA SciTech Forum, 2014.
- Kim, H., J. Kim, and H. Choi (2018). “Flow structure modifications by leading-edge tubercles on a 3D wing”. *Bioinspiration & biomimetics*, 13(6), 066011.
- Kishore, R. A. (2013). *Small-scale Wind Energy Portable Turbine (SWEPT)*. Ph.D. thesis, Citeseer.
- Kline, S. J. and F. McClintock (1953). “Describing uncertainties in single-sample experiments”. *Mechanical engineering*, 75(1), 3–8.
- Lyon, C. A., M. S. Selig, and A. P. Broeren (1997). “Boundary layer trips on airfoils at low Reynolds numbers”. *AIAA Paper*, 511, 35.
- Malipeddi, A. K., N. Mahmoudnejad, and K. A. Hoffmann (2012). “Numerical analysis of effects of leading-edge protuberances on aircraft wing performance”. *Journal of Aircraft*, 49(5), 1336–1344.
- Manwell, J. F., J. G. McGowan, and A. L. Rogers, “*Wind energy explained: theory, design and application*”. John Wiley & Sons, 2010.
- McCrossen, T., A. Zakrzewski, and T. Pollock (2010). “Boundary layer trips on a clark y12 airfoil at low Reynolds numbers”.
- Melville Jones, B. (1934). “Stalling”. *The Journal of the Royal Aeronautical Society*, 38(285), 753–770.



- Melville Jones, B. (1937). The measurement of profile drag by the pitot-traverse method, the cambridge university aeronautics laboratory (r and m no. 1688). Technical report, Technical Report of the Aeronautical Research Committee for the Year 1935–1936.
- Menter, F., R. Langtry, and S. Völker (2006). “Transition modelling for general purpose CFD codes”. *Flow, turbulence and combustion*, 77(1-4), 277–303.
- Miklosovic, D., M. Murray, L. Howle, and F. Fish (2004). “Leading-edge tubercles delay stall on humpback whale (*Megaptera novaeangliae*) flippers”. *Physics of fluids*, 16(5), L39–L42.
- Multhopp, H., *Methods for calculating the lift distribution of wings (subsonic lifting-surface theory)*. Aeronautical Research Council London, 1950.
- Musial, W. and D. Cromack (1988). “Influence of Reynolds number on performance modeling of horizontal axis wind rotors”. *Journal of solar energy engineering*, 110(2), 139–144.
- Nosenchuck, D., G. Brown, H. Culver, T. Eng, and I. Huang, “Spatial and temporal characteristics of boundary layers controlled with the lorentz force”. In *12th Australian Fluid Mechanics Conference*. 1995.
- Pedro, H. T. and M. H. Kobayashi, “Numerical study of stall delay on humpback whale flippers”. In *46th AIAA aerospace sciences meeting and exhibit* volume 584. 2008.
- Polat, O. and I. H. Tuncer (2013). “Aerodynamic shape optimization of wind turbine blades using a parallel genetic algorithm”. *Procedia Engineering*, 61, 28–31.
- Preston, J. (1958). “The minimum Reynolds number for a turbulent boundary layer and the selection of a transition device”. *Journal of Fluid Mechanics*, 3(4), 373–384.
- Rahimi, H., W. Medjroubi, B. Stoevesandt, and J. Peinke, “2d numerical investigation of the laminar and turbulent flow over different airfoils using openfoam”. In *Journal of Physics: Conference Series* volume 555. IOP Publishing, 2014.
- Ramesh, G., K. Madhavan, and A. Sajeer (2009). “Development of smart actuators for active flow control at low reynolds number”.
- Rostamzadeh, N., K. Hansen, R. Kelso, and B. Dally (2014). “The formation mechanism and impact of streamwise vortices on NACA 0021 airfoil’s performance with undulating leading edge modification”. *Physics of Fluids*, 26(10), 107101.
- Rothan, D. (1993). “Low Reynolds number laminar separation bubble control using a backward facing step”.
- Russell, J., “Length and bursting of separation bubbles: a physical interpretation”. In *Science and Technology of Low Speed Motorless Flight, NASA Conference Publication* volume 2085. 1979.

- Schlichting, H. and K. Gersten, *Boundary-layer theory*. Springer, 2016.
- Selig, M. (2003). “Low Reynolds number airfoil design lecture notes”. *VKI lecture series*, 24–28.
- Selig, M. S. and B. D. McGranahan (2004). “Wind tunnel aerodynamic tests of six airfoils for use on small wind turbines”. *Journal of solar energy engineering*, 126(4), 986–1001.
- Serson, D. and J. Meneghini (2015). “Numerical study of wings with wavy leading and trailing edges”. *Procedia IUTAM*, 14, 563–569.
- Shah, H., S. Mathew, and C. M. Lim (2015). “Numerical simulation of flow over an airfoil for small wind turbines using the  $\gamma$ - $Re_\theta$  model”. *International Journal of Energy and Environmental Engineering*, 6(4), 419–429.
- Simens, M. and A. Gungor (2018). “Influence of the transition of a laminar separation bubble on the downstream evolution of strong adverse pressure gradient turbulent boundary layers”. *European Journal of Mechanics-B/Fluids*, 67, 70–78.
- Singh, R. K. and M. R. Ahmed (2013). “Blade design and performance testing of a small wind turbine rotor for low wind speed applications”. *Renewable Energy*, 50, 812–819.
- Skillen, A., A. Revell, J. Favier, A. Pinelli, and U. Piomelli, “Investigation of wing stall delay effect due to an undulating leading edge: An LES study”. In *TSFP DIGITAL LIBRARY ONLINE*. Begel House Inc., 2013.
- Slangen, R. (2009). “Experimental investigation of artificial boundary layer transition”. *Master of Science Thesis, TU Delft*, vol, 82.
- Stein, B. and M. Murray (2005). “Stall mechanism analysis of humpback whale flipper models”. *Proceedings of Unmanned Untethered Submersible Technology (UUST)*, UUST05, 5.
- Sudhakar, S., N. Karthikeyan, and L. Venkatakrishnan (2017). “Influence of leading edge tubercles on aerodynamic characteristics of a high aspect-ratio UAV”. *Aerospace Science and Technology*, 69, 281–289.
- Swatton, P. J., *Principles of flight for pilots* volume 42. John Wiley & Sons, 2011.
- Traub, L. W. (2011). “Experimental investigation of the effect of trip strips at low Reynolds number. *Journal of Aircraft*, 48(5), 1776–1784.
- Tummala, A., R. K. Velamati, D. K. Sinha, V. Indraja, and V. H. Krishna (2016). “A review on small scale wind turbines”. *Renewable and Sustainable Energy Reviews*, 56, 1351–1371.

UIUC (2014). <http://m-selig.ae.illinois.edu/ads/coord/e216.dat>. Accessed: 2014-11-05.

Van Nierop, E. A., S. Alben, and M. P. Brenner (2008). “How bumps on whale flippers delay stall: an aerodynamic model”. *Physical review letters*, 100(5), 054502.

Walker, G., “The role of laminar-turbulent transition in gas turbine engines: a discussion”. In *ASME 1992 International Gas Turbine and Aeroengine Congress and Exposition*. American Society of Mechanical Engineers, 1992.

Watts, P. and F. E. Fish, “The influence of passive, leading edge tubercles on wing performance”. In *Proc. Twelfth Intl. Symp. Unmanned Untethered Submers. Technol. Auton. Undersea Syst. Inst. Durham New Hampshire*, 2001.

## PUBLICATIONS BASED ON THIS THESIS

### Journal Papers

1. Sreejith B.K and Sathybhama A., Numerical study on effect of boundary layer trips on aerodynamic performance of E216 airfoil, *Engineering Science and Technology, an International Journal*, Vol 21, 77–88, 2018.
2. Sreejith B.K and Sathybhama A., Numerical investigation on effect of leading edge tubercle on laminar separation bubble, *CEAS Aeronautical Journal* (Communicated).
3. Sreejith B.K, Sathybhama A, Experimental and numerical study of laminar separation bubble formation on low Reynolds number airfoil with leading edge tubercles, *The Aeronautical Journal* (Communicated).

### Conference Papers

1. Sreejith B.K and Sathybhama A., Design of Small Scale Wind Turbine Blade for Low Wind Potential Areas *WEENTECH Proceedings in Energy - Volume 4*, NIT Patna, March 2016, 17 - 20, ISSN: 2059-2353.
2. Sreejith B.K., Sathybhama A., Pratik B Maniya and Ravi N Patel, Effect of different shapes of boundary layer trips on aerodynamic performance of e216 airfoil profile, *Proceedings of sixth asian symposium on computational heat transfer and fluid Flow*, IIT Madras, December 2017, 354 - 361.
3. Sreejith B.K and Sathybhama A., Numerical study and performance analysis of E216 airfoil for low Reynolds number application, *Proceedings of 24th National and 2nd International ISHMT-ASTFE Heat and Mass Transfer Conference*, BITS-Pilani, December 2017.
4. Sreejith B.K, Sathybhama A. and Sandeep Kumar S., Effect of boundary layer trip shape on laminar separation bubble, *25th National and 3rd International ISHMT-ASTFE Heat and Mass Transfer Conference*, IIT Roorkee, December 2019 (Abstract accepted).

# CURRICULUM VITAE

---

## **SREEJITH B K**

'Thayath', Baladuka

Nekraje PO

Kasaragod, Kerala, India - 671543 Email: srijithbk@gmail.com

Contact Details: 97 47 33 53 21

---

## **PROFESSIONAL SUMMARY**

Results-oriented mechanical engineer with a hands-on approach to tackling projects and accomplishing goals.

---

## **SKILLS**

- MATLAB programming, C, C++
  - AUTO CADD, ICEM CFD, SOLIDWORKS2010
  - ANSYS 15.0, XFOIL, QBLADE, PROPID
  - LATEX, ORIGIN Pro
  - Proficient in Numerical Simulations (FVM).
- 

## **WORKSHOP/PROGRAMS ATTENDED/ORGANISED**

- 16th National Training Course on Wind Energy Technology, 23-25 July 2014, National Institute of Wind Energy Technology, Chennai.
  - Awareness Program on Intellectual Property Rights for MSME's, 1st September 2016, NITK Surathkal.
  - 42nd National Conference on Fluid Mechanics and Fluid Power (FMFP), 14-16 December 2015, NITK Surathkal.
  - Organising committee member - 12th National Conference on Technological Trends, College of Engineering Trivandrum, August 2012.
  - Organising committee member - 42nd National Conference on Fluid Mechanics and Fluid Power (FMFP), 14-16 December 2015, NITK Surathkal.
-

## Academic Records

- Doctoral Program: Aerodynamics, National Institute of Technology Karnataka, Karnataka, 2018
- M.Tech: Thermal Science, College of Engineering Trivandrum, Kerala, 2012
- B.E: Mechanical Engineering, Sree Narayana College of Engineering and Technology, Kannur, 2008
- Higher Secondary: Swamiji's HSS Edneer, Kasaragod, 2004
- High School, NHS Perdala, Kasaragod, 2002